12-9-2009

A Physical Model of Human Skin and Its Application for Search and Rescue

Abel S. Nunez

Recommended Citation

Nunez, Abel S., "A Physical Model of Human Skin and Its Application for Search and Rescue" (2009). *Theses and Dissertations*. 1972.
https://scholar.afit.edu/etd/1972

A Physical Model of Human Skin
and Its Application for Search and Rescue

DISSERTATION

Abel S. Nunez, Major, USAF

AFIT/DEO/ENG/09-14

DEPARTMENT OF THE AIR FORCE
AIR UNIVERSITY

AIR FORCE INSTITUTE OF TECHNOLOGY

Wright-Patterson Air Force Base, Ohio

AFIT/DEO/ENG/09-14

A Physical Model of Human Skin
and Its Application for Search and Rescue

DISSERTATION

Presented to the Faculty

Graduate School of Engineering and Management

Air Force Institute of Technology

Air University

Air Education and Training Command

In Partial Fulfillment of the Requirements for the

Degree of Doctor of Philosophy
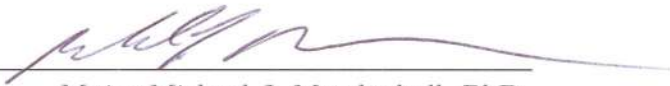
Abel S. Nunez, B.S.E., M.S.E.E.

Major, USAF

December 2009

AFIT/DEO/ENG/09-14

A Physical Model of Human Skin and Its Application for Search and Rescue
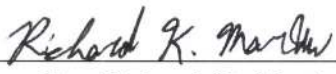
Abel S. Nunez, B.S.E., M.S.E.E.

Major, USAF

Approved:

(signature)	2-DEC-09
Major Michael J. Mendenhall, PhD (Chairman)	date
(signature)	02 Dec 2009
Dr. Richard K. Martin (Member)	date
(signature)	2-Dec-2009
Dr. Kevin C. Gross (Member)	date
(signature)	2 Dec 2009
Lt Col Heidi C. Bertram, MD (Member)	date
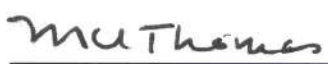
Accepted:

(signature) M. U. Thomas	14 Dec 2009 Date

Dean, Graduate School of Engineering and Management

Abstract

Hyperspectral data is rich in features that allow accurate identification of a wide variety of materials, including human skin. The question this research answers is "Can we develop a skin reflectance model in the visible (VIS) and near infrared (NIR) portions of the electromagnetic spectrum and use it to develop skin detection and classification algorithms?" To answer this question, this research is divided into three parts. First, we describe an engineering model of human skin reflectance in the VIS and NIR. Second, we model sensor output based on knowledge of the skin reflectance spectra, incident radiance spectra, and sensor response. Finally, we describe and demonstrate algorithms for accurate skin detection and skin color estimation from hyperspectral images.

The skin reflectance model developed in this research is based on data collected by the scientific community, measurements collected from cadavers and living subjects, and measurements of some of the constituent components of skin. The model treats skin as a multi-layered material where each layer has a specific absorption and scattering coefficient based on the materials that make up the layer. The reflectance and transmittance values of each optical interface and each layer can then be calculated with the Fresnel and Kubelka-Munk equations. All these values are then used to determine an overall reflectance of skin. Various parameters in the model such as melanosome level, blood level, and oxygenation level can be adjusted to show their effect on the skin reflectance spectra. The results of the skin reflectance model along with illumination by various blackbody radiators are then used as inputs into a modeled sensor. The selected modeled sensor used in this analysis is a generic Red-Green-Blue (RGB) sensor. The modeled skin reflectance spectra is also used to develop the Normalized Difference Skin Index (NDSI) and the Normalized Difference Green Red Index (NDGRI). These indices are computationally inexpensive and allow

for the development of skin detection algorithms with a high probability of detection (P_D) and a low probability of false alarm (P_{FA}). The Near Infrared Melanosome Index (NIMI) is also developed from the skin reflectance model. This index allows for the development of an algorithm to estimate the reflectance of skin at any point in the VIS based on reflectance data at two wavelengths (the first between 650nm and 900nm and second at 1080nm).

To test the accuracy of the skin reflectance model, a comparison is made between measured and modeled data. The average root mean square error across the VIS and NIR between measured and modeled data for skin from living subjects and skin from cadavers was 1.12% and 2.43% respectively. The skin reflectance model then allows us to generate qualitatively accurate responses for an RGB sensor for different biological and lighting conditions. To test the accuracy of the skin detection and skin color estimation algorithms, hyperspectral images of a suburban test scene containing people with various skin colors were collected. The skin detection algorithm developed in this work had a P_D as high as 0.95 with a P_{FA} of 0.006. Skin reflectances of the subjects in the image were collected with an ASD FieldSpec3® Spectrometer for comparison with results from the NIMI algorithm applied to the hyperspectral image. The mean absolute error between data measured by the ASD FieldSpec3® Spectrometer and data estimated by the NIMI algorithm is 0.026 where the reflectances of the individuals at 685nm ranged from 0.14 to 0.64.

Acknowledgements

Abel S. Nunez

Table of Contents

List of Figures

Figure | Page

A Physical Model of Human Skin

and Its Application for Search and Rescue

I. Introduction

1.1 Introduction

Hyperspectral sensors provide a great deal of spectral granularity and a potential means for improved detection and classification of select materials [49]. They have demonstrated an excellent capability for identifying anomalous materials of interest from airborne platforms over a large geographic area to include geologic and biologic surface cover. Their use is certainly not limited to applications of physical sciences and can be extended to a plethora of remote object detections such as aircraft wreckage or a lost hiker's exposed skin [85]. In terms of the latter example, current airborne systems exist that perform search and rescue (SAR) by way of spectral matching [76,89]. The effectiveness of the SAR application is often in the hands of an operator that requires a large degree of "operator capability." It is noted by experts that any hyperspectral system developed for use in SAR will need to be simple enough to operate for a non hyperspectral-exploitation expert [81] and allow the user to discriminate small targets in a large scene [46]. Due to the nature of SAR, near real-time exploitation of the data is essential for it to be of use [77]. A hyperspectral/multi-spectral system designed to automatically detect and classify the pigmentation level of human skin can be one of the components of such a critical system.

One example of an airborne hyperspectral imaging system used in SAR is the Civil Air Patrol's Airborne Real-Time Cueing Hyperspectral Enhanced Reconnaissance (ARCHER) system [81]. ARCHER is able to search for objects with a specific spectral signature and send any data of interest to ground stations for further analysis [14]. The current ARCHER system collects data in the spectral range of 500nm-1100nm, where human skin has a large difference in spectral response based on its

1

color. Extending the capability of the system to collect farther into the near-infrared (NIR) could improve its ability to detect skin since its spectral response in this region does not vary significantly based on its color.

Face recognition is an active area of research that could benefit from knowledge of the spectrum of human skin. Many face recognition algorithms depend on the size, shape, and color of facial features to identify a face [97]. However, performance of these algorithms is degraded by something as simple as a change in face orientation [63]. Hyperspectral images provide several additional features to aid in face recognition. For example, the spectral signature of skin on the face provides a pose-invariant feature for use in these algorithms [62].

Knowledge of skin spectra of the hand has applications in hand and gesture recognition. Hand and gesture recognition is important for designing new and improved human/computer interfaces [15, 54] and is currently based on the color and geometry of the hand [11, 74]. A hyperspectral image of the hand could provide additional information, such as whether a pixel is from the palm or the back of the hand, based on the melanosome level of the skin. Hyperspectral imagery could also identify specific points on the hand such as melanin spots or veins to assist in determining the hand's position.

1.2   *Anatomy and color of human skin*

Skin is constructed of multiple layers with varying thicknesses and varying optical properties. A typical cross-section of skin is shown in Fig. 1 where the primary layers are the epidermis, dermis, and subcutaneous tissue. The epidermis is constructed of the stratum corneum, stratum lucidum, stratum granulosum, and stratum basale. The dermis is constructed of the papillary dermis and reticular dermis. Within the dermis are various blood vessels, nerve endings, and sweat glands, which all affect the optical properties of the dermis. Below the dermis is a layer of subcutaneous tissue which includes fat and striated muscle. Each layer of skin is constructed of various

combinations of water, collagen, blood, melanosomes, and other chromophores such as bilirubin and betacarotene.
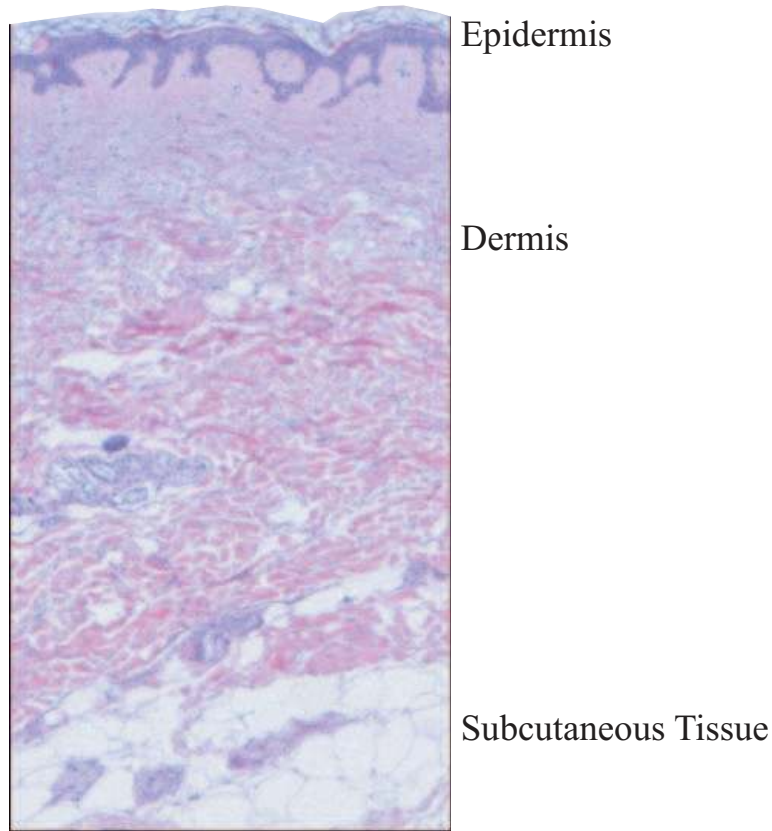
Figure 1:   Cross-section of thin skin collected from a fair-skinned cadaver.

The thickness of the tissue layers can differ depending on their location on the body. For example, the dermis of the back is approximately twice as thick as that of the abdomen. The stratum corneum of the sole of the feet and the palm of the hand are several times thicker than on any other part of the body. These variations affect the reflectance of skin, especially in the NIR.

The color of human skin varies from people with an almost white complexion to those with a black-brown color [57]. Skin color is determined by a number of optical factors such as the refraction coefficient of the surface of the skin, the absorption coefficients of the skin layers and each layer's scattering coefficient. Differing amounts of melanosomes in the epidermis account for the largest difference in skin color. A cor-

Table 1:   Percentage of the epidermis volume occupied by melanosomes [35].

Skin Color	Melanosome Percentage (%)
Light-Skinned Adult	1.6 - 6.3
Moderately Pigmented Adult	11 - 16
Darkly Pigmented Adult	18 - 43

Table 2:   The Fitzpatrick scale used to describe skin color and its sensitivity to ultra-violet radiation [51].

Type	Color	Sun Response
I	Very Fair	Always Burns
II	Fair	Usually Burns
III	White to Olive	Sometimes Burns
IV	Brown	Rarely Burns
V	Dark Brown	Very Rarely Burns
VI	Black	Never Burns

respondence between skin color and the percentage of the epidermis volume occupied by melanosomes is shown in Table 1.

For clinical purposes, skin can be divided into one of six types according to the Fitzpatrick Scale (Table 2). This scale is used to describe skin color and its sensitivity to ultra violet radiation [93]. A connection can be made between the melanosome level in the epidermis and the Fitzpatrick skin type based on the description of skin color in Table 1 and Table 2. (This connection is used in describing skin based on our estimates of the melanin in Section 4.7.)

Differing amounts of hemoglobin, bilirubin, and betacarotene in skin can also account for a large difference in skin color. An increase in dermal blood level causes skin to take on a ruddy color while a decrease causes skin to take on a paler color [67]. Increased amounts of bilirubin or betacarotene in skin cause it to take on a yellow or yellow/orange tint, respectively [45].

1.3   General approaches to modeling multi-layered materials

Existing models of human skin can be categorized as: 1) Monte-Carlo models, 2) diffusion theory models, and 3) Kubelka-Munk theory models [8]. Each model has its advantages and disadvantages in terms of modeling skin reflectance. Monte-Carlo models have the potential to calculate a highly accurate reflectance. However, the accuracy of these methods for estimating reflectance is limited by the accuracy of the model's representation of the structure of the material. In addition, these models are computationally intensive.

Diffusion theory models are a class of model that exhibit reduced complexity compared to Monte-Carlo models, yet appear to have similar capability. Diffusion theory takes into consideration the absorption and scattering properties of the different layers of a material and uses boundary conditions and differential equations to determine the amount of reflected light.

The model with the lowest level of complexity discussed in this dissertation uses Kubelka-Munk theory. Kubelka-Munk theory is a simplified version of diffusion theory that assumes there is no reflection at the boundaries of the different tissue layers and assumes layers are semi-infinite slabs. Models based on the Kubelka-Munk theory are less accurate than those based on diffusion theory or Monte-Carlo theory. However, Kubelka-Munk models are not as computationally intensive.

1.3.1   Monte-Carlo reflectance models.   Monte-Carlo methods are based on following the path of photons randomly scattered and absorbed in different layers of material. A photon traveling with a specific wavelength is modeled as having entered the material. After the photon travels a short distance, it has a probability of being absorbed, scattered, or continuing to travel in its current direction. The probability of being absorbed or scattered is based on the wavelength of the photon and the distance the photon travels.

The distance increment of the photon path for each iteration of the model is a small fraction of the thickness of the material layer through which it is traveling. If

the photon is absorbed, the simulation of the photon's path is ended. If the photon is scattered, the direction of the path of the photon is changed. The new path of the photon can be in any direction. The probability a specific direction is selected is based on the scattering profile of the material layer.

If the photon is neither absorbed nor scattered, it will continue in its current direction. The photon continues to travel until it is either absorbed in the material, transmitted through the material in a specific direction, or reflected back out of the material in a specific direction.

This process is continued with multiple photons to determine what percentage of photons are reflected back out of the skin. This method is computationally intensive since a large number of photons traveling at different wavelengths needs to be modeled to obtain accurate results. Furthermore, if one is estimating diffuse reflectance, the additional cost of calculating the direction of the reflected or transmitted photons is unnecessary and computationally expensive.

1.3.2 Diffusion theory reflectance models. The propagation of light through a turbid (semi-opaque) media, such as skin, can be described using diffusion theory [8]. Diffusion theory is based on a differential equation derived from the full Boltzmann transport equation [31]. It assumes one of two things happen to light traveling through a layer: light can be isotropically scattered or it can continue traveling in its current direction. This theory is practical for modeling light traveling through a highly scattering media [31]. For the modeling of skin reflectance in the visible (VIS) region of the spectrum, the condition of scattering events being more likely than absorption events is easily met. However, in the NIR, water and lipid absorption begins to dominate over scattering events making diffusion theory a poor choice for this portion of the spectrum [8].

1.3.3 Kubelka-Munk theory reflectance models. The Kubelka-Munk theory assumes light incident on a layer is either absorbed within the layer, isotropically

scattered within the layer, or transmitted through the layer. Based on the absorption coefficient, scattering coefficient, and thickness of a particular layer, the amount of light reflected or transmitted through the layer can be determined. The reflectance and transmittance of each layer are incorporated into a multi-layer model that gives an estimate of the material's reflectance. An example of a skin reflectance model based on Kubelka-Munk theory is the model proposed by Dawson *et al.* [16].

Using the depth, reflectance, and transmittance of the layer of material, Kubelka-Munk theory was further used to calculate the absorption and reduced scattering coefficient of skin [5]. Furthermore, the simplicity of Kubelka-Munk skin models allows for quick computation of estimated skin reflectance [8].

1.4 *Remote sensing of skin*

A group of subjects is presented in Fig. 2 with a variety of pigmentation levels that cover the range of Type II to Type VI skin. Ambient lighting conditions can significantly change the apparent color of skin [3], which makes determining skin pigmentation levels a challenging problem. This phenomenon is demonstrated in Fig. 2 where shadowing on the necks makes the corresponding skin appear darker, which demonstrates the difficulty of designing an algorithm that will detect skin and classify its pigmentation level over a full range of illumination levels.

1.4.1 Skin detection in color imagery.   Detection of human skin in color imagery can be difficult because many materials have a color similar to one of the many shades of skin. Skin detection methods with color imagery vary from a ratio of color-space channels to more sophisticated machine learning mechanisms such as the self-organizing map (SOM) [92]. Regardless of the methodology used, the end result is often a high probability of detection (P_D), typically above 90%, with an unfortunate high probability of false alarm (P_{FA}) [9], often on the order of 15%.

Color-space channel skin detection methods typically use two color channels. For example, the full range of skin colors has a red to green ratio greater than one,

Figure 2: Color image of a group of subjects with different skin pigmentations under solar illumination in a suburban environment.

red to blue ratio greater than one, and a green to blue ratio greater than one [9]. These methods produce a significant number of false alarms, and some authors have attempted to mediate this issue with a rules-based approach combining ratios, color-space channel thresholds, and color-space channel differences [65, 92] to maintain the high P_D rates while reducing P_{FA} rates. These approaches essentially define a volume (Voronoi tessellation) of the three-dimensional color-space which encompasses possible skin colors. Other methods reduce false alarms by examining how skin pixels cluster spatially and then attempt to determine if the spatial clustering resembles a part of the body such as a limb [25] or a face [30].

The red-green-blue (RGB) color space is most common in the literature, but may not be ideal for the skin detection task. The disadvantages of the RGB color space is the strong correlation between the channels [92]. Other color-spaces such as hue-saturation-value, hue-saturation-lightness, tint-saturation-luminance, luma-chroma red difference, and chroma blue difference, separate luminance (intensity) and chrominance (hue) which results in a better clustering of skin-colored pixels in the selected color-space [27]. Although, the selection of a color-space may allow for a simpler or more intuitive algorithm, it has been shown by others that there is no

optimum three channel color-space for skin detection if the optimal skin detector for that color-space is used [3].

Other skin detection methods use three-channel color-space examples as a training set to train a classification system to classify an unknown quantity as skin or not skin. In some cases, pixels are projected onto a plane within the color-space that provides the furthest separation between skin pixels and non-skin pixels [9]. This technique in particular provides a slight improvement over the ratio-based methods.

Some statistical-based approaches analyze training images for the probability of skin occurring given a pixel in the image, the probability of a skin color occurring given a pixel is skin, and the probability of a skin color occurring in an image overall. From these quantities, the probability a pixel is skin given a specific skin color is calculated from the training images [9]. This general approach is susceptible to the "data problem" – there is not enough training and testing images under various operating conditions to compute these quantities accurately. These methods may be particularly susceptible to the data sets available, and hence, the results of the system are often questionable. Several other methods have been attempted for skin detection in images with limited success: self organizing maps, Gaussian mixture models, and various clustering algorithms. They all appear to have similar performance to the statistical approach described previously, but tend to be less computationally intensive.

1.4.2 Detection of skin in near-infrared imagery. The same optical parameters that affect the color of human skin also affect skin's reflectance in the NIR region of the electromagnetic spectrum. Analysis of skin's optical parameters results in elegant and computationally efficient detection and pigmentation estimation algorithms. Skin has a high reflectance between 800-1100nm and a low reflectance beyond 1400nm. This observation has been noted by others and exploited, although they have not yet publicly documented their degrees of success. For example, skin detection using two NIR channels has been accomplished for the purpose of counting occupants

in a vehicle [64] and for face detection [19]. Both of these methods use bands that are several hundred nanometers wide in the NIR, which, depending on the operating environment, likely result in a higher P_{FA} than if these regions were narrower. The most notable work, and that referenced by [64], is presented in [40].

The work in [40] exploits the absorption and reflective properties of skin, and and operates in the range of 800-1400nm for the lower wavelengths and 1400-2500nm for the upper wavelengths. Although not explicitly shown, the authors describe a scaled distance between the upper and lower wavelengths and threshold that scaled distance to declare the presence or absence of human skin. Our work uses a similar detection scheme we call the normalized difference skin index (NDSI) [58] (motivated by the normalized difference vegetation index [22]) that carefully chooses narrow spectral bands of interest due both to the spectral properties of skin as well as the known solar illumination source. We further incorporate additional spectral information to help reduce false alarm sources in the natural and urban environments yielding robust detectors.

Our current work extends that described in [40] in the following ways. First, it explains the physiology of human skin and how it relates to hyperspectral human skin modeling that leads to our skin detection algorithm. In doing so, our work refines the broad ranges described in [40] to more refined spectral components based specifically on solar illumination and the optical properties of skin tissue. Second, it extends the skin detection capability to arbitrary environments in the remote setting by incorporating additional spectral information into the detector thus reducing false alarms. Third, our work further estimates the melanin content of detected skin. Finally, our work has a correspondence based on our optical model of human skin in [59], which provides a sound theoretical mapping from image acquisition to skin detection and melanin estimation not described in other literature.

1.5   Research question

The previous sections lead to the following critical question: "Can we develop an engineering model of skin reflectance in the VIS and NIR and use it to develop algorithms to assist in the detection and classification of human skin?" An engineering model of skin reflectance can show how the constituent components of skin interact with light to create a range of characteristic features that can be exploited for remote sensing and classification applications. These features can then be used to detect people in hyperspectral images and identify different properties such as melanosome level. In all cases, we show that the answer is yes.

1.6   Organization of dissertation

The remainder of this dissertation is organized as follows. Chapter 2 provides an in-depth description of a skin reflectance model based on the Kubelka-Munk equations. This includes a description of the optical coefficients used by the model and how adjusting the various parameters affect model results. A comparison is made between modeled and measured results for living people and cadavers. Chapter 3 discusses how hyperspectral reflectance data, along with radiance data and a sensor response, can be combined to determine sensor output. To demonstrate the effect on a generic color (RGB) sensor, the combination of skin reflectance and illumination source is applied to an avatar to produce a color image. Chapter 4 presents the skin detection and melanosome level estimation algorithms for use with remotely sensed hyperspectral data. Results of applying these algorithms to a suburban scene containing people with a variety of pigmentation levels and various skin color confusers is presented. Chapter 5 discusses current and future efforts based on the development of this research. This includes the development of a camera system for real-time skin detection and melanosome level classification. We conclude by offering recommended improvements to the model and skin detection algorithm as well as the addition of detection/classification algorithms.

II. Physics-Based Human Skin Reflectance Model

2.1 Introduction

In this chapter, we propose a novel engineering model of human skin reflectance in the visible (VIS) and near-infrared (NIR) portions of the electromagnetic spectrum. This model is a hybrid of that presented by Matcher and Meglinski [52], but uses optical equations to simplify and speed up model output. The model uses optical parameters from the literature [12, 26, 35, 60, 69] and incorporates real measurements from samples extracted from cadavers as well as spectral measurements from living subjects. Our contributions to the field are two-fold. First is a newly computed reduced scattering coefficient for the dermis and epidermis based on reflectance measurements from cadavers and living people. Second is a high fidelity skin reflectance model which compares favorably with measured skin reflectance data, a stark improvement over existing models [16, 52].

In order to better understand how skin's chromophores effect the overall reflectance, we seek an accurate model that allows us to tune the parameters. In the following discussion of modeling, we will specifically discuss reflectance models, skin models, and skin reflectance models. A skin model refers to a description of skin as multiple layers. Each of these layers has specific optical properties depending on its thickness and tissue makeup. A reflectance model describes a method of modeling the reflectance of a multi-layer material based on the knowledge of each layer's thickness and the optical properties of the constituent components. A skin reflectance model is a combination of a specific reflectance model with a specific skin model. The skin reflectance model created for this work treats skin as having a Lambertian and specular component. The specular component of skin can have a large variation due to the position of the light source, skin and sensor relative to each other. However, for this work, we model the light source and sensor as being normal to skin. This allows us to use the Fresnel equations described in Section 2.2.2 to estimate the amount of specular reflection.

The remainder of this chapter is arranged as follows. The anatomy of human skin is presented and several previously developed models of skin reflectance are described, including the multi-layer skin reflectance approach [16, 45, 52]. The optical properties of the components of skin used by several existing skin reflectance models are described [35, 43, 71]. The results from the multi-layer skin reflectance model developed in this work and the effect of adjusting various optical parameters on the model are then explored. Next, we compare the skin reflectance model developed in this work with results from existing models [35, 72] and measured reflectance data from living subjects and cadavers. Finally, we list conclusions and describe the future work necessary to improve the skin reflectance model.

2.2   Kubelka-Munk theory reflectance model

The Kubelka-Munk equations describe transmission (t_n) and reflection (r_n) of light at a specific wavelength in a homogenous layer of material with constant thickness. This layer both absorbs and scatters light where the transmission and reflection of the nth layer is described in Eqn. (1) and Eqn. (2) as:

$$t_n(\lambda) = \frac{4\beta_n(\lambda)}{(1 + \beta_n(\lambda))^2 e^{K_n(\lambda)d_n} - (1 - \beta_n(\lambda))^2 e^{-K_n(\lambda)d_n}}, \tag{1}$$

$$r_n(\lambda) = \frac{(1 - \beta_n(\lambda)^2)(e^{K_n(\lambda)d_n} - e^{-K_n(\lambda)d_n})}{(1 + \beta_n(\lambda))^2 e^{K_n(\lambda)d_n} - (1 - \beta_n(\lambda))^2 e^{-K_n(\lambda)d_n}}, \tag{2}$$

where

$$\beta_n(\lambda) = \sqrt{A_n(\lambda)/(A_n(\lambda) + 2S'_n(\lambda))}, \tag{3}$$

$$K_n(\lambda) = 2\sqrt{A_n(\lambda)(A_n(\lambda) + 2S'_n(\lambda))}, \tag{4}$$

d_n is the thickness of the material [16], and λ indicates the dependency on wavelength. The coefficients $A_n(\lambda)$ and $S'_n(\lambda)$ in Eqn. (3) and Eqn. (4) are related to the absorption and scattering coefficients ($a_n(\lambda)$ and $s'(\lambda)$ respectively) by Eqns. (5) and (6) [13] as:

$$A_n(\lambda) = \frac{a_n(\lambda)}{\frac{1}{2} + \frac{1}{4}\left(1 - \frac{s'_n(\lambda)}{(s'_n(\lambda) + a_n(\lambda))}\right)}, \tag{5}$$

$$S_n(\lambda) = \frac{s_n(\lambda)}{\frac{4}{3} + \frac{38}{45}\left(1 - \frac{s'_n(\lambda)}{(s'_n(\lambda) + a_n(\lambda))}\right)}. \tag{6}$$

2.2.1 Kubelka-Munk multi-layer reflectance model.   Human skin consists of multiple layers of tissues with unique optical properties. The reflectance of skin depends on many factors, including the light source and skin's structure [30,43,63,79, 83]. The multi-layer skin reflectance model is a physics-based model which describes the reflectance spectra of skin. An anatomy of normal human skin describes four layers: stratum corneum, epidermis, dermis, and subcutaneous tissue. As described earlier (see Section. 1.2), the epidermis and dermis can each be further divided into different layers.

In the model proposed by Meglinski and Matcher, the epidermis is described as the stratum corneum and living epidermis [52]. The dermis is described as the papillary dermis, upper blood net dermis, dermis, and deep blood net dermis [52]. We note that the Meglinski and Matcher model attempts to capture the anatomy of skin in a descriptive engineering model.

2.2.2 A generic N-layer model structure. By identifying the thickness of each tissue layer and its optical properties, a skin reflectance model can be created. One simplifying assumption made for the model is that the light incident on the skin is normal to the skin's surface (as stated earlier, skin is not completely Lambertian as can be seen in existing bidirectional reflectance distribution function measurements [50]). The Fresnel equation describes the amount of reflection for light at normal incidence at the interface between two materials with indices of refraction η_1 and η_2 [28] and is computed as:

$$F = \left(\frac{\eta_2 - \eta_1}{\eta_2 + \eta_1} \right)^2,$$
(7)

where η_1 is the index of refraction of air while η_2 is the index of refraction of the stratum corneum. Although light at angles other than normal incidence will have increased amounts of Fresnel reflection [28], this is outside the scope of this work. Using the Kubelka-Munk equations (Eqns. (1), (2), (3), and (4)), the optical properties and thickness of each tissue layer, one can calculate the reflected and transmitted light energy.

In order to apply the Kubelka-Munk and Fresnel equations, some simplifying assumptions need to be made. First, we assume skin is a Lambertian (constant bidirectional reflection distribution function) surface with a specular component [42]. For this work, the specular component is due to Fresnel reflection from light perpendicularly incident on the skin [5, 43]. Second, we assume skin is constructed of a finite number of layers. The model describes skin as layers with similar optical properties and assumes there is an instantaneous transformation of their optical properties from one layer to the next. Third, we assume each tissue layer has a constant thickness. Finally, we assume that each layer is homogenous in terms of its absorption and scattering coefficients. Although the layers of skin are not of constant thickness and are

not necessarily homogenous, these assumptions are necessary for making the model tractable.

Consider the generic model in Fig. 3, where the surface of a multi-layered material is illuminated with unit energy and the arrows indicate the paths of light within each layer. For a given layer, light is either absorbed, scattered out the top of the layer, scattered out of the bottom of the layer, or continues on its path (without scattering) through the bottom of the layer. The fraction of light reflected off the material is the sum of the fractions of light for each path exiting the material, including the Fresnel reflectance. The fraction of light for each of the exiting paths can be estimated as the product of the Fresnel transmittance, the transmittance of all the layers it travels through to reach the path's final layer, the reflectance of the path's final layer, the transmittance of the layers it travels through to return to the surface of the material, and the Fresnel transmittance. For example, the fraction of light represented by V_3 in Fig. 3 is the product of the Fresnel transmittance, transmittance of layer 1, transmittance of layer 2, reflectance of layer 3, transmittance of layer 2, transmittance of layer 1, and the Fresnel transmittance. The total transmittance to layer 3 is the same as the total transmittance for the return path out the surface of the material. However, we describe all transmittances in the order they occur for completeness.

The limitation to this approach is that it does not consider all possible paths light may take when it travels through a pair of interfaces. For example, in existing approaches it is assumed that, for a pair of interfaces, the transmittance is the product of the transmittance of the two interfaces. It is also assumed the reflectance is the sum of the reflectance of the first layer and the product of the transmittance of the first interface and the reflectance of the second interface. The fact that light may reflect multiple times between the two interfaces before it exits one of the interfaces, is often ignored.
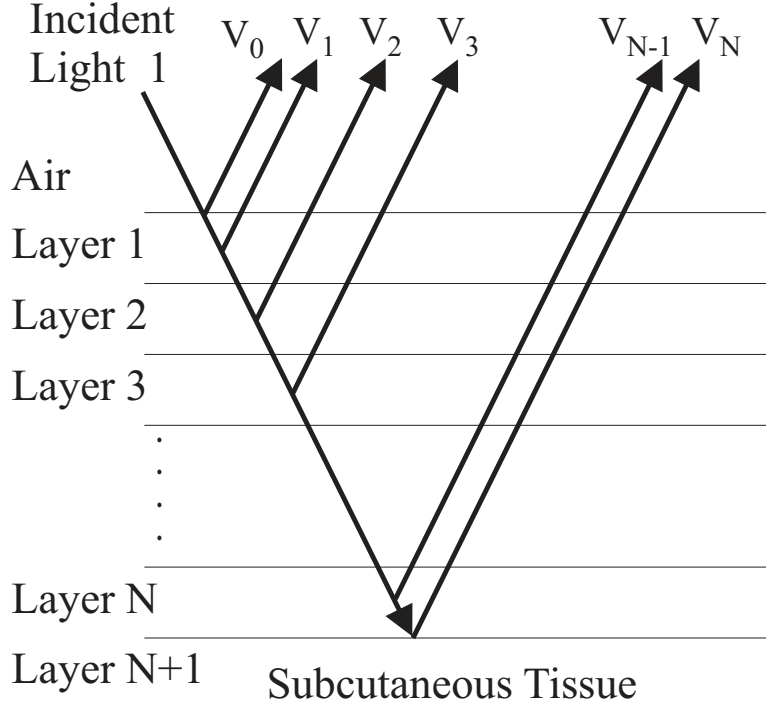
Figure 3:   Multi-layer skin reflectance model based on Fresnel reflection and transmission, Kubelka-Munk reflection and transmission, and reflection of subcutaneous tissue. The arrows depict light traveling through optical interfaces and not a specific direction for the light's path.

Figure 4 shows an example of the possible paths light may take between interfaces 0 and 1 and the resulting transmittance and reflectance for the combined interfaces. The total reflectance of the two interfaces is the sum of all reflectance paths as described by:

$$R_1 = r_0 + t_0^2 r_1 \sum_{m=0}^{\infty} (r_0 r_1)^m \qquad (8)$$

while the total transmittance is the sum of all transmittance paths as described by:

$$T_1 = t_0 t_1 \sum_{m=0}^{\infty} (r_0 r_1)^m. \qquad (9)$$

For these equations, r_n and t_n are the reflectance and transmittance of the nth optical interface. An optical interface is defined as a point in the skin model where Fresnel reflectance and transmittance occurs or where Kubelka-Munk reflectance and transmittance occurs.
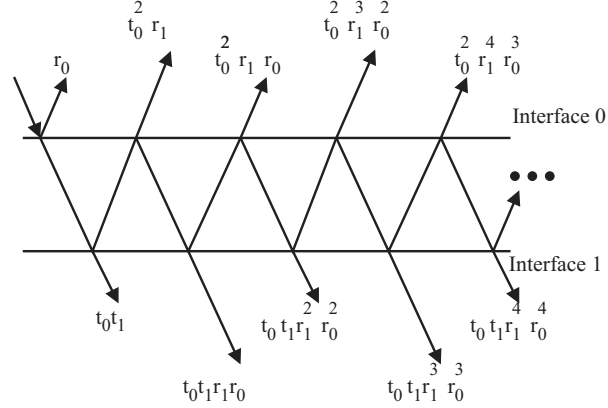
Figure 4: Fractions of reflectance and transmittance for possible paths of light for model interfaces 0 and 1.

The calculation of R_1 and T_1 allows us to begin the process of calculating R_{n+1} and T_{n+1} which are defined as the total reflectance and total transmittance (respectively) of optical interfaces 1 through $n + 1$. This is done iteratively, where the calculations of R_{n+1} and T_{n+1} are dependent on R_n and T_n as:

$$R_{n+1} = R_n + T_n^2 r_{n+1} \sum_{m=0}^{\infty} (R_n r_{n+1})^m \quad \text{and} \tag{10}$$

$$T_{n+1} = T_n t_{n+1} \sum_{m=0}^{\infty} (R_n r_{n+1})^m. \tag{11}$$

The infinite sums in Eqns. (10) and (11) are of the form $\sum_{i=0}^{\infty} a^i$ which converges to $1/(1-a)$ if $a < 1$. Since $(R_n, R_{n+1}) < 1$ and none of the interfaces analyzed in this work are 100% reflective, Eqns. (10) and (11) respectively converge to:

18

$$R_{n+1} = R_n + \frac{T_n^2 r_{n+1}}{1 - r_{n+1} R_n} \quad \text{and} \tag{12}$$

$$T_{n+1} = \frac{T_n^2 t_{n+1}}{1 - r_{n+1} R_n} \,. \tag{13}$$

2.2.3 Process for generating spectra. To calculate the total reflectance and transmittance in a multi-layer model, one needs to take an iterative approach with Eqn. (12) and Eqn. (13). First, calculate the Fresnel reflection of the top layer where R_0 is the Fresnel reflection and $T_0 = 1 - R_0$. Second, calculate the reflectance and transmittance of each of the layers using the Kubelka-Munk equations (Eqn. (1) and Eqn. (2) respectively). Third, determine R_1 and T_1 based on r_1, t_1, R_0, and T_0. The values of R_1 and T_1 are the total reflectance and transmittance of the interfaces 0 and 1 in the multi-layer model. The values of R_1, T_1, r_2, and t_2 are then used to calculate R_2 and T_2, which are the total reflectance and total transmittance of interfaces 0, 1, and 2. This procedure continues until one reaches the final layer N. At that point, one can calculate the total reflectance and transmittance of all the layers, R_N and T_N.

The final element of the skin reflectance model is the reflectance of subcutaneous tissue. Although one can model the absorption, scattering, and reflectance properties of subcutaneous fat and possibly the striated muscle beneath, it is beyond the scope of this dissertation and is recommended for future work. Instead, we use reflectance measurements of subcutaneous tissue as layer $N + 1$. This approach is reasonable since subcutaneous fat is often significantly thicker than skin and can be considered an infinite slab where light is only reflected at the interface and any light entering the tissue is entirely absorbed. To determine the reflectance of skin over subcutaneous

Table 3:   ASD FieldSpec3® Spectrometer Parameters [4].

Parameter	Value
Spectral Range	350 - 2500 nm
Spectral Resolution	3 nm at 700 nm
	10 nm at 1400 nm
	10 nm at 2100 nm
Sampling Interval	1.4 nm at 350 - 1050 nm
	2 nm at 1000 - 2500 nm

tissue, one needs to calculate R_{N+1} using Eqn. (12) and Eqn. (13) where r_{n+1} is the reflectance of the subcutaneous tissue.

2.3   Data and tissue collection

In order to accomplish the research goals discussed earlier, several data collections were necessary from both living subjects and cadavers. These included reflectance measurements from both and included the collection of skin samples from cadavers. Reflectance measurements were collected with the Analytical Spectral Devices (ASD) FieldSpec® 3 Spectrometer. The ASD FieldSpec3® Spectrometer consists of a hand-held contact probe connected to a spectrometer with a fiber optic cable. The probe contains its own illumination source which covers the VIS and NIR. The system is calibrated by placing the probe with its illumination source on against a calibrated reflectance panel with a known reflectance. The amount of light received by the spectrometer at a specific wavelength can then be associated with the reflectance of a material at that same wavelength. Once the system is calibrated, the contact probe is placed against materials such as skin and the material's reflectance for different wavelengths in the VIS and NIR can be collected. The spectral range and resolution of the system is shown in Table 3.

2.3.1   Collection from living subjects.   Our first set of data collections consisted of reflectance measurements from volunteers with various levels of pigmentation.

Because this part of the data collection deals with living human subjects, we obtained permission from the AFIT Institutional Review Board (IRB) to conduct our experiments (see Appendix A for a copy of the exemption letter from the AFIT IRB). The approved collection form is shown in Fig. 5.
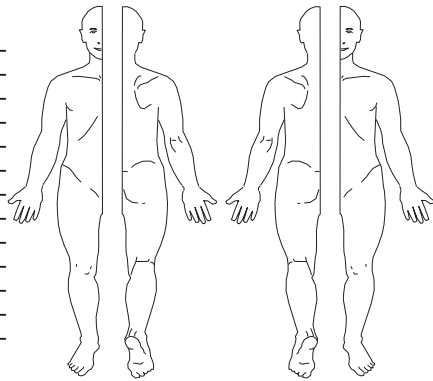
Figure 5:   Volunteer collection form.

Skin reflectance measurements of the volunteers were collected with an ASD FieldSpec3® Spectrometer, which shines a low-powered (less than 10W) white light from a contact probe onto the object of interest and measures the amount of light reflected off that object. Reflectance measurements were collected from the forearm of each subject. This area was selected since it does not have a significant amount of hair, which allows for near pure skin reflectance measurements.

2.3.2   Collection from cadavers.   A consistent procedure was used to collect data from each cadaver. Permission from the Director of the Anatomical Gift Program, Boonshoft School of Medicine, Wright State University was obtained to perform the described analysis (see Appendix A). Several sites on the cadaver were chosen for analysis. Each site was photographed with a standard digital camera, had a reflectance measurement collected with the ASD FieldSpec3® Spectrometer, and had tissue samples extracted from the site. The procedures used for each step is documented in the following paragraphs.

All procedures were documented on a form (Fig. 6) that listed all pertinent information about the data collection. The form allows for the selection of one to six sights on the cadaver for analysis.

Using the same ASD FieldSpec3® Spectrometer used on the living subjects, reflectance measurements were collected from multiple points on several cadavers. Following the reflectance measurements, skin tissue samples were collected from the same points on each of the cadavers using a 4mm disposable skin biopsy punch. The skin samples were then placed in individually marked cassettes and placed in containers of 10% neutral buffered formalin. Analysis of the skin samples was conducted by a staff pathologist, Department of Pathology, 88th Medical Group, Wright-Patterson AFB, Ohio. The analysis consisted of tissue preparation, determination of the thickness of the various layers of the skin, a clinical assessment of the melanin content, and a high-resolution color photograph of the tissue samples so they may be analyzed using image processing techniques at a later juncture.

2.4   Optical properties of skin components

One factor that simplifies the modeling of skin is that the dermal optical properties are essentially the same for different people. The same is true for the epidermis where the most notable exception is melanosome level [82]. The calculation of the reflectance and transmittance for the Kubelka-Munk equations for an arbitrary layer n are based on the absorption and scattering coefficients of the skin components (a_n

```
File Information for Cadaver
        Control Number:        _____
        Date:                  _____
        Collector:             _____
Subject Information
        Sex:      M    F       Age:      _____
        Race:      _____       Pigmentation Estimate:     Fair     Moderate     Dark
Data Collected
        Spectral Reflectance:            Y       N
        Visible Hyperspectral Image:     Y       N
        NIR Hyperspectral Image:         Y       N
        Camera Image:                    Y       N
        Skin Samples:                    Y       N
        If skin samples are collected, number of samples from:
        Location 1    _____      Location 2    _____      Location 3    _____
        Location 4    _____      Location 5    _____      Location 6    _____

  Notes:_____
  _____
  _____
  _____
  _____
  _____
  _____
  _____
  _____
  _____
  _____
  _____
  _____
                                        Data Collection Locations
                                     (Write circled number over location)
```

Figure 6:   Cadaver collection form.

and s'_n respectively). These are assumed constant across models, except for differing amounts and at different tissue depths. The main absorbers in skin in the VIS are melanosomes, collagen, and hemoglobin [2,25,80] while the main absorber in the NIR is water [72]. Melanosomes exist primarily in the epidermis while hemoglobin exists primarily in the dermis. Water exists in all layers to varying degrees.

2.4.1   Index of refraction.   Although the indices of refraction are wavelength dependent, an approximation is made that they are constant across the VIS and NIR. When considering the basic anatomical view of human skin, the only significant index of refraction exists between air/stratum corneum interface. These indices of refraction

are 1.0 and 1.5 respectively. The index of refraction between the stratum corneum, epidermis, and dermis are nearly identical (1.5, 1.34, 1.40 respectively) [53] and are safely ignored here and later when we present an engineering model of skin anatomy in Section 2.5.

2.4.2 Absorption coefficients.

2.4.2.1 Water. Water is skin's main constituent. Its absorption is insignificant in the VIS, but has several significant absorption features in the NIR. The absorption of water (shown in Fig. 7) in the VIS is defined in [61] and in the NIR is defined in [12].
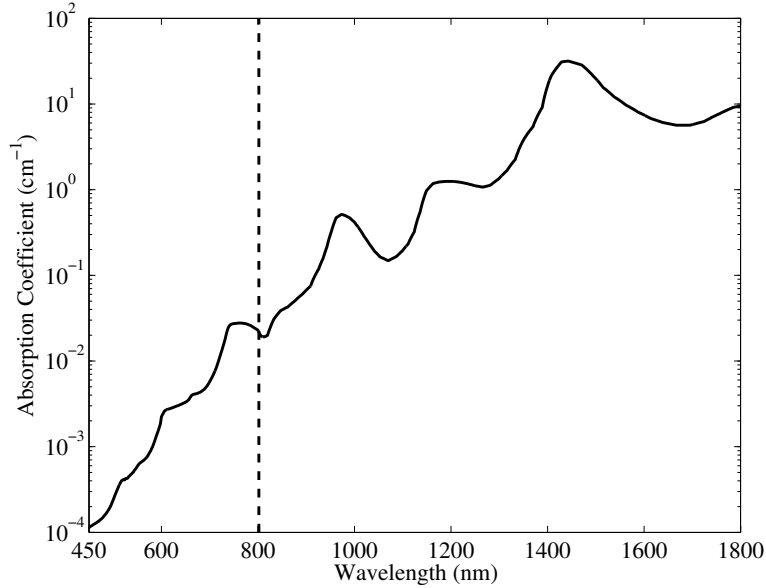
Figure 7: Water absorbtion in the visible (VIS) [61] and near-infrared (NIR) [12]. Dashed line delineates data from [61] and [12].

2.4.2.2 Collagen. While water makes up the majority of the dermis, the next most plentiful material in the dermis is collagen at 15-30% of skin's volume. Absorption measurements of collagen were derived in this dissertation by measuring the transmittance of sheets of clear gelatin, which consist of 100% collagenous protein. These measurements were conducted with the ASD FieldSpec3® Spectrometer

and ASD Leaf Clip. The ASD Leaf Clip connects to the hand-held probe on the spectrometer in such a way that a white-panel rest flush against the probe. A calibration measurement is collected to determine the amount of light from the probe that reflects off the panel and is received by the fiber optic cable in the probe. The thickness of a gelatin sheet is measured with a micrometer and then inserted between the probe and the leaf clip's white panel. A measurement of light returning to the probe with the gelatin between the probe and panel is collected. Part of the light transmits through the gelatin sheet, reflects off the white panel, transmits through the gelatin sheet again, and returns to the probe. The rest of the light is absorbed by the gelatin sheet. Since the path length through the gelatin is known (twice the thickness of the gelatin sheet since it travels through the sheet twice) and the fraction of light absorbed by the gelatin sheet is now known, the absorption coefficient of the gelatin can then be calculated using the Kubelka-Munk equations. The use of the Kubelka-Munk equations is based on the assumption that the scattering by the gelatin is insignificant when compared with its absorption. A similar assumption was made in [90] which calculated the absorption coefficient of gelatin in a similar manner. Absorption results for the gelatin sheet are shown in Fig. 8.

Assuming the dermis and epidermis are a combination of collagen and water, a comparison is made between measurements of dermis and epidermis absorption measured by others. Figure 9 shows the dermis and epidermis absorption coefficients developed in this dissertation, measured by Saidi *et al.* [71], and measured by Salomatina *et al.* [72]. The results measured by Saidi *et al.* were collected from bloodless dermis sample from neonatal skin [71]. The results measured by Salomatina *et al.* were measured from abdominal skin from fair-skinned adults (Caucasians) [72]. The results presented in this work are a summation of the absorption of 70% water and 30% collagen for the dermis and a summation of the absorption of 20% water and 80% collagen for the epidermis as documented by Meglinski and Matcher [52].

In the VIS, there is a wide variation in values for the absorption coefficient found in the literature and those measured for this research. These differences can
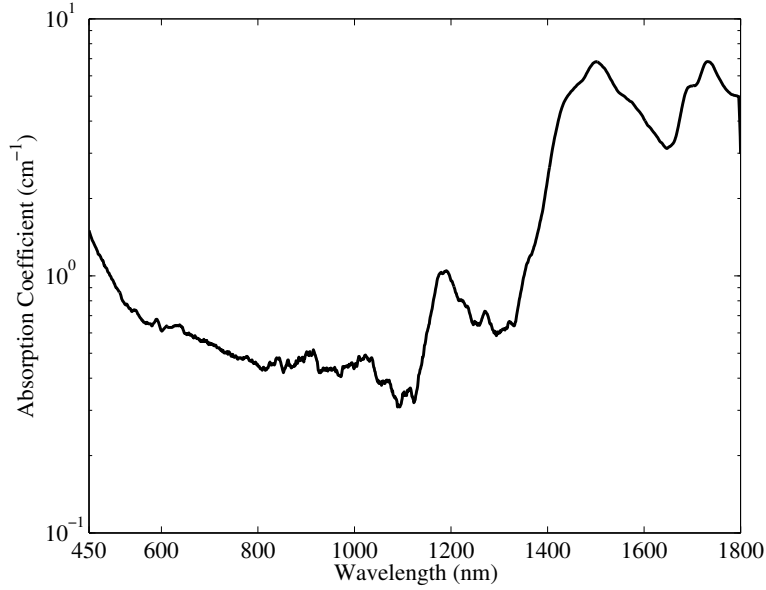
Figure 8: Collagen absorbtion in the VIS and NIR measured from gelatin sheets which are 100% collagenous protein.
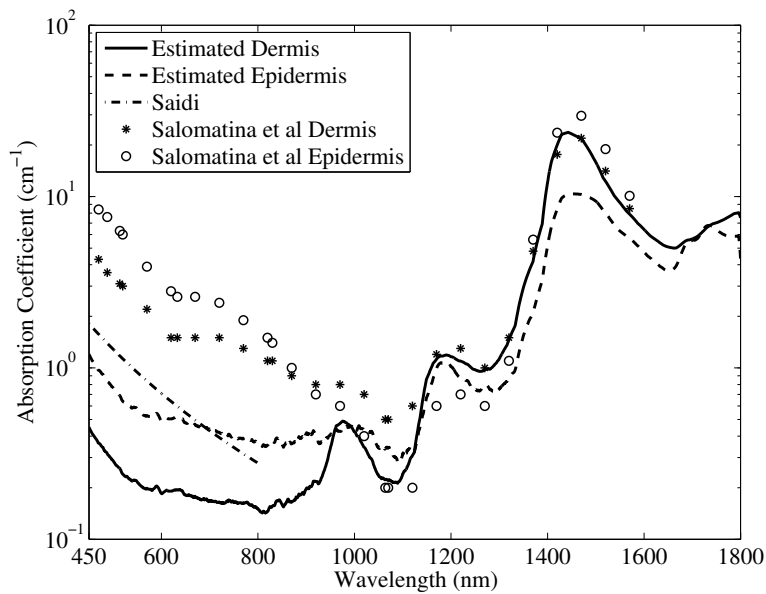
Figure 9: Comparison of dermis and epidermis absorbtion values defined in this research (solid and dashed) with that of the literature of Saidi *et al.* (dashed-dotted) [71] and Salomatina *et al.* (circles and asterisks) [72].

be accounted for by different materials, methods, and assumptions made by each of the researchers. In the NIR, water absorption begins to dominate and the absorption coefficients measured by each of the researchers and for this dissertation are similar.

2.4.2.3 Melanosomes. One of the main chromophores in skin is melanin [43] which is produced by melanocytes within the stratum basale (bottom layer of the epidermis). Melanin works its way toward the surface of the skin within biological cells called melanosomes [37]. Differing amounts of melanosomes in the epidermis account for the greatest difference in skin color between people world-wide [33, 34, 41] (Table 1). People from areas with intense sunlight have a tendency to have increased amounts of melanosomes [33] as a form of protection against the dangerous affects of UV radiation [34]. The absorption of melanosomes (a_{mel}) is characterized by:

$$a_{\text{mel}} = 6.6 \times 10^{11} \lambda^{-3.33} \tag{14}$$

where the units for λ are nanometers and the units for a_{mel} are cm^{-1} [35]. The general trend for melanosome absorption (Fig. 10) is for it to decrease as the wavelength increases over the VIS and NIR. Beyond 1100nm, melanosome absorption does not significantly affect skin reflectance as a majority of the absorption is due to water [5].

2.4.2.4 Hemoglobin. The second major chromophore in the VIS is hemoglobin suspended in the blood which exists in varying concentrations within the dermis and subcutaneous tissue. There are two types of hemoglobin: oxygenated hemoglobin and deoxygenated hemoglobin. Oxygenated hemoglobin is hemoglobin that has been oxygenated in the lungs and transports oxygen to the cells of the body. Deoxygenated hemoglobin is hemoglobin that has released the oxygen to the cells of the body, which is then returned back to the lungs. Blood is concentrated just above and below the dermis, with a limited amount existing within the dermis. The depth and concentration of blood play a key part in the reflectance spectra in the VIS. Another important component is the ratio of oxygenated hemoglobin to deoxygenated hemoglobin. When blood leaves the lungs, it is approximately 100% oxygenated, and
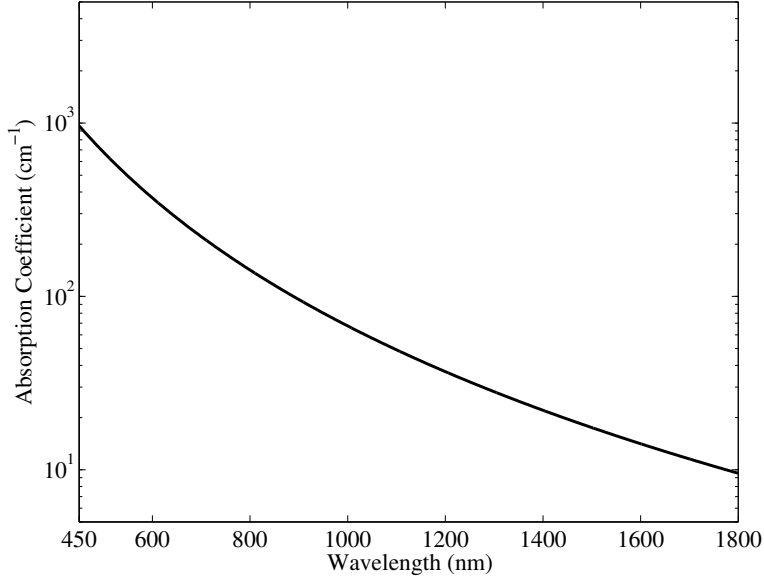
Figure 10: Melanosome absorbtion in the VIS and NIR based on values measured by Jacques [35].

when it returns to the lungs, it is approximately 50% oxygenated. We make the assumption that half of the blood volume is leaving the lungs while the other half is inbound to the lungs. As such, oxygenated hemoglobin throughout the body makes up 75% of the total hemoglobin while deoxygenated hemoglobin makes up the remaining 25%. It is important to note that concentrations can vary in different parts of the body based on a number of factors. This is discussed further in Section 2.7.

Figure 11 shows the absorption spectrum for both oxygenated hemoglobin (solid line, 100% oxygenation level) and deoxygenated hemoglobin (dashed line, 0% oxygenation level) in the VIS. The absorption coefficient assumes that hemoglobin has a typical concentration of $150g/L$ in blood [44]. The actual concentration of oxygenated hemoglobin and deoxygenated hemoglobin are each a fraction of this amount and sum to one. Conditions such as anemia will reduce the overall concentration where conditions such as polycythemia vera will increase the overall concentration [47]. In these extreme cases, the hemoglobin absorption will be reduced, or exaggerated, respectively.
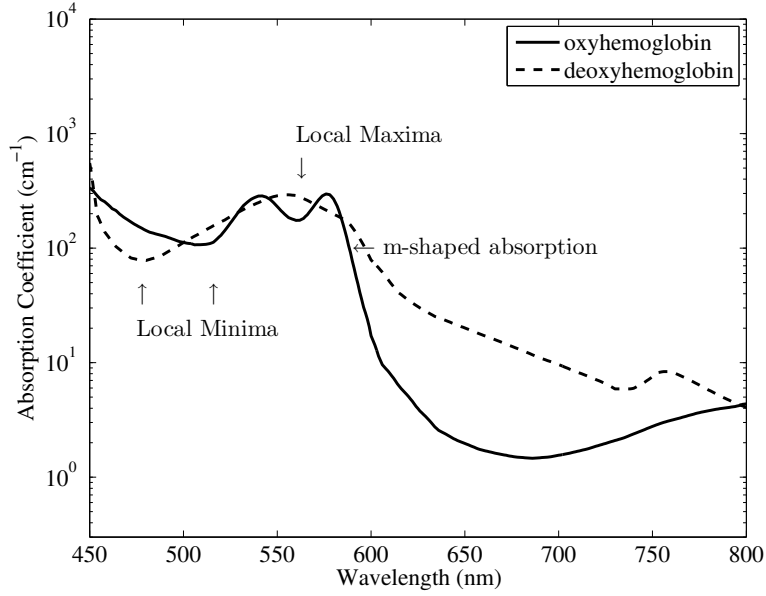
Figure 11: Oxygenated hemoglobin and deoxygenated hemoglobin absorption in the VIS (solid and dashed respectively) at concentration in blood of $150g/L$ [68].

Oxygenated hemoglobin has a few key absorption features: an m-shaped absorption at ≈ 560nm and a local minimum at ≈ 510nm. Note that for deoxygenated hemoglobin, the m-shaped absorption feature does not exist. There is, however, a local minimum at ≈ 480nm and a local maximum at ≈ 560nm. The shift in absorption features from oxygenated hemoglobin to deoxygenated hemoglobin change the reflected color of hemoglobin from deep red to red with a dark bluish tint [48, 70].

For both oxygenated hemoglobin and deoxygenated hemoglobin, the absorption drops sharply as wavelength increases. Once in the NIR, the effect of hemoglobin absorption is virtually non-existent.

2.4.2.5 Bilirubin and betacarotene. Bilirubin is a byproduct of hemoglobin and has a yellow color. It gives people with conditions such as jaundice a yellow tint [98]. Figure 12 (solid) shows the absorption of bilirubin at a typical concentration of $0.05g/L$ in blood [44].

Betacarotene is a chromophore that exists in both skin and blood. Betacarotene strongly absorbs in the green and blue parts of the spectrum giving objects it colors

29

a yellow/orange tint. Figure 12 shows the absorption of betacarotene for a normal concentration of $2.1 \times 10^{-4} g/L$ in the epidermis (dashed-dotted) and $7.0 \times 10^{-5} g/L$ in the blood (dashed) [44].
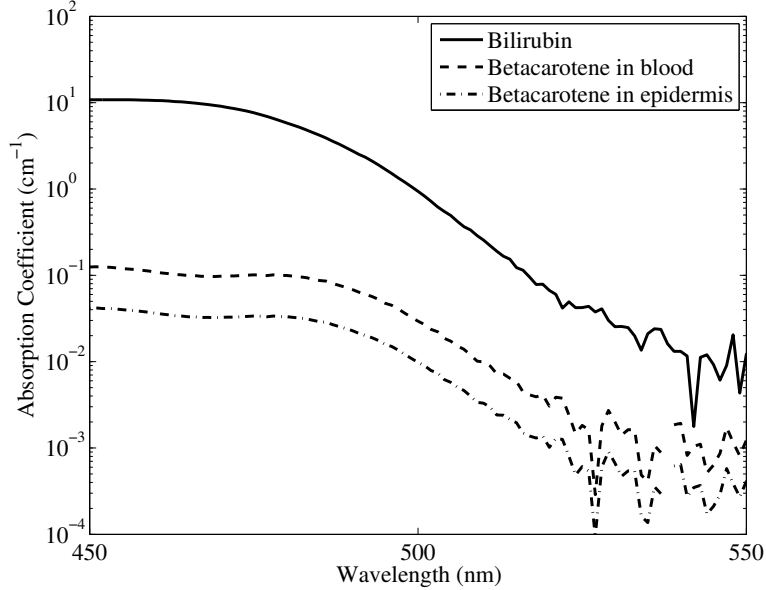
Figure 12: Absorbtion of bilirubin at concentration in blood of $0.05 g/L$ (solid), betacarotene in the epidermis at concentration of $2.1e^{-4} g/L$ (dashed), and betacarotene in blood at concentration of $7.0e^{-5} g/L$ (dashed-dotted) [44].

2.4.3 Reduced scattering coefficient. The scattering coefficient for skin has been calculated by multiple researchers with different methods and varying results [13]. Past works have shown that skin tissue is highly forward scattering [7,91] and is based on the size of the collagen fibers in the dermis and their index of refraction. Rayleigh scattering dominates in the smaller wavelengths while Mie scattering dominates in the larger wavelengths [71].

The calculation of the reduced scattering coefficient for this research is based on data collected from living skin and cadavers. Data from living skin consists of 24 reflectance measurements collected from the forearms of people with various levels of pigmentation. For the cadaver skin data, 76 reflectance measurements and corresponding skin samples were collected from multiple sites on 14 bodies. Extracted

samples were analyzed by a pathologist who provided tissue layer thicknesses and a labeling of skin color.

The next step in determining the reduced scattering coefficient is the creation of an engineering model for skin reflectance. This model is discussed in greater detail in Section 2.5. However, for now, this skin reflectance model is defined with the function $\Omega(\lambda, A, B, \mathbf{P}_m)$ where $\mathbf{P}_m$ is a vector of six values used to define the parameters for skin reflectance, the variables A and B define a universal reduced scattering coefficient, and λ indicates dependence on wavelength. A description of the vector $\mathbf{P}_m$ can be found in Table 5. Once a universal reduced scattering coefficient is determined, the skin reflectance model can be redefined as $\Omega(\lambda, \mathbf{P}_m)$ since parameters will no longer be necessary to define the reduced scattering component of the model. The universal reduced scattering coefficient is constrained by the power law form:

$$s'(\lambda) = A\lambda^{-B} \tag{15}$$

where the parameters A and B are positive numbers. This form smoothly and monotonically decreases and allows the modeling of a scattering coefficient that rapidly decreases in the VIS and becomes near constant in the NIR. This form has been used by multiple researchers to characterize reduced scattering in tissues with scatterers of different sizes [96]. Although the different layers of skin may have different scattering coefficients, they are modeled as being the same for this work. This greatly reduces the complexity of the engineering model for skin reflectance.

Using all the measurements, the vector $\mathbf{P}_m$ and a universal reduced scattering coefficient for all the samples were adjusted until the best squared error fit (an additional weighting factor of 20 was given to the error between 450nm and 590nm) between measured and modeled results as achieved. The reason for the additional weighting factor is this area of the reflectance spectra is its domination by both oxygenated and deoxygenated hemoglobin absorption (especially for fair skin). We are

31

then able to more accurately assess the amount of oxygenated and deoxygenated hemoglobin in skin if our error function is given additional weight for this portion of the spectrum. The amount of hemoglobin in skin and the ratio of oxygenated versus deoxygenated hemoglobin control the shape and amplitude of unique spectral features in this area of the spectrum as discussed in Section 2.4.2.4. Specific layer depth information was used as measured from the samples, vice the universal measurements in Table 4. Each of the model components was constrained by typical ranges described in the literature as specified in Table 7.

The first assumption we make is that values for A and B exist that correctly define the parameters for the scattering coefficient spectra. The next assumption is the existence of a vector $\mathbf{P}_m$ that minimizes the mean square error between the mth modeled reflectance $(\Omega(\lambda, A, B, \mathbf{P}_m))$ and measured reflectance $M_m(\lambda)$. It should be noted that the values in the vector $\mathbf{P}_m$ are constrained so as not to exceed what is biologically possible for skin. Using simulated annealing, A, B, and $\mathbf{P}_m$ for $m = 1...76$ are adjusted until the error, defined as:

$$
\begin{aligned}
\text{E} = {} & \frac{1}{76} \sum_{m=1}^{76} \int_{450\text{nm}}^{460\text{nm}} \left(\Omega(\lambda, A, B, \mathbf{P}_m) - M_m(\lambda) \right)^2 d\lambda + \\
& \frac{20}{76} \sum_{m=1}^{76} \int_{460\text{nm}}^{590\text{nm}} \left(\Omega(\lambda, A, B, \mathbf{P}_m) - M_m(\lambda) \right)^2 d\lambda + \\
& \frac{1}{76} \sum_{m=1}^{76} \int_{590\text{nm}}^{1800\text{nm}} \left(\Omega(\lambda, A, B, \mathbf{P}_m) - M_m(\lambda) \right)^2 d\lambda
\end{aligned}
\tag{16}
$$

is minimized. When E is at or close to its minimum, the values A and B are used to define the scattering coefficient parameters as shown in Eqn. (17).

The parameter space was searched using a stochastic search algorithm, simulated annealing [20]. Simulated annealing models a physical annealing process, provides a local optimum solution, and the solutions tend to be robust. A regression on the resultant scattering coefficient yields the following functional form:

$$s'_{\text{dermn}} = 30447\lambda^{-1.283}. \tag{17}$$

A comparison of the reduced scattering coefficient estimated in this article and two others from the literature are shown in Fig. 13. The first estimate is based on Eqn. (18) from Jacques [35] (used in several existing skin models [8, 10, 44]):

$$s'_{\text{dermj}} = 2 \times 10^{12}\lambda^{-4} + 2 \times 10^{5}\lambda^{-1.5}. \tag{18}$$

The second estimate is based on measurements by Salomatina *et al.* in [72]. Our measurements of the reduced scattering coefficient reside below these two. Similar to the absorption coefficients described earlier, there is a wide variation in skin coefficients. Once again, this wide variation can be accounted for by the different methods, materials, and assumptions made by the different researchers. Like the absorption coefficient calculated for this work, the purpose of the scattering coefficient derived here is for use in an engineering model of skin reflectance.

2.4.4 Subcutaneous tissue reflectance. The reflectance of subcutaneous tissue is the final optical property considered for our model. Because of a combination of low scattering and low absorption for skin tissue in some areas of the spectrum, skin transmittance can be significant. Salomatina *et al.* [72] measured skin transmittance as high as 40% for a 3mm thick section of abdominal skin. This suggests that a significant amount of light can transmit through skin, reflect off subcutaneous tissue, and transmit back out through the surface. As will be shown in Section 2.6.9, the presence of subcutaneous tissue can increase the reflectance of skin by more than 15% in the NIR.
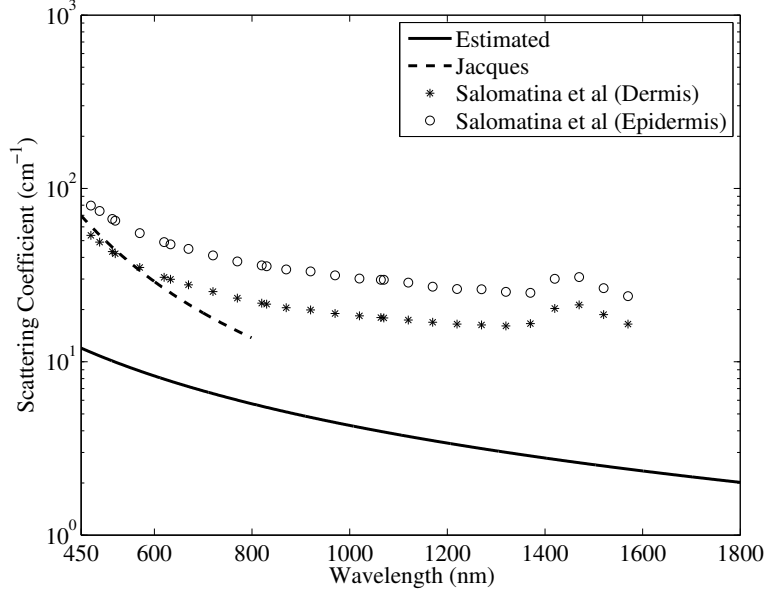
Figure 13: Reduced scattering coefficient for the epidermis and dermis estimated in the current work (solid), estimated by Jacques (dashed) [35], and measured by Salomatina *et al.* (asterisks for dermis and circles for epidermis) [72].

To characterize the diffuse reflectance of subcutaneous tissue (R_{sub}), reflectance measurements were collected from eight cadavers (four of these reflectance spectra are shown in Fig. 14). The reflectances measured have a high degree of similarity with varying amplitudes. In the visible region of the spectrum, the effect of different amounts of hemoglobin with different levels of oxygenation is clearly visible from approximately $400\text{nm} \leq \lambda \leq 600\text{nm}$. Large amounts of oxygenated hemoglobin result in the ω-shaped absorption feature at approximately 580nm while a lack of hemoglobin results in an overall higher reflectance in the region $400\text{nm} \leq \lambda \leq 600\text{nm}$. Even though there is a wide variation in subcutaneous reflectance in the VIS, it does not significantly affect skin reflectance in this region of the spectrum. This will be demonstrated in Section 2.6.9. Water absorption and lipids begin to dominate the reflectance of subcutaneous tissue beyond 1000nm. Water and lipid absorption account for the pattern of local maxima at 1100nm, 1280nm, and 1620nm and local minima in the reflectance of subcutaneous tissue at 1180nm and 1400nm.
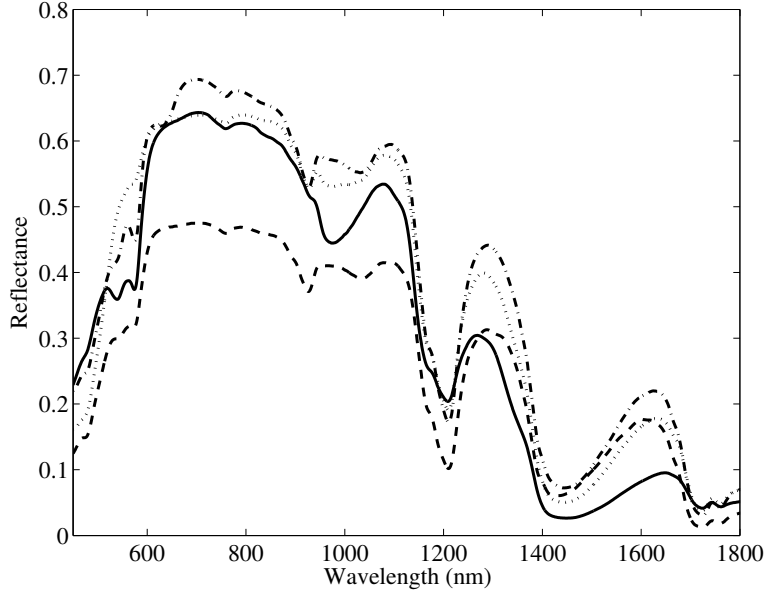
Figure 14:   Reflectance of subcutaneous tissue for four different cadavers.

To simplify the final layer of the model, the subcutaneous tissue is defined by a characteristic spectrum and a scale factor. The characteristic spectrum, shown in Fig. 15, is the mean of several subcutaneous tissue spectra which is then scaled so $\max(R_{sub}) = 1$. This spectrum is then scaled by a factor that ranges from 0.45 to 0.7, which corresponds with the maximum and minimum reflectances of the measured subcutaneous tissue reflectances.

To determine the accuracy of the characteristic subcutaneous reflectance spectrum, we adjusted the scale factor for the best fit. The worst case absolute difference is shown in Fig. 16. The largest difference between the scaled characteristic spectra and the measured spectra is less than 7.5%. These differences can come from several sources, including different thicknesses of the subcutaneous fat layer and different types of subcutaneous fat such as white adipose tissue or brown adipose tissue. To determine a more accurate subcutaneous tissue reflectance requires a more extensive characterization of the optical properties of the subcutaneous tissue which is beyond the scope of this dissertation.
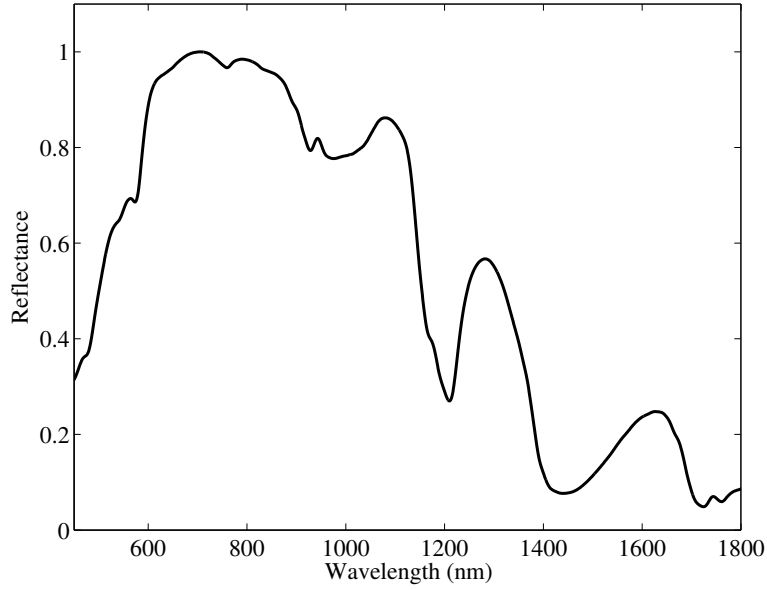
Figure 15: Mean reflectance of subcutaneous tissue scaled so its maximum value is one.
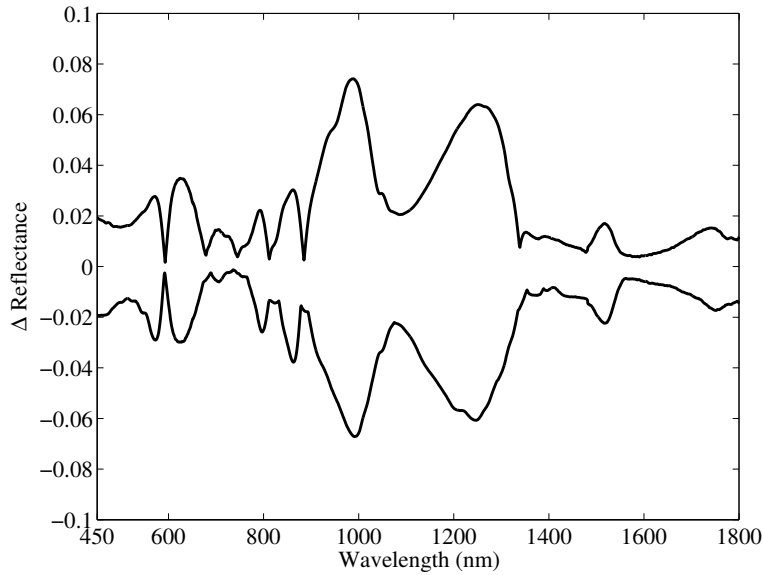
Figure 16: Maximum absolute difference envelope for measured and modeled subcutaneous reflection.

2.5 A model of human skin

The skin reflectance model described here is based on three main sources. Meglinski and Matcher [53] list the skin layers, their nominal thicknesses, and water content (Table 4). A report by Jacques [35] describes the absorption and scatter-

Table 4:   Skin layer depths and water percentages for the Meglinski and Matcher skin model [53].

Layer (m)	$\approx$ Depth (d)	Water (w)
Stratum Corneum (1)	20-80μm	5%
Stratum Lucidum (2)	10μm	20%
Stratum Granulosum (3)	10μm	20%
Stratum Spinosum (4)	45μm	20%
Stratum Basale (5)	15μm	20%
Papillary Dermis (6)	150μm	50%
Upper Blood Net Dermis (7)	80μm	60%
Reticular Dermis (8)	1000-3000μm	70%
Deep Blood Net Dermis (9)	80μm	70%

ing parameters of the skin. The final source is this dissertation, specifically collagen absorption measurements, empirical reflectance measurements of subcutaneous tissue from cadavers, and re-estimation of the reduced scattering coefficient of the epidermis described previously in Section 2.4.3.

2.5.1   Model parameters.   It should be noted that the model described here represents skin of "normal" thickness such as the forehead, abdomen, or thigh, and not "thick" skin such as the back, which has a dermis twice as thick as normal skin [60]. Another type of skin is the skin of the palm of the hand or the sole of the foot, which has a stratum corneum that is several times thicker than normal skin [60]. Table 4 lists the tissue thickness and water content for each layer from [53]. These are typical parameters and several factors affect them. Soaking skin in water, for example, would change the water content of the stratum corneum. A scale model of skin thickness from the abdomen, an extension of the Meglinski and Matcher model [52] which adds the upper blood net dermis and the deep blood net dermis, is shown in Fig. 17.

2.5.2   Fresnel reflection.   The amount of Fresnel reflection and transmission (r_0 and t_0) sum to one with the Fresnel reflection calculated from Eqn. (7). For the
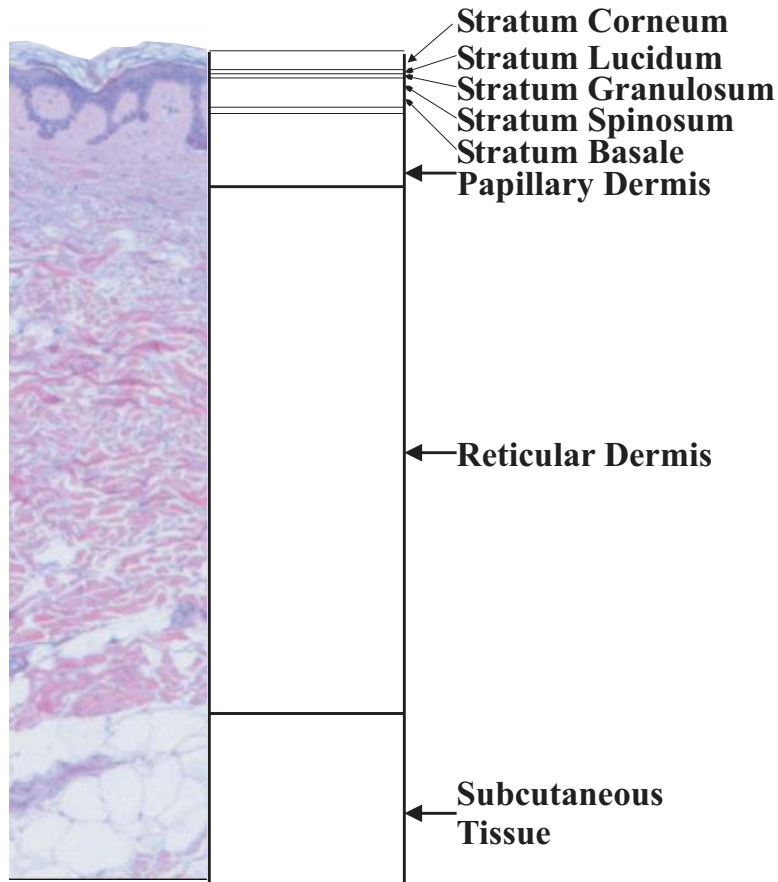
Figure 17: Magnified image of skin sample along side Meglinski and Matcher model [52] with the following additional layers in the epidermis: stratum lucidum, stratum granulosum, stratum spinosum, and stratum basale. Actual depth of skin sample shown in the image is approximately 1.2mm.

air/stratum corneum interface, $r_0 = 0.04$ and $t_0 = 0.96$. The Fresnel reflection for the other tissue layers ranges from 3×10^{-6} to 3×10^{-3}. These values are small and do not contribute significantly to the model results and are therefore not considered in this model.

2.5.3 Absorption and scattering coefficients. The absorption coefficient of each skin layer is based on the abundance of a given absorber and the absorption features of that absorber. In other words the total absorption of a layer is modeled as the sum of the absorption of the constituent components of a layer. The constituent components include water, collagen, melanosomes, and blood. Within blood are chro-

mophores such as oxygenated hemoglobin, deoxygenated hemoglobin, bilirubin, and betacarotene. Within the epidermis is a limited amount of betacarotene.

For the nth layer, the fraction of blood, water, collagen, and melanosomes are described as b_n, w_n, c_n, and v_n respectively. Typical values of w_n are listed in Table 4, $c_n = 1 - w_n - v_n$, and $v_n = 0$ for $n \neq 4, 5$ (in other words, melanosomes only exist in layers 4 and 5).

The absorption coefficient of the stratum corneum (layer 1) is modeled as a combination of the absorption of water, collagen, and betacarotene as:

$$a_1(\lambda) = c_1 a_{\text{col}}(\lambda) + w_1 a_{\text{wat}}(\lambda) + a_{\text{ce}}(\lambda) \tag{19}$$

where a_{wat} is the absorption of water defined in Section 2.4.2.1, a_{col} is the absorption of collagen defined in Section 2.4.2.2, and a_{ce} is the absorption of a typical amount of betacarotene in the epidermis (defined in Section 2.4.2.5). These variables are used to calculate the total absorption coefficient for subsequent layers in the epidermis

The absorption coefficient of the layers of the epidermis (layers 1-5) are modeled as a combination of the absorption of water, collagen, betacarotene, and melanosomes as:

$$a_n(\lambda) = a_{\text{mel}}(\lambda) v_n + a_{\text{col}}(\lambda) c_n + w_n a_{\text{wat}}(\lambda) + a_{\text{ce}}(\lambda) \tag{20}$$

where a_{mel} is the absorption of melanosomes and is defined in Section 2.4.2.3.

The absorption coefficient for the layers of the dermis (layers 6-9) are modeled as a combination of the absorption of water, collagen, oxygenated hemoglobin, deoxygenated hemoglobin, bilirubin, and betacarotene as:

$$a_n(\lambda) = a_\text{col}(\lambda)(c_n) + (w_n + 0.9b_n)a_\text{wat}(\lambda)$$

$$+ \left(a_\text{ohb}(\lambda)\gamma + a_\text{dhb}(\lambda)\left(1 - \gamma\right) + a_\text{car}(\lambda) + a_\text{bil}(\lambda)\right)b_n \tag{21}$$

where γ is the fraction of oxygenated hemoglobin and $(1 - \gamma)$ is the fraction of de-oxygenated hemoglobin. Absorption characteristics for hemoglobin (a_ohb and a_dhb), bilirubin (a_bil), and betacarotene (a_car) in blood are described in Section 2.4.2.4 and Section 2.4.2.5. Since whole blood consists of 90% water, its additional contribution due to water absorption is also considered and appears as the term $0.9b_n$ in Eqn. (21).

The reduced scattering coefficient for each layer of tissue is defined as:

$$s_n(\lambda) = s_\text{dermn}(\lambda)\frac{c_n}{0.3}. \tag{22}$$

The assumption made here is that the amount of scattering is directly proportional to the fraction of collagen in the dermal tissue. Scattering is modeled as the baseline reduced scattering coefficient multiplied by the fraction of material in the layer that is collagen divided by 0.3. The baseline reduced scattering coefficient is equal to the maximum possible amount of scattering in the dermis since the maximum fraction of collagen in the dermis is equal to 0.3.

2.5.4   Subcutaneous tissue reflectance.   The last layer of the model (layer 10), as shown in Fig. 17, is a layer of subcutaneous tissue. A simplification of the model is made by assuming this layer is infinitely thick. As such, we only need to know the reflectance of this tissue and need not worry about the amount of light transmitted through it.

Table 5:   Description of parameters in the skin reflectance model.

Parameter	Model Parameter Description
Melanosome (%)	Percent melanosomes in the epidermis
Blood Level (%)	Percent blood in the dermis
Oxygenation (%)	Percent oxygenation of the hemoglobin in the blood
Derm. Depth (cm)	Depth of the reticular dermis
Collagen (%)	Percent collagen in the reticular dermis
Sub. Scale	Scale factor for the characteristic subcutaneous reflection

2.5.5   Skin reflectance model: incorporating optical properties.   The skin reflectance model is constructed of the elements described in Section 2.2.1. The values of r_0 and t_0 are calculated from the Fresnel equation covered in Section 2.2.1. The values of r_n and t_n for $n = 1...N - 1$ are calculated from the Kubelka-Munk equations (Eqn. (1) and (2) respectively), using the absorption and scattering coefficients for the respective layers described in Section 2.5.3 as well as the tissue layer depths from Table 4. The values for r_N were determined by laboratory measurements as discussed in Section 2.5.4. For this work, $N = 10$. The reflectances and transmittances are used with Eqn. (10) and Eqn. (11) to determine the total reflectance of skin as described in Section 2.2.3. In Section 2.4.3, the skin reflectance model is described as the function $\Omega(\lambda, \mathbf{P}_m)$ where $\mathbf{P}_m$ is a vector of six parameters that describe the reflectance of the mth skin sample. Table 5 gives a brief description of each of these parameters.

2.6   *Exploring tissue variation effects on the reflectance model output*

In this section, we investigate the affect of adjusting various parameters in the skin reflectance model. This gives insight into how each parameter of the model affects skin reflectance as a function of wavelength. Adjusting the concentrations and distributions of different constituents of skin can have a minor affect on the reflectance of skin in one area of the spectrum and a strong affect in another. Unless otherwise stated, the parameters used in the model for Type I/II skin are 2.4% melanosomes,

0.5% blood throughout the dermis, 30% collagen in the dermis, a dermal thickness of 0.15cm, and a 75% oxygenation level for hemoglobin in the blood.

2.6.1 Melanosome level. Figure 18 shows a comparison of model results for Type I/II and Type V/VI skin. The parameters for Type V/VI are the same as Type I/II skin except for the melanosome level of 24%. As the melanosome level increases, the reflectance of skin decreases across the VIS and NIR. The decrease in reflectance is greater for the VIS region of the spectrum versus the NIR. If the melanosome level is high enough, the affect of hemoglobin absorption is no longer a factor.
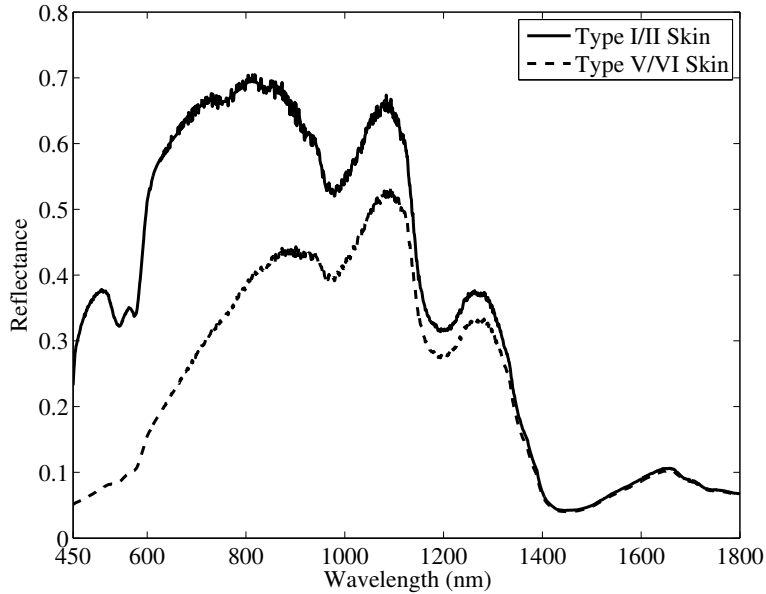
Figure 18: Modeled skin reflectance for Type I/II skin (melanosome level of 2.4%) and Type V/VI skin (melanosome level of 24%).

2.6.2 Redistribution of melanosomes. Melanin is made in the stratum basale, which is the deepest layer of the epidermis, and is transported throughout the rest of the epidermis in melanosome organelles (see Fig. 17) [55]. The concentration of melanosomes is higher at the stratum basale versus the other layers of the epidermis [55]. However, the current skin model uses a uniform distribution of melanosomes throughout the epidermis. To determine the effect of redistributing melanosomes, we examine a uniform distribution of melanosomes throughout the epidermis (see Section

2.6.1) and a concentration of all the melanosomes in the stratum basale. For both cases, melanosomes constitute the same overall percentage of the epidermis. The difference in reflectance between the uniform and concentrated distributions for Type I/II skin and Type V/VI is shown in Fig. 19. In general, the uniform distribution has a lower reflectance than the concentrated distribution, especially in the VIS. Furthermore, the difference between the two distributions increases as the melanosome level increases. The maximum difference in skin reflectance for the different distributions is approximately 1% for Type I/II skin and 2% for Type V/VI skin..
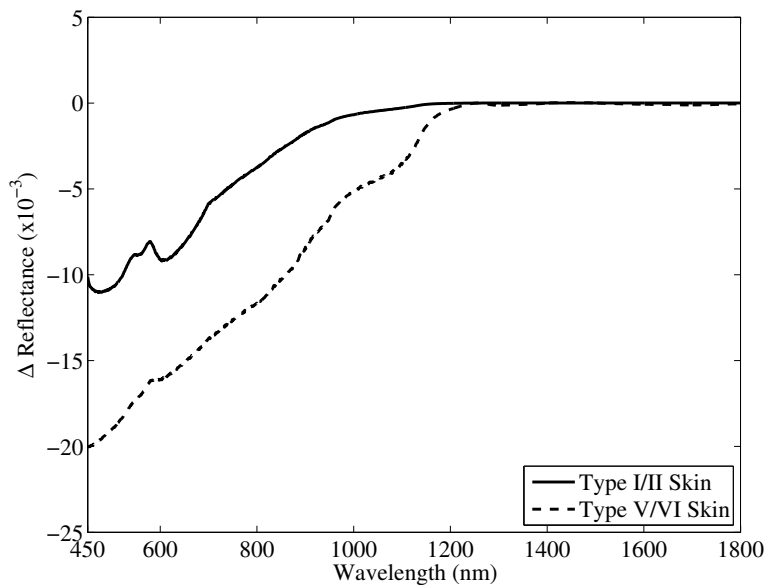
Figure 19:   Difference in modeled skin reflectance for a uniform distribution of melanosomes in the epidermis versus the same volume of melanosomes concentrated in the stratum basale. Difference is shown for Type I/II skin (solid) and Type V/VI skin(dashed).

2.6.3 Blood level.   Figure 20 shows a comparison of model results for skin with blood concentrations of 0.5% and 0% throughout the dermis for Type I/II and Type V/VI skin. Different conditions such as strong emotions, sickness, or injury can affect the concentration of blood in skin, giving it a stronger reddish tint for higher concentrations or an ashen tint for lower concentrations. These conditions are only visible if the amount of melanosomes in the epidermis is at weak concentrations so

as not to obscure the affects of hemoglobin absorption. Since hemoglobin is not a significant absorber in the NIR, the reflectance of skin in this portion of the spectrum is very similar to the case where skin has blood.
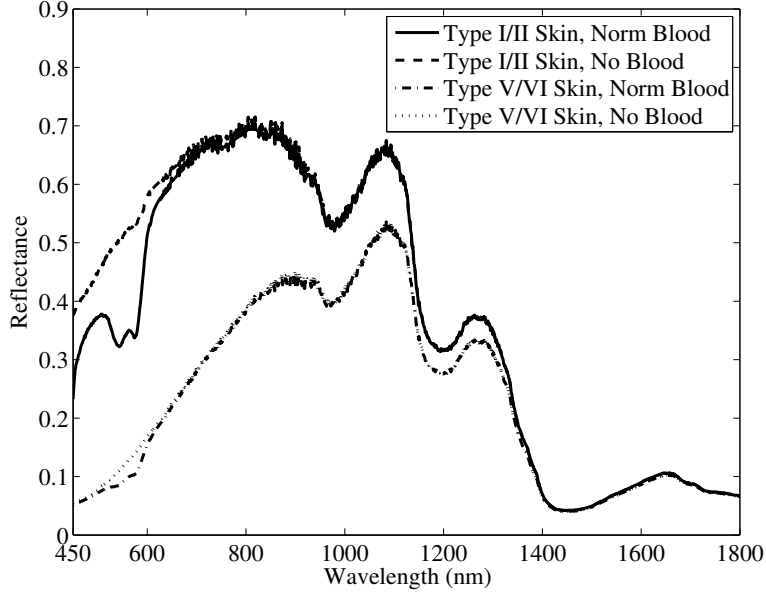
Figure 20:   Modeled skin reflectance for a typical concentration of dermal blood and without dermal blood. Reflectance is shown for Type I/II skin with normal concentration of blood (solid), Type I/II skin without blood (dashed), Type V/VI with normal concentration of blood (dashed-dotted), and Type V/VI without blood (dotted).

2.6.4 Redistribution of blood.   Although differing amounts of blood in the dermis are known to significantly affect the spectra of skin, the affect that different distributions of blood in the dermis have on the spectra of skin is not described in the existing literature. Blood is concentrated just below the papillary dermis in the upper blood net dermis and just below the reticular dermis in the lower blood net dermis [53]. A comparison of skin reflectance spectra using the two different blood distributions described in Table 6 is made. By observation, the percentage of the dermis consisting of blood is 0.51% for the first distribution. To determine the percentage of the dermis consisting of blood for the second distribution, one must sum the product of the depth and percent blood for each layer and then divide the result by the total depth of the

44

Table 6: Depths and blood percentages for dermal layers for different blood distributions [53]

Layer	Depth (μm)	Dist. 1 (%)	Dist. 2 (%)
Papillary Dermis	150	0.51	0.4
Upper Blood Net Dermis	80	0.51	3.0
Reticular Dermis	2000	0.51	0.4
Deep Blood Net Dermis	80	0.51	1.0

four layers. The result is once again 0.51 %. In other words, both distributions have the same amount of blood in the dermis.

For the second distribution, blood in the different layers is in the same proportions, although in smaller concentrations, as the Meglinski and Matcher model [53]. Figure 21 shows the affect of uniformly distributing blood throughout the dermis rather than distributing it at different concentrations for different layers of skin. Beyond 750nm, the difference in reflectance between the two distributions is not significant. Below 750nm, the difference in reflectance is up to 1.2% for Type I/II skin and 0.2% for Type V/VI. Increased amounts of blood closer to the surface of skin for the second distribution increases the overall absorption of light in the VIS. As melanosome levels increase, this affect is attenuated since melanosomes in the epidermis allow less light to reach and reflect from the dermis.

2.6.5 Oxygenation level.   Figure 22 shows the difference in the reflectance of skin with 100% oxygenated hemoglobin and 100% deoxygenated hemoglobin for two different levels of pigmentation. Below 500nm, skin with oxygenated blood has a lower reflectance than skin with deoxygenated blood while from 600-780nm, skin with oxygenated blood has a higher reflectance. This combination of features gives skin with excessive amounts of deoxygenated blood a bluish tint and excessive amounts of oxygenated blood a reddish tint. The characteristic ω-shape absorption feature of oxygenated blood between 500-600nm is also one of the major differences between skin with oxygenated versus deoxygenated blood. Beyond 780nm, hemoglobin absorption
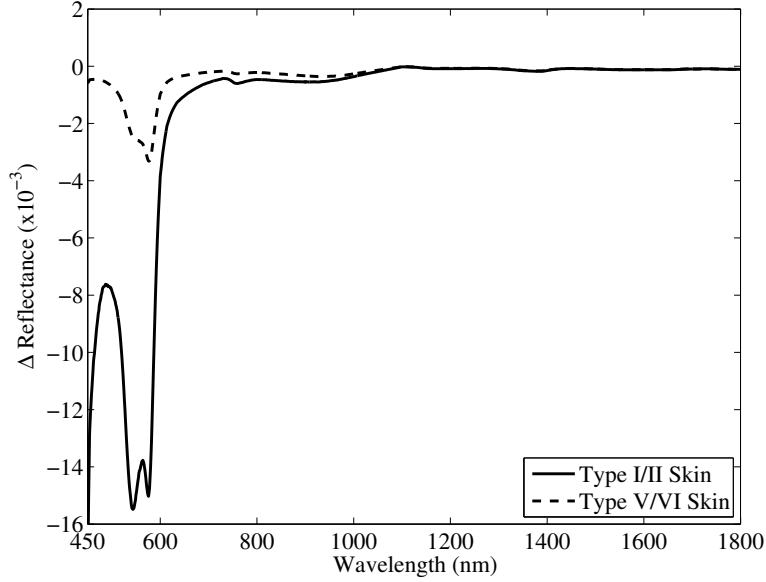
Figure 21: Difference in modeled skin reflectance for an even distribution of blood in the dermis versus the same amount of blood in the papillary dermis, upper blood net dermis, reticular dermis, and deep blood net dermis at concentrations of 0.4%, 3%, 0.4%, and 1% respectively (see Table 6). Difference is shown for Type I/II skin (solid) and Type V/VI (dashed).

of both skin types becomes less significant and the difference between skin with either type of hemoglobin is very small. Melanosomes attenuate hemoglobin absorption since it exists in the epidermis (above the dermis) where hemoglobin is present. This can be seen when comparing the difference in the spectra for the two different oxygenation levels for skin with 2.4% melanosomes versus skin with 24% melanosomes.

It is important to note that hemoglobin in the body is actually a combination of oxygenation and deoxygenated hemoglobin. Hemoglobin typically has an oxygenation level of 75%. This mixture results from arteries carrying approximately 100% oxygenated hemoglobin from the lungs and veins returning a mixture of approximately 50% oxygenated hemoglobin and 50% deoxygenated hemoglobin to the lungs for oxygenation. While on average blood is oxygenated 75% throughout the body, large variations in oxygenation level can occur at the surface of skin [88].
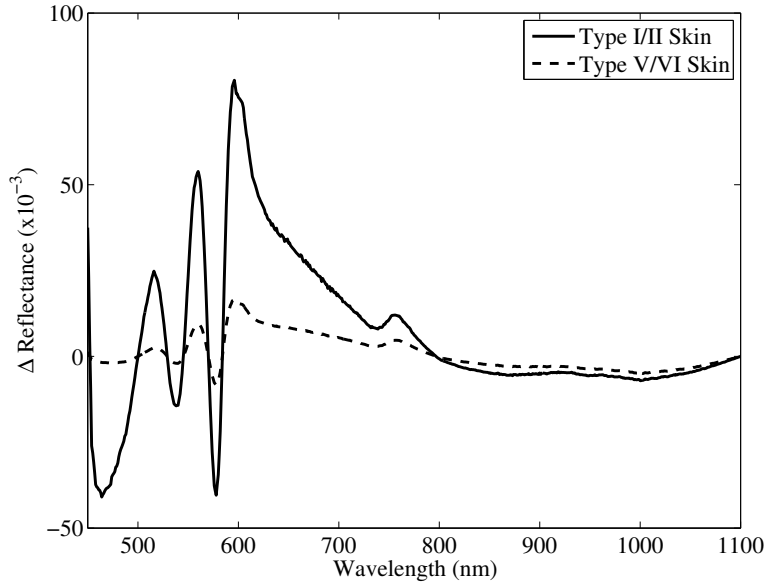
Figure 22:   Difference in modeled skin reflectance for skin with a typical concentra-
tion of blood where all the hemoglobin is oxygenated versus the case where all the
hemoglobin is deoxygenated. Difference is shown for Type I/II skin (solid) and Type
V/VI skin (dashed).

2.6.6   Dermal thickness.   In general, thin skin has a higher reflectance than
thick skin. This is because thinner skin is more transparent and the highly reflective
subcutaneous tissue becomes more of a factor in the total reflectance of areas with
thinner skin. Figure 23 shows the difference in reflectance for dermal thicknesses
of 3mm and 1.5mm for both Type I/II and Type V/VI skin. Between 600nm and
1200nm, the reflectance spectra of thin skin is higher than thick skin for a given pig-
mentation level, while outside of this range, the reflectance spectra are approximately
the same.

2.6.7   Collagen.   The amount of collagen in skin can vary from 15-30% of
the dermal tissue. The general trend is for younger people to have higher levels of
collagen in their skin versus older people. Since collagen has a higher absorption
in the VIS, skin with more collagen has a lower reflectance over this region of the
spectrum. Figure 24 shows the difference in the reflectance spectra of skin with 30%
collagen and 15% collagen for Type I/II (solid) and Type V/VI (dashed). Between
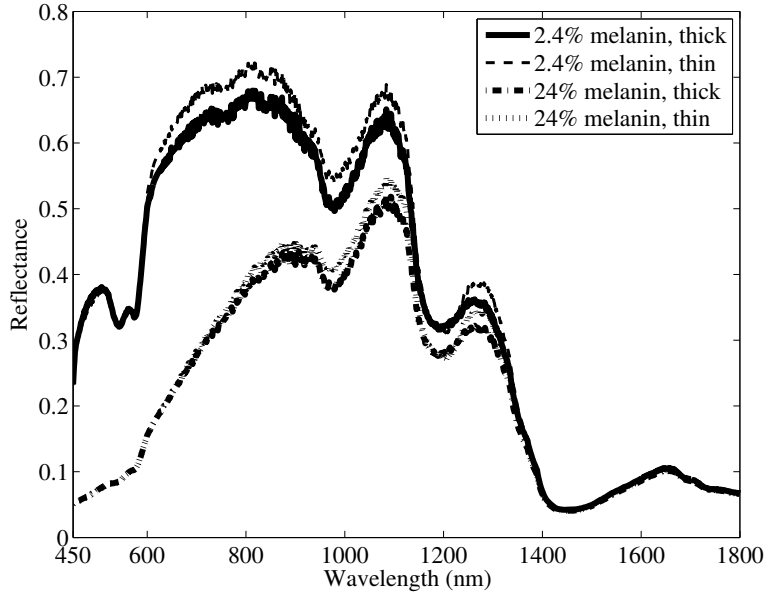
Figure 23:   Modeled skin reflectance for Type I/II skin with a dermal thicknesses of 3mm (solid), Type I/II skin with a dermal thicknesses of 1.5mm (dashed), Type V/VI skin with a dermal thicknesses of 3mm (dashed-dotted), and Type V/VI skin with a dermal thicknesses of 1.5mm (dotted).

600-1000nm, where melanosome, hemoglobin, and water absorption do not dominate, reduced collagen content makes the skin more transparent. This is due to the reduced amount of collagen absorption, where increases in the reflectance of skin are due to the highly reflective subcutaneous fat beneath the skin. The difference in reflectance for Type V/VI skin is smaller since less light makes it through the epidermis to reflect off the dermis.

2.6.8   The effect of including the stratum lucidum and stratum granulosum.

The stratum lucidum and stratum granulosum are very thin layers just below the stratum corneum going through a process of keratinization where parts of the cells are being replaced by keratin. Because of this, we assume that the water content is between that of the stratum spinosum and the stratum corneum. The Meglinski and Matcher model [52] assumes that the water content in these two layers matches that of the stratum spinosum at 20%. The other extreme would then match the water content in the stratum corneum at 5%. Figure 25 shows the difference in modeled
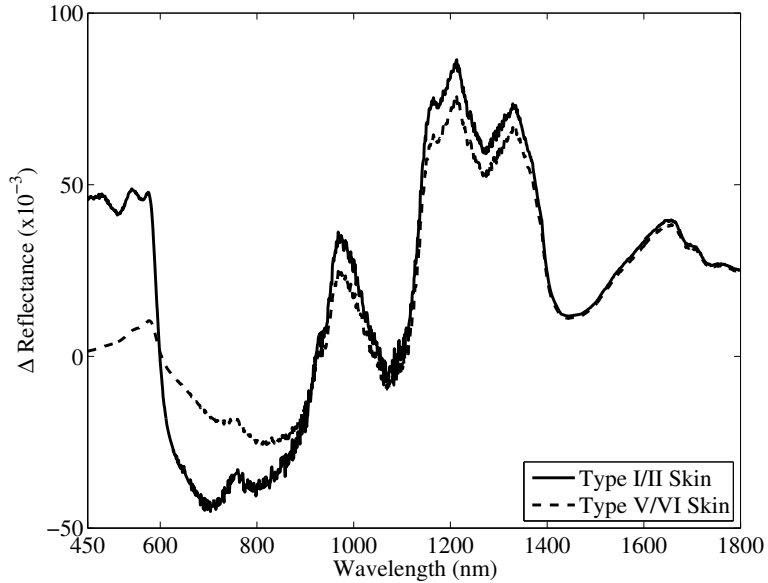
Figure 24:   Modeled difference in skin reflectance for skin with 30% collagen versus skin with 15% collagen. Difference is shown for Type I/II skin (solid) and Type V/VI skin (dashed).

reflectance for these two different water levels for the stratum lucidum and stratum granulosum. For both fair skin and dark skin, the difference in reflectance between the two extremes of water content is less than 1×10^{-3} (0.1%). Increasing the amount of water, while simultaneously reducing collagen by a corresponding amount, has the overall affect of decreasing absorption in the VIS and increasing absorption in the NIR. This accounts for the fact that increasing the water content in these layers has the affect of increasing reflectance in the VIS and reducing reflectance in the NIR. Increasing the melanosome level of the skin reduces these differences slightly in the VIS since the reflectance of the dermal tissue below the melanosomes in the epidermis is not as much of a factor. The difference in reflectance is less than 0.1% over the entire spectrum for the full range of melanosome levels and does not significantly affect the model.

2.6.9   The effects of subcutaneous tissue.   Figures 26 and 27 show the affect of scaling the subcutaneous reflectance shown in Fig. 15 by a factor of 75%, 50%, and 0%. Subcutaneous reflection is not significant for 600nm $\leq \lambda \leq$ 1350nm. For

49
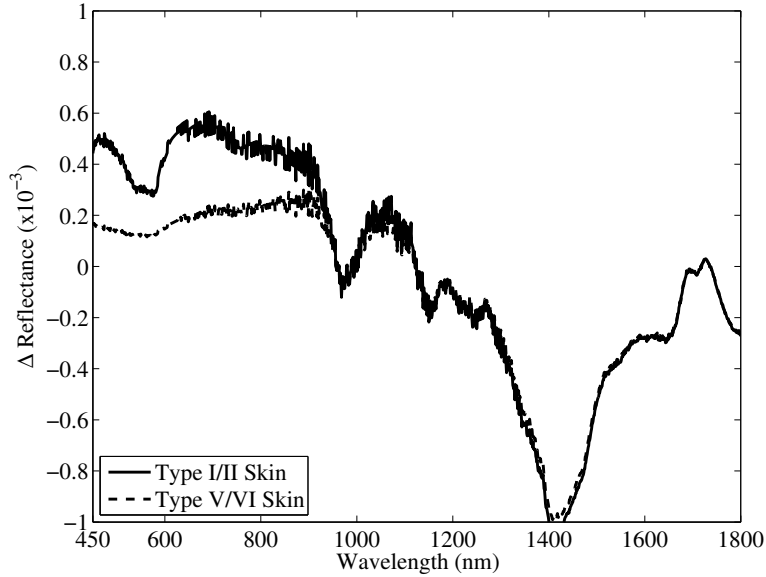
Figure 25: Difference in modeled skin reflectance for skin with 20% water versus 5% water in the stratum lucidum and stratum granulosum. Difference is shown for Type I/II skin (solid) and Type V/VI skin (dashed).

$600\text{nm} \leq \lambda \leq 1350\text{nm}$, the transmittance of skin is fairly high because the absorption of collagen and the chromophores of skin is fairly low in this range. Beyond 1350nm, water absorption is significant and most of the incident light energy is absorbed.
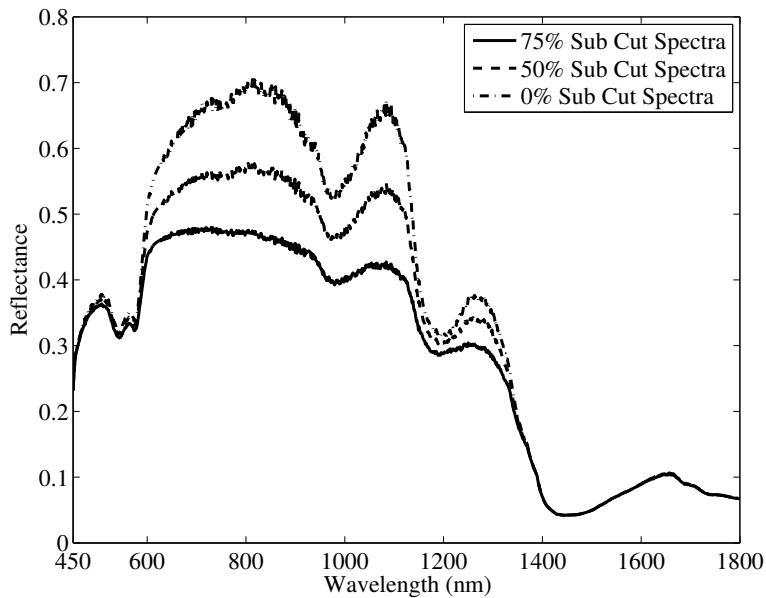
Figure 26: Modeled Type I/II skin reflectance for characteristic subcutaneous reflectance spectra scale factors of 75% (solid), 50% (dashed), and 0% (dashed-dotted).
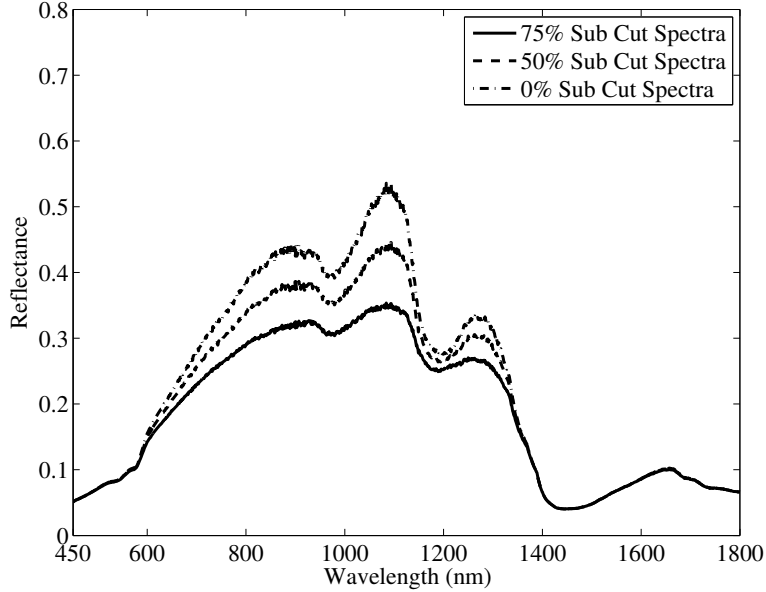
Figure 27: Modeled Type V/VI skin reflectance for characteristic subcutaneous reflectance spectra scale factors of 75% (solid), 50% (dashed), and 0% (dashed-dotted).

2.6.10 Comparison of our reflectance skin model results using absorption and scattering coefficients described in this dissertation and existing literature. Figures 28 and 29 show a comparison of results using three sets of absorption and scattering coefficients for Type I/II skin and Type V/VI skin respectively. For Fig. 28, each set of results uses the same melanosome level of 2.4%, blood percentage of 0.5%, and oxygenation level of 75%. For Fig. 29 the same holds except a melanosome level of 24% is used. The skin thicknesses used for the results are based on values described by Meglinski and Matcher in [52] (Table 4). The absorption and scattering coefficients described by Jacques in [35] and Salomatina *et al.* in [72] result in a modeled reflectance significantly higher than the modeled reflectance calculated from our estimates of the absorption and scattering coefficients which are based on our measurements of collagen absorption and measurements collected from living and cadaver skin.
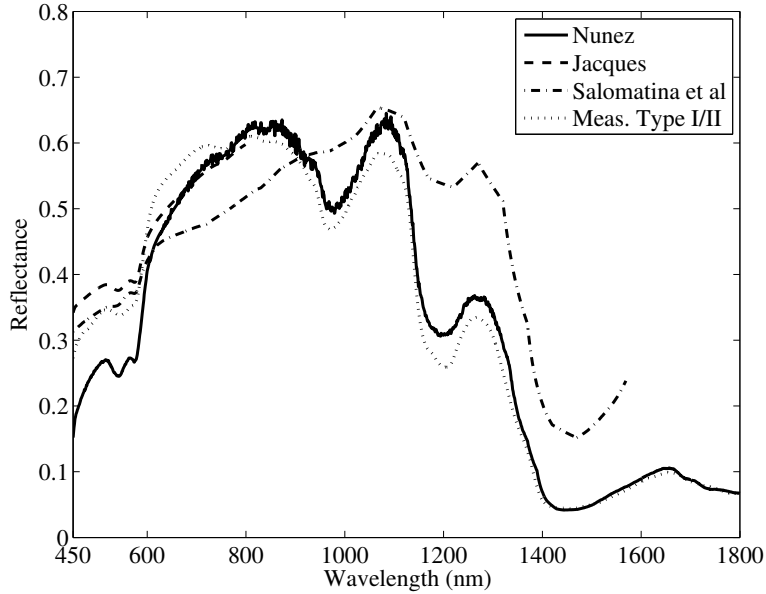
Figure 28:   Measured Type I/II skin reflectance and modeled Type I/II skin reflectance using scattering and absorption coefficients developed in this dissertation (Section 2.6), described by Jacques in [35], and measured by Salomatina *et al.* in [72]. Parameters for the model were not adjusted for best match with measured data.
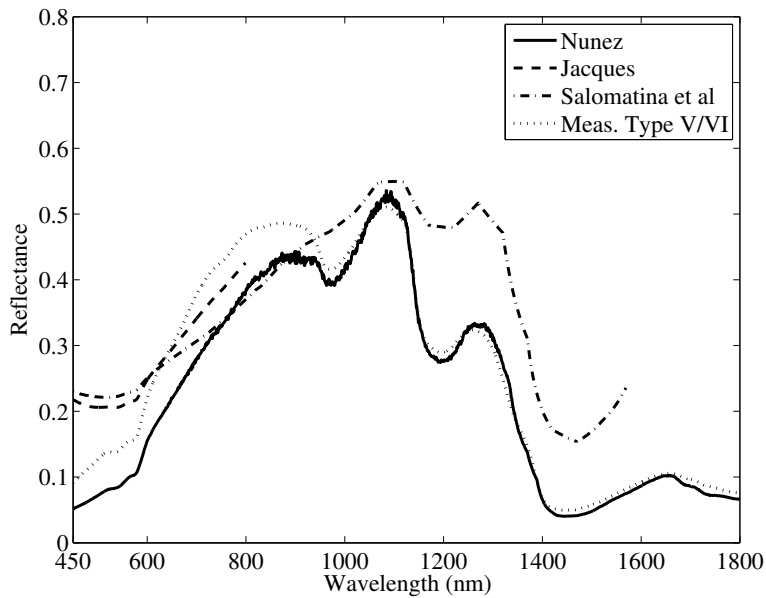
Figure 29:   Measured Type V/VI skin reflectance and modeled Type V/VI skin reflectance using scattering and absorption coefficients developed in this dissertation (Section 2.6), described by Jacques in [35], and measured by Salomatina *et al.* in [72]. Parameters for the model were not adjusted for best match with measured data.

Table 7: Minimum and maximum parameters for cadaver and living skin used in the skin reflectance model developed in this dissertation. Values are derived from the literature.

Parameter	cadaver min.	cadaver max.	living min.	living max.
Melanosome (%)	1.5	43	1.5	43
Blood Level (%)	0	1	0.25	1
Oxygenation (%)	0	90	20	90
Dermal Depth (cm)	n/a	n/a	0.1	0.3
Collagen (%)	15	30	30	30
Sub. Scale	0.51	0.65	0.62	0.65

2.7 Comparing skin reflectance model output with collected data

Reflectance measurements from two cadavers and two living subjects is compared against the model estimate of those same reflectance measurements. Melanosome levels, hemoglobin levels, hemoglobin oxygenation levels, collagen levels, dermal thickness, and subcutaneous reflectance were all adjusted to provide the best mean-square error fit with the measured data as described in detail in Section 2.4.3.

Parameters are constrained with the values in Table 7 with the resulting parameters shown in Table 8. Melanosome percentages in the epidermis are constrained based on values in Table 1. The blood levels were constrained based on the mean blood level estimated during the simulated annealing process. The constraints are half to double the estimated mean blood level. Oxygenation value constraints for living skin were based on values obtained from [88] while oxygenation values for cadaver skin were allowed to drop to 0%. The dermal depth constraint for the living skin samples come from [56] which measured the thickness of skin layers for the forearms of multiple subjects. For cadavers, dermal depths are measured. The range of subcutaneous reflectance values is constrained by the range of reflectance measurements of subcutaneous tissue collected for this work.

Both skin reflectance measurements for the cadavers came from skin with a low pigmentation level and a low hemoglobin level. The melanosome percentage levels for the cadavers may seem high when compared with the values described in Table 1 for different skin pigmentation levels. However, the values in Table 1 assume an epidermal thickness of 60μm while the epidermal thickness of the cadavers is a fraction of this and known. In other words, skin with a thinner epidermis requires a higher melanosome percentage versus skin with a thicker epidermis for both types of skin to have the same spectra. The blood level for both cadaver samples is also very low when compared with the amount of blood in living skin. After death, gravity can pull blood from skin and cause it to pool on the inside. The less blood at the surface of the skin the less meaningful the oxygenation values listed in Table 8 are. The extreme example of this is the case where there is no blood in the dermal tissue making the oxygenation values meaningless. The value used for the dermal depth parameter is measured from a skin core sample at the same location the reflectance measurement was collected. As such, this parameter is not made adjustable for the cadavers. The subcutaneous reflection for the cadavers is well within the bounds set in Table 7.

The two sample skin reflectance measurements for living people came from Type I/II skin and Type V/VI skin. The melanosome percentages for both skin Types correspond well with the values in Table 1. The blood level for the Type I/II skin is well within the set bounds while the value for the Type V/VI skin is at the maximum value. However, the melanosomes in the epidermis attenuate the affect of any blood in the dermis, making it difficult to obtain an accurate value for blood level. The oxygenation value for the Type I/II skin is well within the set bounds while, once again, the value for the Type V/VI skin is at the maximum value. For the same reason it is difficult to obtain accurate blood levels for highly pigmented skin, it is difficult to obtain the oxygenation level of the dermal blood. Changing the oxygenation level of darkly pigmented skin has very little affect on the reflectance spectra.

Table 8:   Parameters used in the skin reflectance model developed in this dissertation that provide the best match with sample pair of reflectance measurements from cadavers and sample pair of reflectance measurements from living skin.

Parameter	Cad. 1	Cad. 2	Live 1	Live 2
Melanosome(%)	10	18	2	28
Blood Level (%)	0	0	0.61	0.75
Oxygenation (%)	60	60	46	43
Derm. Depth (cm)	n/a	n/a	0.101	0.100
Sub. Factor	0.51	0.65	0.62	0.65

The skin depths applied to the model are shown in Table 9 where the skin layer thicknesses for the cadavers come from measurements of skin samples and for living people were a parameter in the model that provided the best fit with measured data.

Figures 30 and 31 compare skin reflectance measurements from fair-skinned cadavers generated using model results with optimized parameters. Both cadaver skin samples had few melanosomes and little blood so the effect of these chromophores on skin reflectance is dramatically reduced.
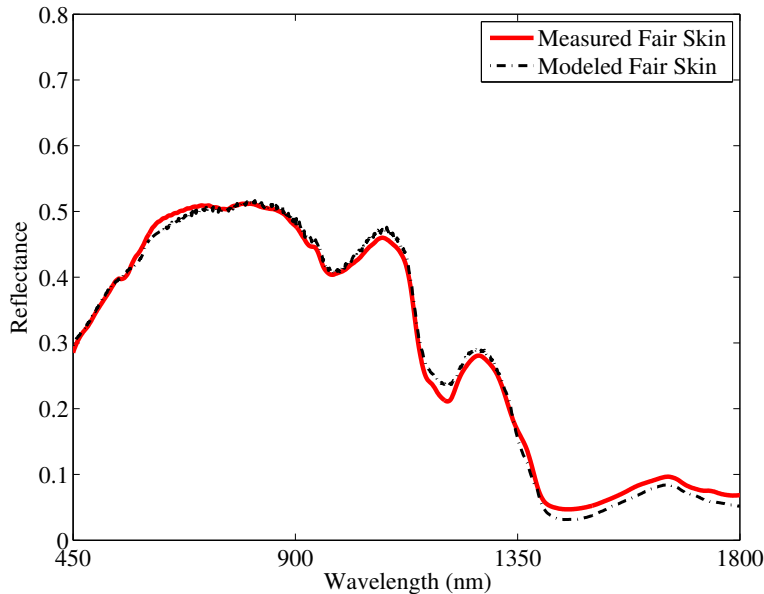
Figure 30:   Sample comparison of modeled and measured cadaver thick Type I/II skin reflectance. Selected sample has among the highest correlation between measured and modeled data for the cadaver measurements.

Table 9: Skin layer depths in cm used in the skin reflectance model developed in this dissertation for sample pair of reflectance measurements from cadavers and sample pairs of reflectance measurements from living skin. Cadaver skin layer depths are measured and living skin layer depths are from [53]

Layer	Cad. 1	Cad. 2	Live 1	Live 2
1	0.00425	0.0015	0.002	0.002
2	0.000338	0.000281	0.001	0.001
3	0.000338	0.000281	0.001	0.001
4	0.001519	0.001266	0.0045	0.0045
5	0.000506	0.000422	0.0015	0.0015
6	0.002513	0.0067	0.015	0.015
7	0.001238	0.0033	0.008	0.008
8	0.13062	0.08645	0.1520	0.1150
9	0.006875	0.00455	0.008	0.008
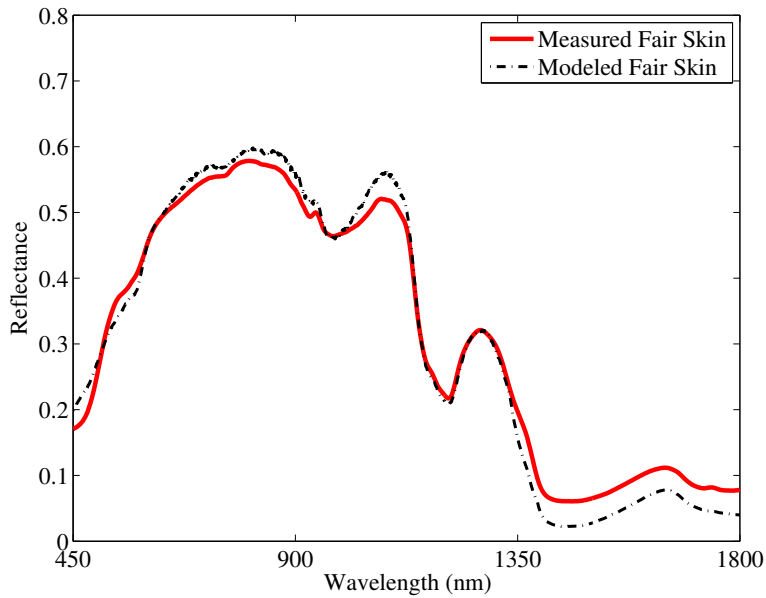
Figure 31: Sample comparison of modeled and measured cadaver thin Type I/II skin reflectance. Selected sample has among the highest correlation between measured and modeled data for the cadaver measurements.

Reflectance measurements from Type I/II skin and Type V/VI skin were selected for comparison with the model. Figures 32 and 33 show the resulting compar-

56

ison for Type I/II and Type V/VI skin respectively. Once again, model parameters are adjusted to provide the best fit with the measured data.
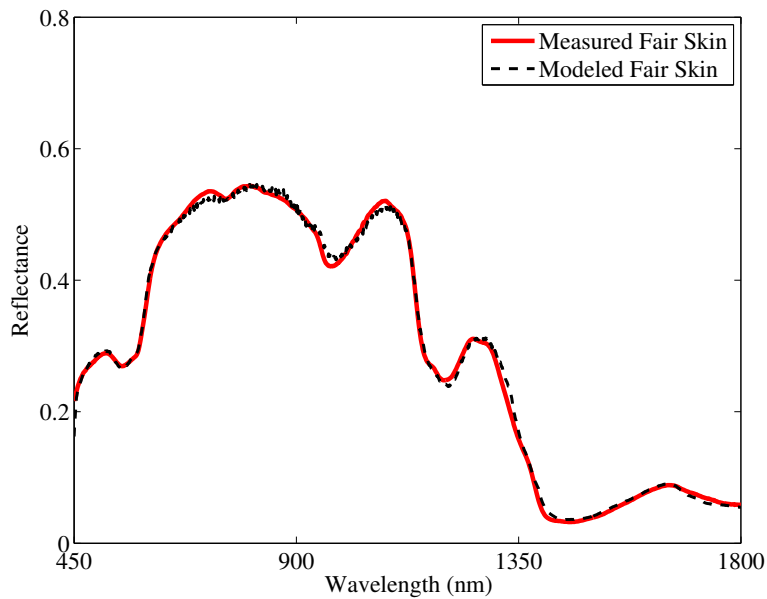
Figure 32:   Sample comparison of modeled and measured living thin Type I/II skin reflectance. Selected sample has a typical correlation between measured and modeled data for the living skin measurements.
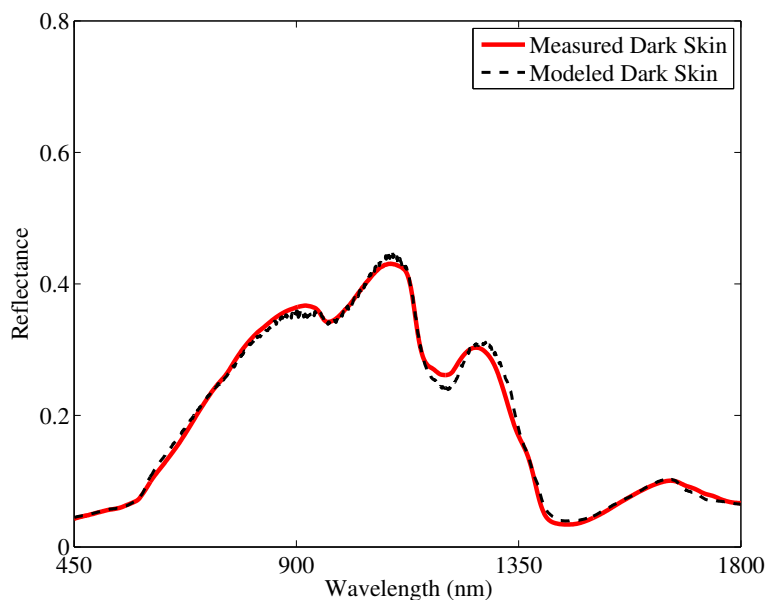
Figure 33:   Sample comparison of modeled and measured living thin Type V/VI skin reflectance. Selected sample has a typical correlation between measured and modeled data for the living skin measurements.

Table 10:   RMSE results between modeled and measured skin reflectances for living and cadaver skin.

Type	RMSE Mean	RMSE STD
Living	0.011159	0.004844
Living Type I/II	0.0093225	0.0021872
Living Type V/VI	0.016284	0.0079289
Cadaver	0.024345	0.012278
All	0.020199	0.012077

To determine the effectiveness of adjusting model parameters to make modeled reflectance match measured reflectance, the root mean square error (RMSE) between measured and modeled reflectance is calculated. The error function used earlier for matching modeled and measured data is based on the mean square error with the error from a portion of the spectrum (460nm-590nm) scaled by a factor of 20. However to provide a more intuitive comparison between measured and modeled data, the RMSE is used since its units are the same as reflectance. For the four examples described in this section (two cadaver measurements and two living measurements), the errors are 0.0083391, 0.0089603, 0.011885, and 0.026699, respectively. The mean and standard deviation for the RMSE for the reflectance measurements are presented in Table 10. The general trend was for the mean and standard deviation for the RMSE to be lower for the living skin reflectances versus the cadaver skin reflectances. The mean and standard deviation for the RMSE error was lower for the Type I/II living skin reflectances versus the the Type V/VI skin reflectances. A complete comparison of modeled and measured skin reflectances for all of the skin samples collected for this work can be found in Appendix C. This includes skin layers depths, model parameters, and figures showing modeled and measured skin reflectances.

Figure 34 shows the mean RMSE between measured and modeled data for all of the reflectance measurements (blue), all of the reflectance measurements from living people (red), and all of the reflectance measurements from cadavers (green). Two things to note are the majority of the reflectance measurements are from the cadavers

(52 out of the 76) and that the errors for the cadavers were greater overall than for the living skin reflectances. As such, the mean error for all of the reflectances was slightly less than that of the mean reflectance for the cadavers. The mean errors for both living and cadaver reflectances is fairly low before 600nm. The errors then rise significantly in the NIR before it drops significantly beyond 1350nm. The area between 600nm and 1350nm corresponds to a part of the spectra where the dermis and epidermis have a high transmittance and subcutaneous reflectance plays a significant role in the overall reflectance of skin.
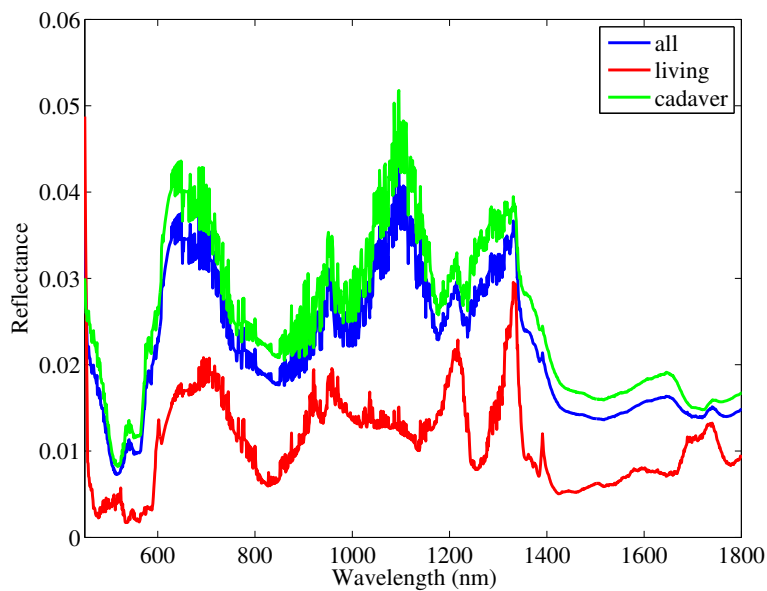
Figure 34: Average RMSE as a function of wavelength for living measured skin reflectances, cadaver measured skin reflectances, and combination of living and cadaver measured skin reflectances.

2.8 Distribution and sensitivity of parameters

A list of each set of model parameters that best fit the measured data are listed in Appendix C. To determine if the model is credible, a histogram of each parameter is generated using the parameter values determined for the living skin reflectances and the cadaver skin reflectances. Analysis of the sensitivity of the model output to input parameters is also done.

2.8.1 Distribution analysis of model parameters.   Figure 35 shows the collection of 6 histograms, one for each of the adjustable skin parameters, for the 24 skin reflectances of living subjects. The histogram for melanosome percentage shows the majority of the skin reflectances are for people with Type I/II skin with a limited number of people with Type III/IV/V/VI skin. This corresponds well with the fact that the majority of skin reflectances were collected from people with fair skin and only a few of the skin reflectances were collected from people with moderately pigmented to dark skin. The histogram for blood distribution shows that their was a wide variety of blood volumes in the living skin reflectances. These could be caused by a wide variety of conditions such as pressure on the skin from the measuring probe (blood would leave the skin) or heat from the light in the measuring probe (blood volume would increase in the skin). The histogram for oxygenation level shows a range of values from 20% to 40%. As stated in Section 2.4.2.4 and 2.7, these values correspond with oxygenation measurements others have reported [88]. The dermal depth is concentrated in the 0.1cm bin which corresponds to relatively thin skin. The reason for this observation is all of the measurements for living skin came from the subjects' forearms which has fairly thin skin. The collagen percentages covers the full range of 15% to 30%. The subcutaneous reflection scale factor covers the full range from 0.5 to 0.75 with a greater concentration at the top half of the range.

Figure 36 shows the histograms for 52 cadaver skin reflectances. The histogram for the melanosome percentages are concentrated on the bottom half of the percentages with what seems like an inordinate amount of the values concentrated in the region between 7% and 20%. This is because the epidermis for the cadavers are generally thinner than those from living people since cadavers are generally from older people with atrophied skin. The atrophied skin is thinner and as such has a greater concentration of melanosomes versus skin with a thicker epidermis and the same color. However, despite epidermis thickness, people with the same skin color would still have similar amounts of melanosomes in their skin. The histogram for the blood percentage shows the percentage of blood concentrated near 0%. This is because the blood in
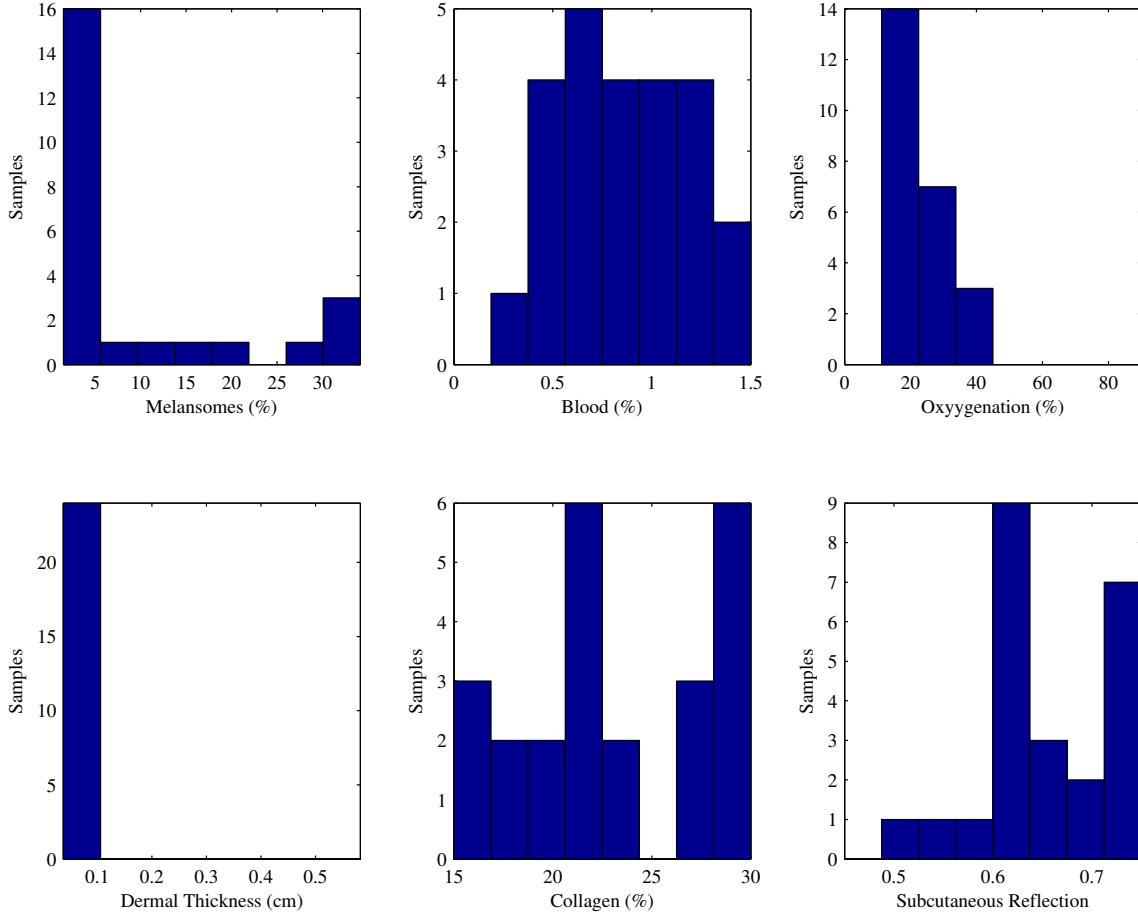
Figure 35: Histograms of the six model parameters used for the best match with measured living skin reflectances. Parameter name is listed on the x-axis of each histogram.

the cadaver has left the surface of the skin. The histogram for the oxygenation percentage is concentrated on the extreme edges of the histogram. As discussed earlier, oxygenation of the hemoglobin is not a significant factor if there is very little blood in the skin. The algorithm used to determine the model parameters had a tendency to select an extreme value of oxygenation if there was not a significant amount of blood in the skin. The histogram for the dermal depth shows a range of thicknesses from less than 0.1cm to more than 0.5cm. This is due to the fact that skin samples were collected from various parts of the cadaver which had skin with various thicknesses. The histogram for collagen percentages was concentrated at the 15% end of the histogram. This is due to the fact that as age increases, the amount of collagen

in skin decreases. The histogram for subcutaneous reflection covers the full range of scale factors. This is because the skin samples were collected from various parts of the body which would have differing amounts of subcutaneous reflection.
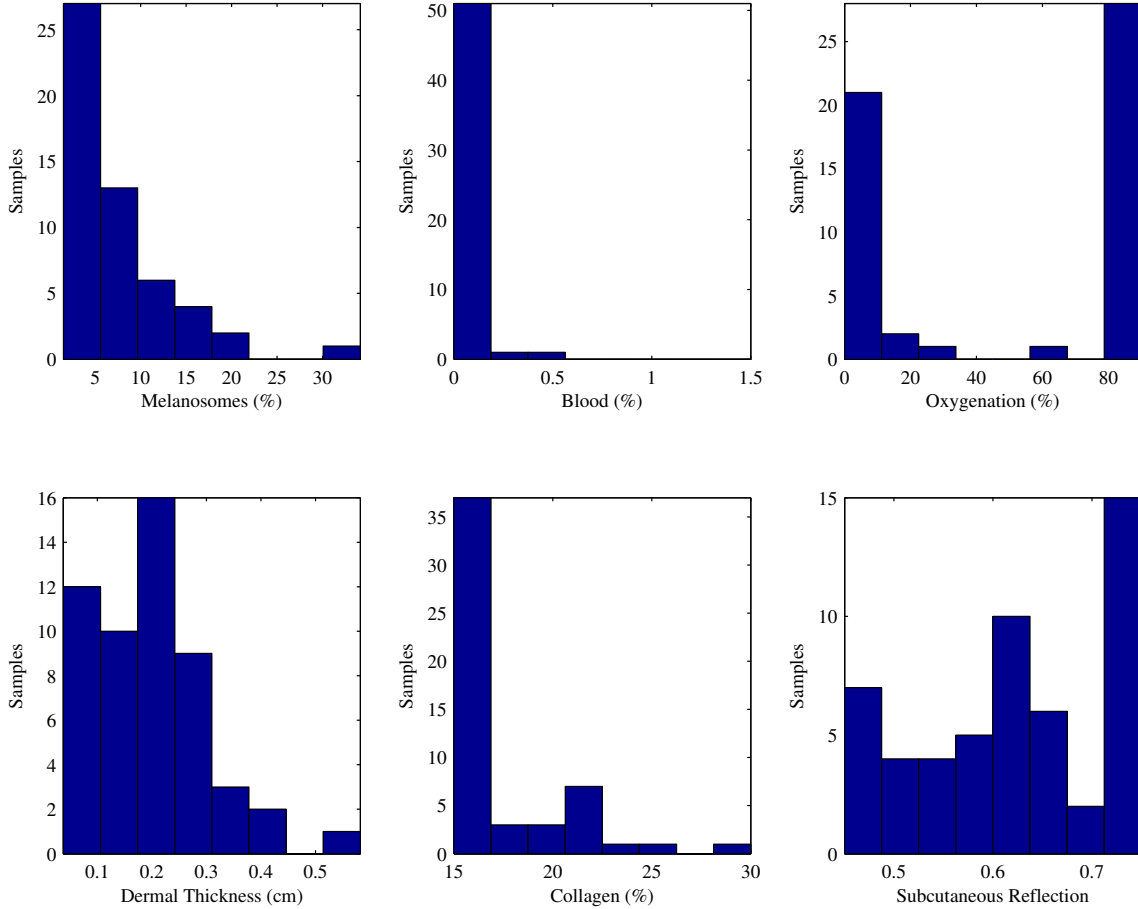
Figure 36: Histograms of the six model parameters used for the best match with measured cadaver skin reflectances. Parameter name is listed on the x-axis of each histogram.

2.8.2 Model sensitivity analysis. The Jacobian matrix (matrix of derivatives) is calculated to determine the sensitivity of the reflectance model as a function of the six model parameters. The Jacobian is a $M \times N$ matrix of partial derivatives based on a function with N inputs and M outputs. For this analysis, $M = 1351$ where each row represents a wavelength from 450nm through 1800nm in 1nm increments and $N = 6$ where each column represents a model parameter. The element of

the matrix at (m, n) is the partial derivative of the reflectance at the mth wavelength versus the nth parameter. The Jacobian is calculated for each of the 76 model results that best matched the 76 measured skin reflectances previously described. A relatively high partial derivative for a specific parameter at a specific wavelength means that the model is sensitive to the parameter at that wavelength. To characterize the sensitivity of the model, the mean of the Jacobian matrices was calculated for various categories. These categories include the 24 measurements from living subjects, 52 measurements from cadavers, 4 measurements from the four fairest living subjects, and 4 measurements from the four darkest living subjects. The resulting columns from each of the matrices was then plotted as shown in the rest of this section.

The first category analyzed is all of the model results for the living skin reflectances as shown in Fig. 37. The figure shows that the model is most sensitive in the VIS to the melanosome percentage. As the wavelength increases, the model becomes less sensitive to the melanosome percentage which corresponds to the fact that melanosome absorption decreases as wavelength increases. The model is also highly sensitive to the percentage of collagen in the dermis. This sensitivity is constant across the VIS and NIR. In fact, the model becomes more sensitive to the collagen percentage than the melanosome percentage in the NIR. The sensitivity of the model to subcutaneous reflection is approximately the same as the collagen percentage in the VIS. In the NIR, the model sensitivity to subcutaneous reflection drops. Next in sensitivity for the model is the dermal thickness. The sensitivity of the model to dermal thickness is constant across the VIS and most of the NIR accept for the water absorption bands around 1400nm and 1800nm. Around 550nm, the model is highly sensitive to the amount of blood in the dermis. As the wavelength increases, the model becomes less sensitive to blood volume. Finally, the model is only slightly sensitive to changes in the oxygenation versus other parameters. However, the very specific absorption features of oxygenated and deoxygenated hemoglobin make it a very important component in the model.
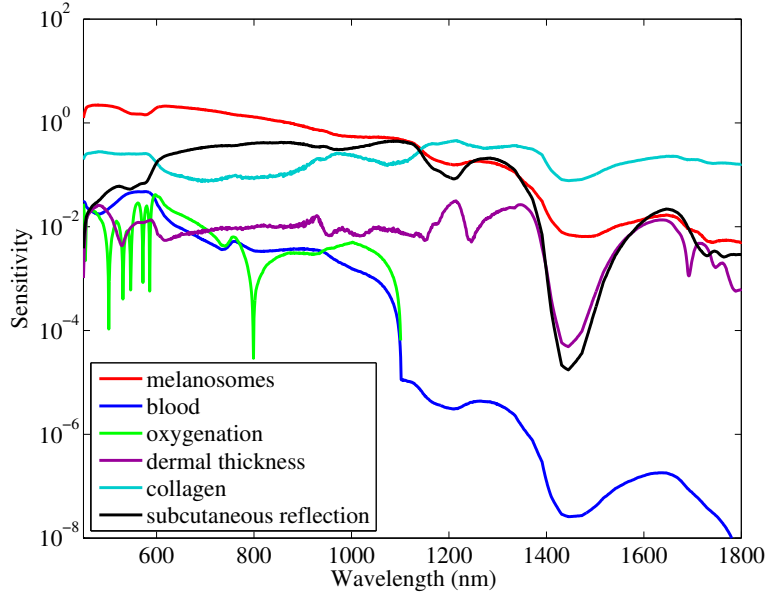
Figure 37: Sensitivity analysis for the skin model parameters for skin from living subjects over the VIS and NIR. Sensitivity is the partial derivative of the skin model function versus the specified model parameter at a particular wavelength. Skin model parameters include melanosome level, blood level, oxygenation level, dermal thickness, collagen level, and subcutaneous reflection level.

Figure 38 shows the sensitivity of the model when used for cadaver reflectances. For the cadavers, the model is more sensitive to the amount of blood and less sensitive to the oxygenation levels than for the living skin reflectances. This is because there is very little blood in the cadavers. This means a small increase in blood causes a large change in reflectance. Furthermore, a lack of blood in the cadavers means a change in the oxygenation of that blood will have little effect on the reflectance. The sensitivity of the model for the rest of the parameters is approximately the same for the living and cadaver skin reflectances.

Figures 39 and 40 show the sensitivity of the model using the four fairest living skin reflectances and the four darkest living skin reflectances respectively. Since the majority of the living skin reflectances were for fair-skinned persons, Fig. 37 and Fig. 39 are approximately the same. As shown in Fig 40, dark skin is less sensitive than fair skin to melanosome percentage and blood volume in the skin. For fair skin, a small change in the melanosome percentage makes a big difference in reflectance.

64
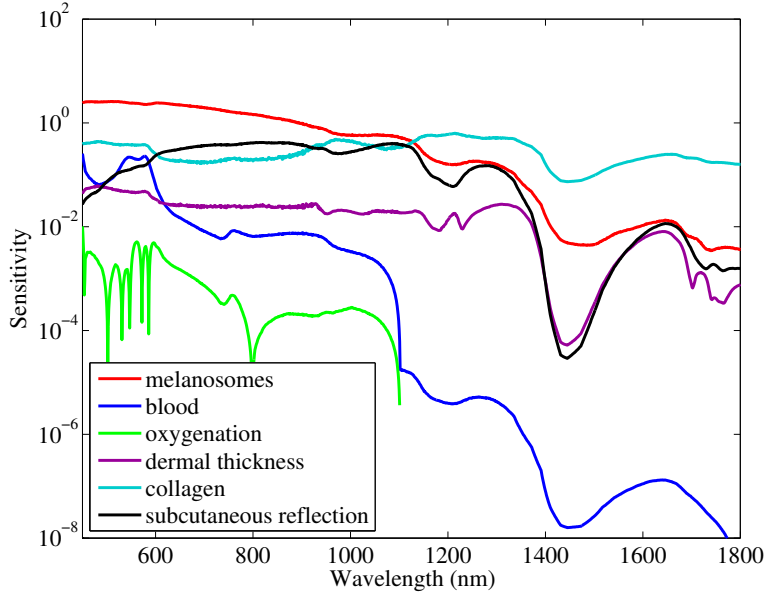
Figure 38: Sensitivity analysis for the skin model parameters for skin from cadavers over the VIS and NIR. Sensitivity is the partial derivative of the skin model function versus the specified model parameter at a particular wavelength. Skin model parameters include melanosome level, blood level, oxygenation level, dermal thickness, collagen level, and subcutaneous reflection level.

However, for dark skin, the same change in melanosome percentage does not create the same amount of change in reflectance. This means the model is less sensitive to melanosome percentage for dark skin. As discussed earlier, melanosomes in the epidermis block the effect of hemoglobin absorption in the dermis. This means, for dark skin, the model is less sensitive to blood volume and the oxygenation of the hemoglobin in that blood.

2.9 Discussion

In this chapter we described a model for the diffuse reflectance of human skin using the Kubelka-Munk equations where skin is modeled as a multi-layer material. Unlike other models which represent skin as multiple layers this model incorporates multiple reflectances between optical interfaces. This allows for the addition of layers to the model without a reduction in accuracy.
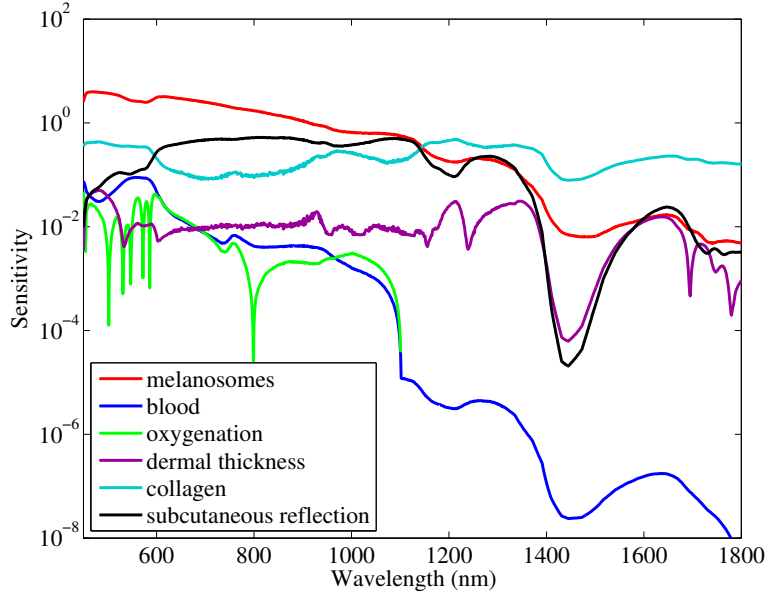
Figure 39: Sensitivity analysis for the skin model parameters for fair skin (Type I/II) from living subjects over the VIS and NIR. Sensitivity is the partial derivative of the skin model function versus the specified model parameter at a particular wavelength. Skin model parameters include melanosome level, blood level, oxygenation level, dermal thickness, collagen level, and subcutaneous reflection level.

Good results for the model require exact values for the absorption and scattering coefficients of the constituent materials of skin. The absorption and scattering coefficients of many of these materials are available in the current literature. However, due to limitations in the ability to isolate many of these materials without changing their optical properties, the accuracy of the measured absorption and scattering coefficients is limited. This is one possible source of error in the model.

One absorption coefficient measured specifically for this work was that of collagen. The absorption coefficient of collagen for the VIS and NIR was obtained from measurements of clear gelatin sheets (100% collagenous protein) using the ASD FieldSpec3® Spectrometer. Although the ASD FieldSpec3® Spectrometer provided accurate measurement of the absorption coefficient across the VIS and NIR, other types of equipment such as an integrating sphere used in conjunction with a spectrometer could provide even more accurate measurements. Better measurements of the collagen absorption coefficient would result in a more accurate skin reflectance model.

66
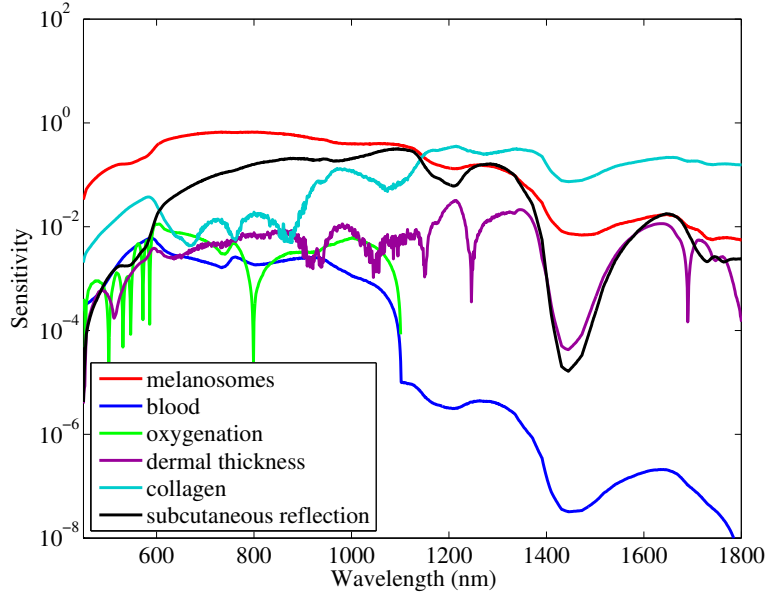
Figure 40: Sensitivity analysis for the skin model parameters for darkly pigmented skin (Type V/VI) from living subjects over the VIS and NIR. Sensitivity is the partial derivative of the skin model function versus the specified model parameter at a particular wavelength. Skin model parameters include melanosome level, blood level, oxygenation level, dermal thickness, collagen level, and subcutaneous reflection level.

The next element measured for the skin reflectance model was the scattering coefficient of skin tissue. This was based on reflectance measurements from living people and cadavers as well as skin samples collected from cadavers. For the purpose of this work, the scattering coefficient of the epidermis was modeled as the same for all types of skin. For the dermis, the scattering coefficient was modeled as a function of the collagen percentage in the dermis. In reality, there is likely a greater variation in the scattering coefficient for the skin of different people. This is another likely source of error in the model.

For completeness, the final element of the model is the reflectance of subcutaneous tissue. We collected multiple reflectances of subcutaneous tissue which we used to create a characteristic spectrum. The spectrum can be scaled to approximate a wide range of subcutaneous tissue spectra. Although this method did a reasonable job approximating the reflectance spectra of subcutaneous tissue, there are still large

67

enough differences in measured and modeled subcutaneous tissue to induce errors in the skin reflectance model.

Even with the possible sources of error in the model, all of the elements allow for a model that can accurately match a wide variety of skin reflectances. The mean RMSE between the model and the measured skin reflectances from living subjects and cadavers was only 2%.

An analysis of the model parameters which best fit the measured data shows a reasonable distribution of model parameters. The distribution of model parameters can be explained by the parameter boundaries (minimum and maximum possible values of the parameter based on the biology of skin) and by the types of skin measured. The distribution of the melanosome percentage correlates with the distribution of skin colors measured. For this research, there was a higher concentration of measurements for fair skin. The distribution of blood volumes varied widely for the living subjects while it was concentrated near zero for the cadavers. Blood in the skin of living subjects will vary because of different biological conditions. For cadavers, blood has the tendency to leave the skin. Oxygenation levels for living subjects was well within the ranges found in the literature while a lack of blood in the cadavers reduced the validity of the oxygenation levels estimated for cadavers. The dermal thickness for the living subjects was concentrated on the lower end of the dermal thickness distribution while the cadavers had a more uniform distribution. This can be explained by the fact that the skin measured on the living subjects came from the forearm which has a relatively thin dermal thickness. The measurements for the cadavers, however, came from multiple areas of the body with differing amounts of dermal thickness. The collagen percentage for the living subjects had a fairly uniform distribution while the collagen percentage for the cadavers was concentrated on the lower end. This corresponds with the fact that the cadavers were older people and a reduction in the amount of collagen in skin comes with age. Finally, the subcutaneous reflectance parameters for the living subjects and cadavers was almost uniformly distributed.

This can be accounted for by the fact that different subjects (living and cadaver) had different amounts of muscle and fat making up their subcutaneous tissue.

The sensitivity of the model output to changes in the parameters is also explainable based on the biology and optical properties of skin. Melanosome percentage was the most sensitive parameter in the VIS with subcutaneous reflectance and collagen percentage following in sensitivity. Blood volume, hemoglobin oxygenation, and dermal thickness were much less sensitive than the other parameters in the VIS. In the NIR, collagen percentage takes on a greater percentage while the sensitivity of melanosome percentage and subcutaneous reflectance drops. The sensitivity of the rest of the parameters either decreases or remains the same in the NIR. Even though the sensitivity of model parameters varies, all of the parameters are important in creating the most accurate model possible.

III. Application of Skin Reflectance Model for Determining Sensor Reaching Radiance for Imaging Human Skin

3.1 Introduction

Knowledge of the reflectance spectra of a material as well as the incident radiant light allows one to determine the expected sensor input. A relevant example of this would be a color camera recording the response of sunlight reflecting off human skin. The radiance of sunlight is well documented and easily measured with an ASD FieldSpec3® Spectrometer. The reflectance of human skin is also determined using the reflectance model developed in this dissertation where various parameters such as melanosome levels or hemoglobin levels can be adjusted. The reflectance of human skin can also be measured with an ASD FieldSpec3® Spectrometer. The former allows one to model specific conditions such as vasodilation and vasoconstriction which could be reactions to embarrassment or nervousness respectively. These and other conditions visibly manifest themselves within different portions of the spectra of skin. One may use model generated spectra to simulate any number of conditions as they relate to psycho-physiological responses. This gives one a way to understand what is detectable and what is not. The final aspect is the camera system response (optics and focal plane array). In this way, given what one knows one needs to detect, one may design the system with an appropriate response to perform the specified task. In the examples here, we use a typical red-green-blue (RGB) camera response, something well understood and well documented. A generic response of a color (i.e., RGB) sensor is also well documented. Based on these three pieces of knowledge, the expected output of the camera to an arbitrary light source on skin can be determined. A block diagram demonstrating this concept is shown in Fig. 41

To demonstrate this concept, the skin reflectance model is used to generate reflectance spectra for use on an avatar created in the RGB color space. The avatar is rendered with various parameters adjusted in the skin reflectance model including dermal blood levels and epidermal melanosome levels. Different illumination conditions are applied to the spectra which are then "imaged" by an RGB camera. However,
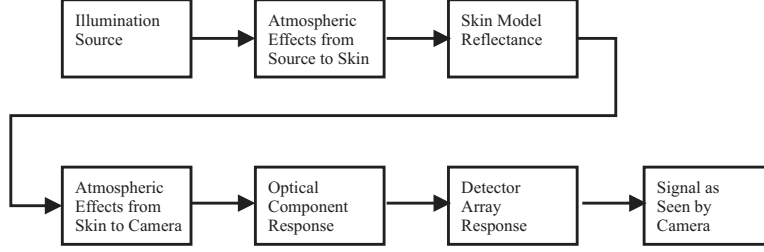
Figure 41: Block diagram of an imaging system used to model camera output when imaging skin.

since the skin model is a diffuse model and does not contain a specular component, we are limited to the case where the illumination source is normal to the skin.

3.1.1 Illumination sources. Total illumination can be a complicated assortment of multiple light sources and reflections of these light sources off of different materials. For simplicity, the two sources used on our avatar are an equal energy spectrum and a blackbody radiator. An equal energy spectrum is simply a light source with a flat spectral distribution. A blackbody radiator is an object at a given temperature T (in Kelvin) that emits a radiation spectrum defined by:

$$M(\lambda) = \frac{2\pi h c^2}{\lambda^5 \left(e^{\frac{hc}{\lambda k T}} - 1\right)} \tag{23}$$

where $h = 6.626 \times 10^{-34} Js$, $c = 3 \times 10^8 \frac{m}{s}$, $k = 1.38 \times 10^{-23} \frac{J}{K}$, and units of wavelength (λ) are in meters (m) [18]. Many common light sources can be approximated as blackbody radiators including sunlight ($T \approx 5250K$), moonlight or a "cool" incandescent light bulb($T \approx 4100K$), a "warm" incandescent light bulb ($T \approx 3200K$), and an open flame ($T \approx 1800K$) as shown in Fig.42. All of the light sources used to illuminate the avatar are scaled to have equal total power in the region of the spectrum between 380nm and 825nm. This allows an accurate comparison of the effect of the illumination source on the avatar without having to consider the illumination level. The light sources are also scaled so that the brightest possible skin pixel (based on the

71

skin reflectance model) does not saturate any of the channels in the RGB color space used to demonstrate the sensor response concept.
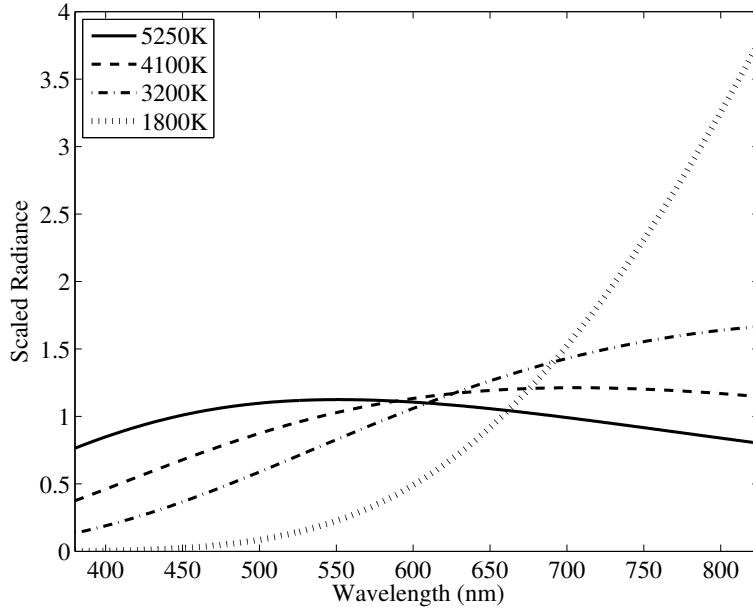
Figure 42: Scaled blackbody radiance curves for 5250K, 4100K, 3200K and 1800K. Curves are scaled so sum of area under curves between 380nm and 825nm are equal.

3.1.2 The RGB camera response. In order to color the avatar, spectra are generated from our physics-based model of skin reflectance and of blackbody curves of several lighting sources. The product of the two spectra are then converted to the RGB color space. Each pixel is parameterized based on the desired effect of that pixel. For example, one may determine RGB values transformed from the skin reflectance model based on different lighting conditions, blood volumes, hemoglobin oxygenation levels within blood, or epidermal melanosome levels.

For the cheek regions, it is assumed that melanosome levels and hemoglobin oxygenation levels are the same as the rest of the face. We wish to increase blood volume in the cheeks to give a rosy cheek effect. To simulate this affect, the method defined by Kalra and Magnenat-Thalmann is used [39]. First, an area of the cheek for the blush is defined with a Bezier curve. Next, a Gaussian distributed spatial gradient within this blush area is used to define the blood volume within the dermis.

The blood volume in the cheek varies between the highest volume in the center of the cheek and the value for the rest of the face. This is done to give a more realistic depiction of blood distribution in these regions.

Since the reflectance spectra tell us how much of the incident light energy is reflected from the skin surface, they are scaled using a matrix of intensity values. This matrix accounts for lighting effects in the environment and simulates the amount of energy incident on each of the skin pixels. These intensity values are based on a gray-scale version of the original image scaled so the maximum value is equal to one. In this way, shadows and facial features are preserved in the final avatar which is necessary since the model only accounts for the diffuse portion of skin reflectance.

Once the skin reflectance spectrum and the spectrum of the lighting source are known, the two spectra are multiplied together to form a reflected radiance spectrum, $s(\lambda)$. Creating realistic skin color involves a transformation of $s(\lambda)$ into the CIE color space (three dimensional color space defined by the channels X, Y, and Z) followed by a transformation into the RGB color space. This first conversion is done using Eqn. (24) where values for $x(\lambda)$, $y(\lambda)$, and $z(\lambda)$ are shown in Fig. 43 [32, 94] and enumerated in Appendix B.

$$
\begin{aligned}
X &= \int_0^\infty s(\lambda)x(\lambda)d\lambda \\
Y &= \int_0^\infty s(\lambda)y(\lambda)d\lambda \\
Z &= \int_0^\infty s(\lambda)z(\lambda)d\lambda
\end{aligned}
\tag{24}
$$

Once values of X, Y, and Z are determined, they are transformed into values of R, G, and B using [29]:
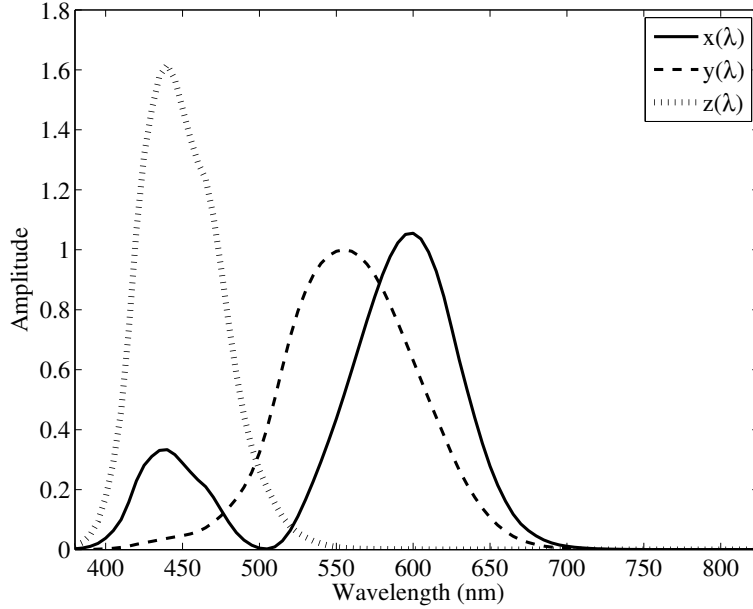
Figure 43:   Response curves as a function of wavelength for the Commission internationale de l'clairage (CIE) color space.

$$
\begin{bmatrix} R \\ G \\ B \end{bmatrix} = \begin{bmatrix} 0.4185 & -0.1587 & -0.0828 \\ -0.0912 & 0.2524 & 0.0157 \\ 0.0009 & -0.0025 & 0.1786 \end{bmatrix} \begin{bmatrix} X \\ Y \\ Z \end{bmatrix}. \tag{25}
$$

Although it would be possible to transform the hyperspectral data directly into the RGB colorspace rather than first transforming the data into the XYZ colorspace, transforming the data into the XYZ colorspace allows a user additional flexibility. The selection of the RGB colorspace in this work is for demonstration purposes, but this method is easily adapted for transformation of the XYZ colorspace to other commonly used three-dimensional colorspaces.

Model input parameters are easily changed to incorporate additional regions to the avatar for study (e.g. bruises, rashes, or freckles). Assumptions of uniform spatial distribution of melanosome level and blood oxygenation level parameters are for modeling simplicity only. Non-uniform spatial distributions of chromophores as

74

well as the adjustment of the volume of chromophores, such as bilirubin, and beta-carotene, can be used to increase the realism of the results.

The avatar used for this work is based on an image created by DAZ Productions, Incorporated [17]. This work does not generate spectra for the eyes, lips, hair, or the avatar's background environment; they retain the color of the original avatar image. Figure 44 shows a color image of an avatar based on the RGB colors calculated from a model generated spectrum assuming a 2% melanosome level with a baseline volume of blood throughout most of the face and three times the baseline level of blood in the cheeks illuminated from the front with an equal energy spectrum lighting source. The right frame of the figure shows the reflectance spectra used to derive the color of the face and cheeks. There is a noticeable decrease in reflectance in the portion of the cheek spectrum from 350nm to 600nm which is discussed below in Section 3.2.
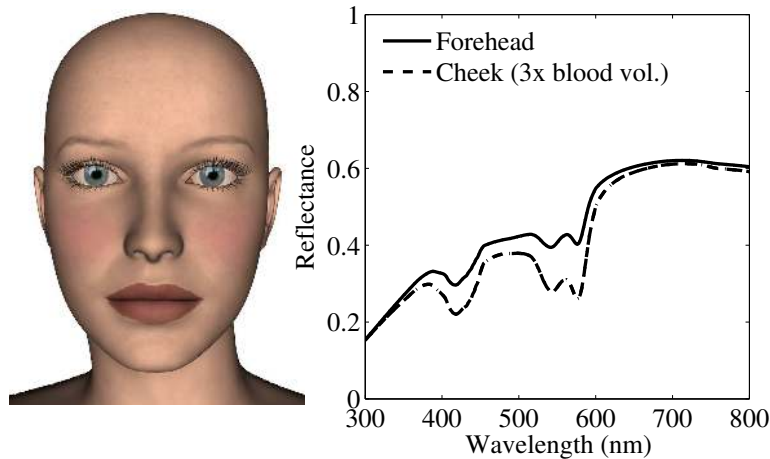
Figure 44: **Left**: Avatar with a 2% melanosome level and increased blood volume in the cheek. **Right**: Corresponding reflectance spectra.

3.2 Results

3.2.1 Epidermal melanosomes.   The melanin pigment is contained in cells throughout the epidermis called melanosomes. Melanosome volume varies from 1.6 – 6.3% for a fair-skinned person, 11 – 16% for a moderately pigmented person, and 18 – 43% for a darkly pigmented person [35] (see Table 1). As the melanosome level

increases, its effect on mean skin reflectance in the visible begins to decrease. This point is demonstrated in Fig. 45 where a plot of the mean skin reflectance averaged over 380-750nm is shown for melanosome levels ranging from 1%-43%.
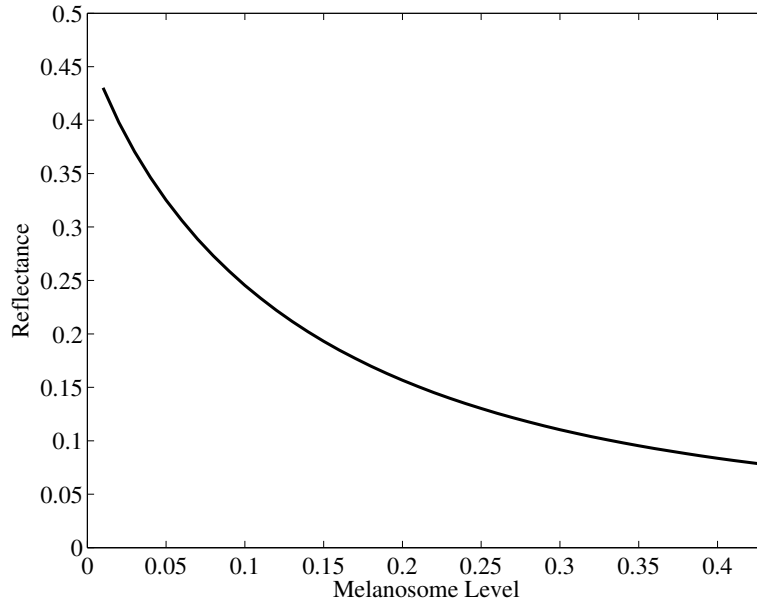
Figure 45:   Mean skin reflectance from 380nm-750nm for melanosome levels ranging from 1%-43%.

As stated previously, Fig. 44 (left) shows the avatar face with a 2% melanosome level with the corresponding spectra for the forehead and cheek (right). Due to the low melanosome level in this face, the blush of the cheeks is clearly visible. Figure 46 (top left) shows the results for 4% and 8% melanosome levels while Fig. 46 (bottom left) shows the results for a 16% and 32% melanosome level for the avatar. It is clearly evident that as melanosome level increases, the ability to differentiate the blush of the cheek from the rest of the skin diminishes. A more detailed description of the effect of hemoglobin on skin color is given in Sections 3.2.2 and 3.2.3. Figure 46 (right) shows the effect that increasing the melanosome level has on skin reflectance. As the melanosome level increases, reflectance decreases over the entire spectrum. This decrease is reduced for larger versus smaller wavelengths.
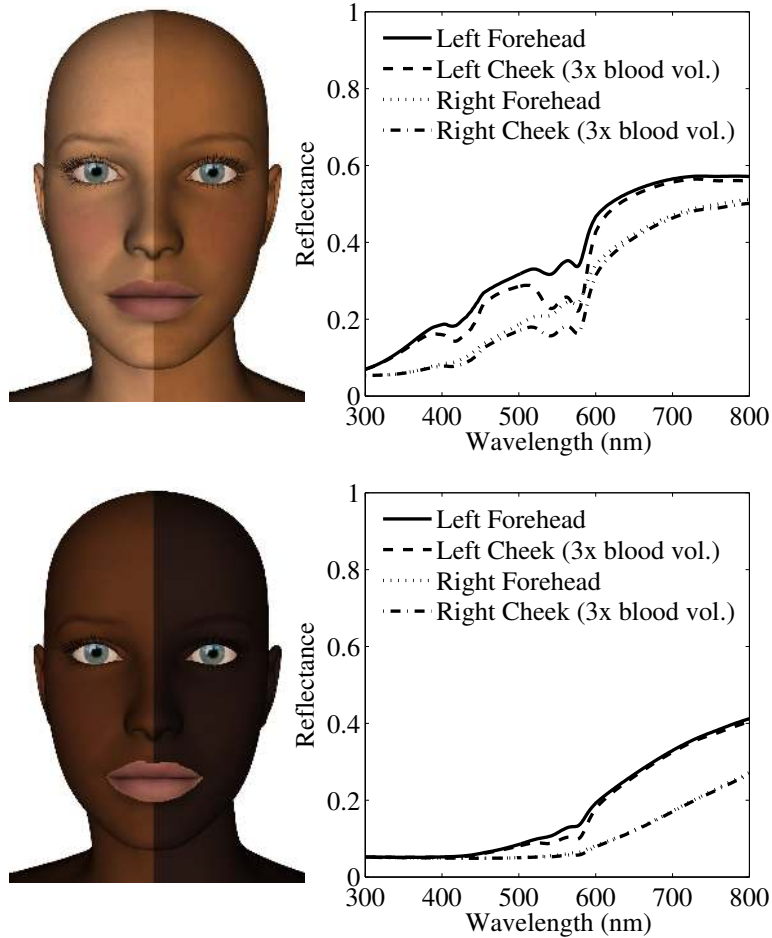
Figure 46:   **Top**: Left and right halves of avatar correspond to 4% and 8% melanosome levels respectively in the left frame with corresponding reflectance spectra in the right frame. **Bottom**: Left and right half of avatar correspond to 16% and 32% melanosome levels respectively in the left frame with corresponding reflectance spectra presented in the right frame.

3.2.2   Blood volume.   Dilation of the vascular system is due to the regulation of the nervous system and due to embarrassment or anger [75]. Nervous system regulatory mechanisms that cause vasodilatation in the skin are typically caused by the body's attempt to maintain and regulate temperature. This can occur if the skin temperature decreases below some acceptable value where the body is attempting to warm the skin to prevent damage and also occurs when the body attempts to cool the body down due to physical exertion.

The typical cases of vasodilation are evocable. That is to say, it is rather simple to force vasodilation as a response to cooling the body or heating extremities exposed to cold. What may be more interesting to model is vasodilatation as a response to embarrassment (due to a release of adrenaline). It most often appears in the face and upper thorax region (upper chest), although the particular manifestation depends on the individual. The centers of the cheeks for the avatars in Fig. 46 (left) show the effect of tripling the blood volume in the skin, simulating vasodilation [23, 75]. Figure 46 (left) shows the reflectance differences as a result of different blood volumes in the skin at different melanosome levels. As the blood volume increases in the skin, the characteristic ω-shape at 585nm caused by oxygenated hemoglobin within blood becomes more visible and the blue and green portions of the VIS are further suppressed. An increased melanosome level in the skin suppresses the effect of the chromophores of blood until their effect is negligible for a darkly pigmented person.

Trauma to the skin such as sunburn or an abrasion can result in increased blood volume near the surface of the skin. The left of the avatar in Fig. 47 (left) shows the result of increasing blood volume in the skin by a factor of 10 with a 2% melanosome level. At this blood volume, the skin begins to take on a distinctly reddish tint. The right frame of Fig. 47 shows the manifestation of increasing the blood volume on the reflectance spectra. The characteristic ω-shape of oxygenated hemoglobin and the suppression of the blue and green portions of the reflectance becomes even more significant as the blood volume increases.

Constriction of blood vessels is regulated by the nervous system and can be influenced by hormonal mechanisms [75]. Hormonal mechanisms are due to the release of epinephrine and small amounts of norepinephrine which can be a sympathetic nervous system response to physical exertions (e.g., exercise) [75]. One example of this would be fear evoking the "fight-or-flight" response causing vasoconstriction in the integumentary system to route blood to organs that need it.
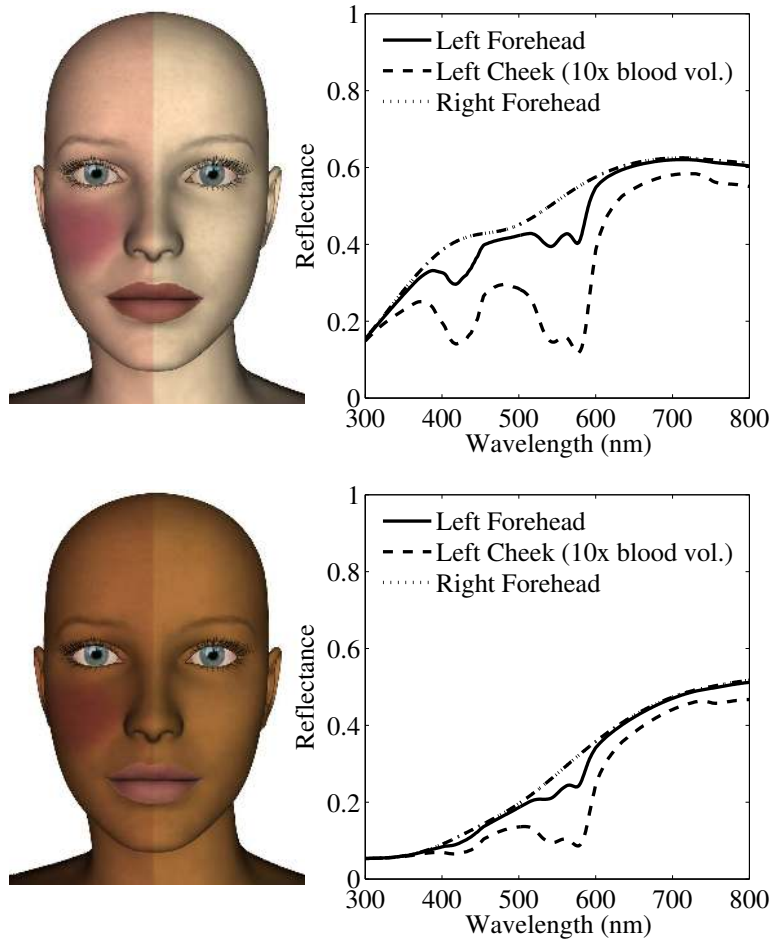
Figure 47: **Top**: Avatar with a 2% melanosome level. Left and right halves of avatar correspond to normal blood volume and no blood volume respectively in the left frame with corresponding reflectance spectra in the right frame. **Bottom**: Avatar with a 8% melanosome level. Left and right halves of avatar correspond to normal blood volume and no blood volume respectively in the left frame with corresponding reflectance spectra in the right frame.

Death can also cause the blood volume in skin to decrease. For example, gravity may cause blood to drain from the surface of the skin eliminating the pinkish hue caused by hemoglobin. The right halves of the avatars in Fig. 47 (top left and bottom left) demonstrate the absence of blood in the skin. Figure 47 (right) shows the skin reflectance for skin with normal and increased blood volume and no blood in the skin. Hemoglobin absorption in the blue and green portions of the VIS is no longer present which gives the right side of the face a paler look.

3.2.3 Hemoglobin oxygenation.   Another important aspect of this work is to characterize the color of skin based on the hemoglobin oxygenation level. This has important implications in search and rescue applications providing some level of triage.

Figure 48 shows the avatar with a 2% melanosome level. The left and right halves of the avatar in Fig. 48 (left) have a hemoglobin oxygenation level of 75% and 0% respectively while Fig. 48 (right) shows the associated reflectance spectra. The most obvious difference between the two sides of the avatar is in the cheeks which have ten times the normal blood volume. The cheek on the left side has a reddish tint while the cheek on the right side has the distinctly bluish tint associated with oxygen deprivation. As indicated previously in the spectra of Fig. 46, as the melanosome level increases, the ability to detect the presence of oxygenated and deoxygenated hemoglobin decreases. In fact, when medical professionals try to assess oxygenation levels of blood in a person, they usually place the device that measures oxygenation (pulse oximeter) on the tip of the finger since it does not contain melanosomes. Figure 48 (right) shows the skin reflectance spectra for skin with and without oxygenated hemoglobin. When hemoglobin in the blood is deoxygenated, skin has a lower reflectance in the red portion of the VIS and the ω-shape at 585nm is no longer present.

3.2.4 Illumination conditions.   To demonstrate the effect of different lighting conditions on the avatar, the face from Fig. 44 is illuminated with an equal energy spectrum on the left side while the right side is illuminated with a blackbody at a color temperature of 5250K (top), 4100K (middle), and 3200K (bottom). The 5250K color temperature approximates sunlight, while 4100K would approximate a "cool" incandescent light bulb and 3200K a "warm" incandescent light bulb. As the color temperature drops, the face begins to take on an orange hue. Note that "warm" light is associated with the lower color temperature which has a stronger red tint than the "cool" light with the higher color temperature [87]. It is the red tint that is

80
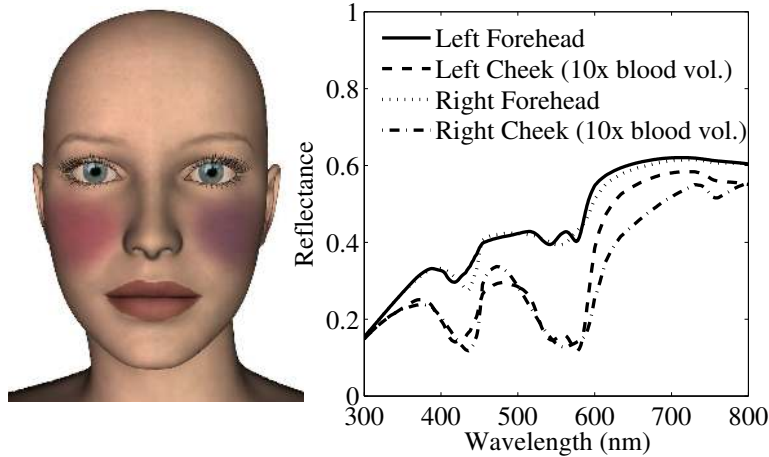
Figure 48: **Left**: Avatar with a 2% melanosome level. The left and right half of the avatar have a hemoglobin oxygenation level of 75% and 0% respectively. **Right**: Corresponding reflectance spectra.

associated by people with the "warmth" of the light and not the color temperature. Modeling the incandescent bulbs and sunlight as blackbody radiators provides a good approximation of their actual spectra. Color temperature is the metric used by many manufacturers to describe the spectra of their light bulbs.

3.3   Discussion

This chapter presents an avatar where the integumentary system is created using the engineering hyperspectral model developed in this dissertation. The model allows one to generate accurate colors for skin with varying epidermal melanosome levels, blood volume, and hemoglobin oxygenation levels. Secondarily, it hints that hyperspectral imagers may potentially be used to unobtrusively characterize persons of interest, say in a security or medical setting. In the latter case, conditions such as anemia (which causes reduced hemoglobin), jaundice (which causes increased bilirubin), or polycythemia (which causes increased hemoglobin) can be modeled and possibly measured remotely.

It further hints that given we understand illumination conditions, material spectrum, and sensor response, we can model sensor output. This provides us a method

for transforming sensor output into an estimated reflectance. This allows us to apply algorithms for remote sensing developed for use with reflectance, the topic of Chapter IV.
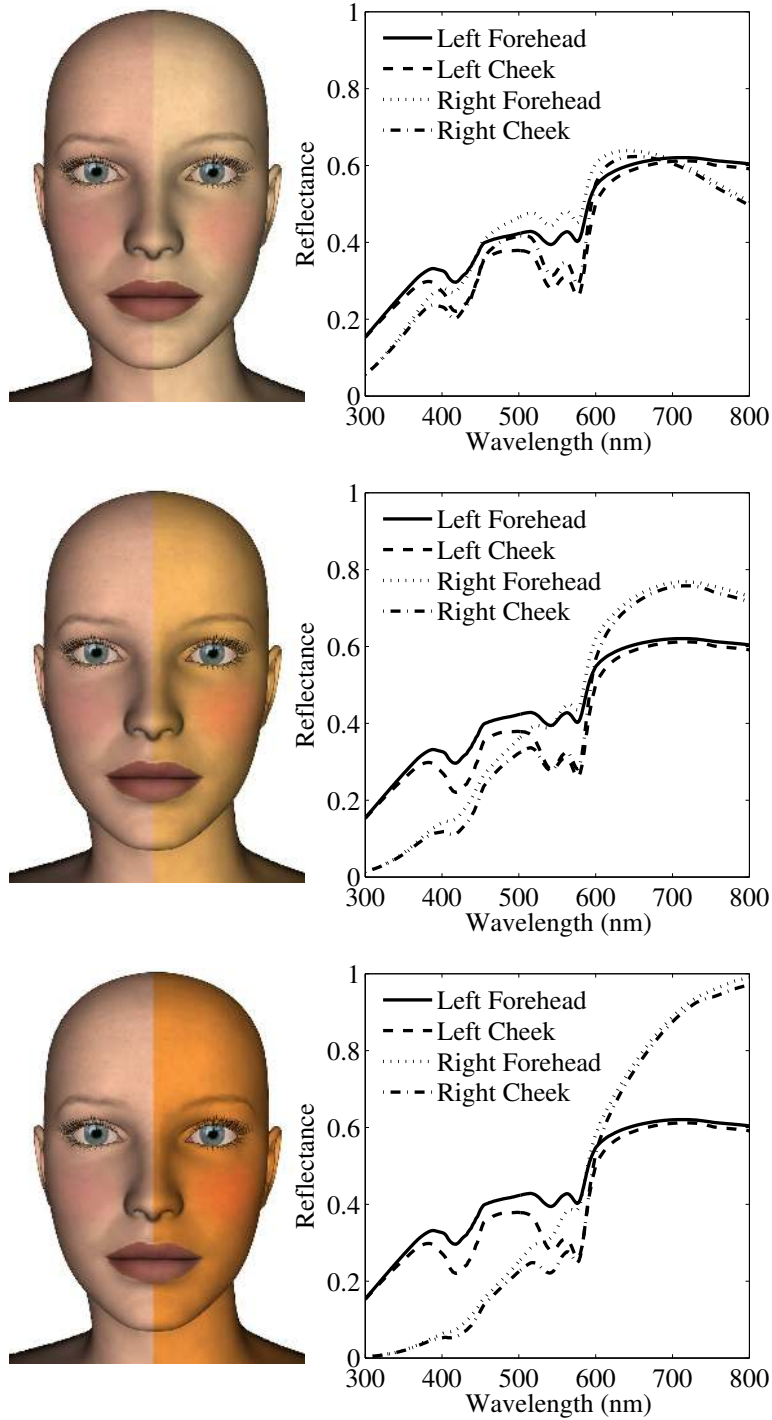
Figure 49:   Avatars with a 2% melanosome level and increased blood volume in the cheek. Left halves of the avatars are illuminated with an equal energy spectrum. The right halves are illuminated with blackbody radiation at different color temperatures. Corresponding reflectance radiance spectra presented in the right frame. **Top**: 5250K color temperature. **Middle**: 4100K color temperature. **Bottom**: 3200K color temperature.

IV. Application of Skin Reflectance Model for Remote Sensing

4.1 Introduction

A thorough understanding of the optical properties of skin in the visible (VIS) and near-infrared (NIR) allows one to accurately model skin's reflectance spectra. These optical properties include the indices of refraction of the air/skin interface, the absorption coefficient spectra of the constituent components of skin (water, collagen, melanin [24], hemoglobin [66], and others [59]) and skin's scattering coefficient spectra. An accurate model of skin reflectance allows one to identify spectral features for the detection and characterization of skin.

In Section 4.2, we identify features of skin reflectance that can be used to develop relevant exploitation algorithms. Section 4.3 presents our skin detection algorithm while Section 4.4 presents our skin pigmentation level estimation algorithms. Section 4.5 provides a description of the data used for our analysis. In Section 4.6 and Section 4.7, we present algorithm results for our skin detection and pigmentation level algorithms respectively. Concluding remarks are offered in Section 4.8.

4.2 Measured and Modeled Skin Reflectance and Skin Confuser Measurements

4.2.1 Observations from skin reflectance measurements. Reflectance measurements were collected from the forearms of 24 living subjects with various pigmentation levels and from several locations on 14 cadavers as described in Section 2.3. Reflectance measurements from three different living people with different pigmentation levels are presented in Fig. 50. Several important features can be noted in the spectra. As pigmentation level increases, there is a decrease in reflectance for skin throughout the VIS and NIR. However, since melanosome absorption decreases as wavelength increases, the difference in reflectance between skin with different amounts of melanosomes also decreases as wavelength increases [35]. Beyond 1300nm, melanosome absorption is no longer significant and skin reflectance is approximately

the same [5]. In the VIS, hemoglobin significantly affects the spectrum [43] accounting for the dip in reflectance around 570nm as well as the lower reflectance in the VIS up to 600nm. Water absorption becomes significant in the NIR where it accounts for the decrease in reflectance for wavelengths beyond 1150nm, the local maxima at 1080nm and 1250nm, and the local minima at 1200nm and 1400nm [5].
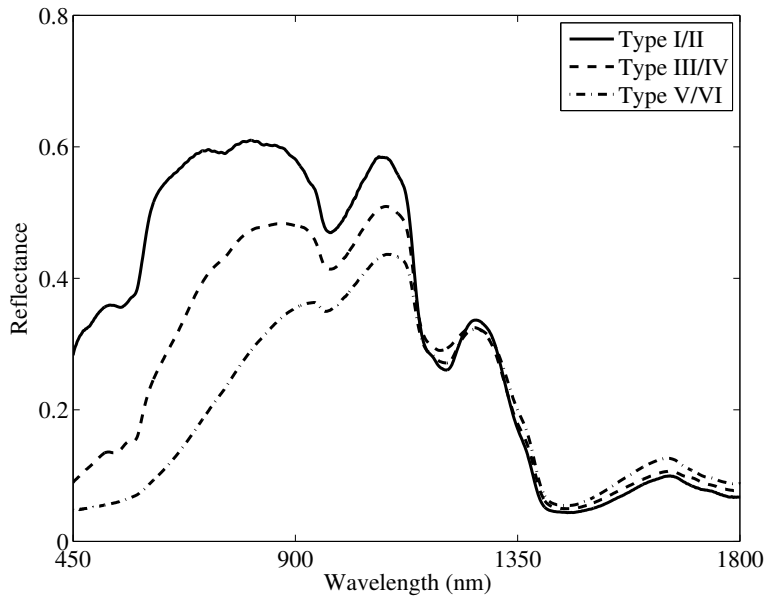
Figure 50:   Skin reflectance measurements of Type I/II skin (solid), Type III/IV skin (dashed), and Type V/VI skin (dashed-dotted).

4.2.2   Human skin reflectance model output.   Development of the skin detection and pigmentation level algorithms are based on the model developed in Chapter 2 rather than measured data. This is done because the model allows one to adjust various parameters, resulting in a wide variety of model generated estimated reflectance signatures. With the full-spectrum of skin samples available, to include the hard-to-come-by boundary conditions, we can determine theoretical bounds on the detector statistic (i.e., the features we use in the detector) allowing us to better set thresholds for our algorithm. Additionally, one can model other conditions of interest, including an increase in blood volume causing blushing (vasodilation) and a decrease in blood volume causing one to turn pale (vasoconstriction), as well as other abnormalities (anemia, etc.). Most importantly, correspondence between the model theory and the

85

anticipated imager response allows us to extend the results to an arbitrary imager and achieve good skin detection and pigmentation level estimation results. Figure 51 shows the modeled reflectance for skin from a healthy live person with a range of possible melanosome levels in the epidermis.
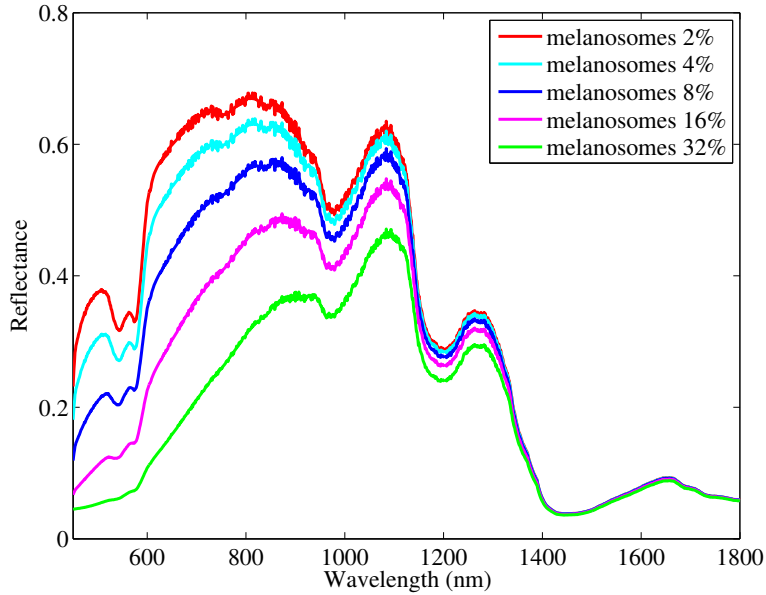
Figure 51:   Modeled skin reflectance for different melanosome levels.

Although the model is not described in detail in this chapter, we introduce limited model notation in order to aide discussion. Let measured skin reflectance be defined as $\rho(\lambda)$ and estimated reflectance of the ith pixel in a hyperspectral image be defined as $\hat{\rho}_i(\lambda)$. The modeled reflectance of skin for a specified level of pigmentation and blood volume is defined by the function $\tilde{\rho}(\lambda, D, H)$, where λ indicates the dependency on wavelength, D is the reflectance of skin at 685nm ($D = \rho(685\text{nm})$), and H the amount of blood in the dermis where "normal" blood volume is defined as $H = 1$, low blood volume by $0 < H < 1$, and excessive blood volume by $H > 1$. The selection of D ($\lambda = 685\text{nm}$) is based on work by Jablonski and Chaplin [33] who identify melanin as the dominating chromophore specifically at that wavelength, and use it in defining skin color for indigenous people from different regions of the world. For the purpose of this dissertation, D is synonymous with pigmentation level. The

parameters, λ, D, and H are used in developing the skin detection and pigmentation level estimation capability presented in Section 4.3 and Section 4.4.

4.2.3   Skin confuser measurements.   Understanding the reflectance of skin aides in developing methods to differentiate it from other materials. Several materials have colors similar to one of the wide varieties of skin-tones, some by design such as mannequins and dolls [6], others by coincidence such as brown cardboard, wood, leather, and some metals [1,38,84]. Depending on the image acquisition scenario, the scene background may also be rich in skin-tones such as a desert environment which contains naturally occurring materials with shades of brown, red, and yellow [95].

Measurements of different materials were collected with an ASD FieldSpec3® Spectrometer. A comparison of Type I/II skin with the reflectance of a plastic flesh-colored doll is shown in Fig. 52 (dashed and solid lines respectively). Like skin, the reflectance of the flesh-colored doll rapidly increases as wavelength increases in the VIS, hence the similar color. However, beyond 1200nm, the reflectance of the flesh-colored doll is significantly higher than skin since the surface of the doll does not contain water and thus does not exhibit skin's water absorption characteristics in the NIR. A comparison of the reflectance of Type III/IV skin with brown cardboard is also demonstrated in Fig. 52 (dotted line and dashed-dotted line respectively). Note that cardboard and Type III/IV skin exhibit an increase in reflectance as wavelength increases in the VIS. Again, in the NIR, the reflectance of cardboard remains relatively high while the reflectance of the skin is much lower due to water absorption. (Note that we further measured wet cardboard, and it does not exhibit the same absorption characteristics of skin.)

4.3   Skin detection algorithm

4.3.1   Features for skin detection and false alarm suppression.   Any detection algorithm is based on the quality of the received (reflected) signal (quality typically defined as signal to noise ratio), which depends on the illumination source. In this
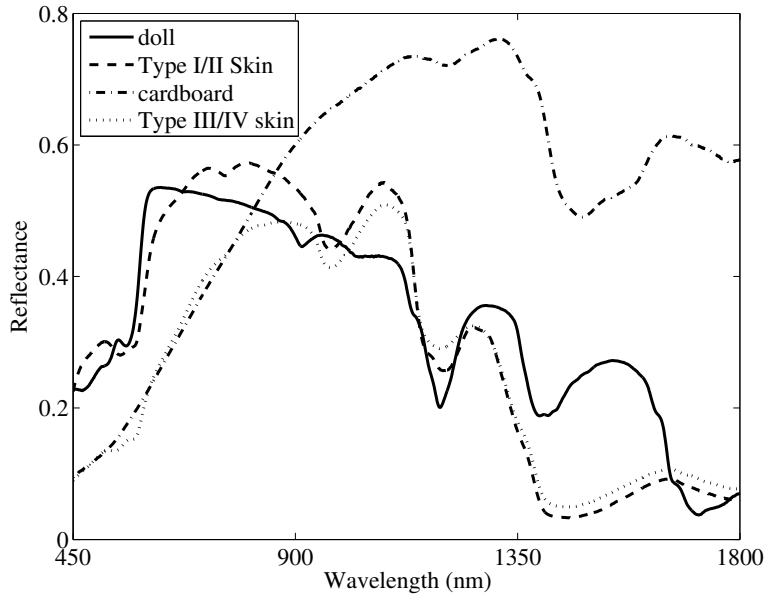
Figure 52:   Spectra of Type I/II and Type III/IV skin (dashed and dotted respectively) and spectra of a plastic doll and brown cardboard (solid and dashed-dotted respectively).

work, we are interested in detecting human skin under solar illumination. As an example, the ambient radiance on a sunny day in Dayton, Ohio (scaled so its maximum value is one) is demonstrated in Fig. 53 (solid line). The irradiance of sunlight received at the Earth's surface depends on several factors: presence of cloud cover, quantity and type of aerosols, humidity, and the solar angle (which dictates how much atmosphere the light must travel through), to name a few. Regardless, there are a few fundamental absorption features in the atmosphere in the NIR that should be avoided for any detection algorithm using hyperspectral data. These are primarily the bands associated with the absorption of water vapor nominally at 1400nm and 1900nm. The object of interest further imposes constraints on the spectra one should use in detection. As an example, a measurement of the radiance under solar illumination, scaled by the same factor as the solar irradiance, reflected from Type I/II skin is shown in Fig. 53 (dashed line). This solar illumination measurement was collected at approximately noon on a partly cloudy day with the ASD FieldSpec3® Spectrometer connected by a fiber optic cable to a cosine receptor. The local minima of the skin

88

reflectance measurement corresponds to water absorption at approximately 950nm, 1150nm, and 1400nm (note that we do not consider spectra beyond 1600nm since it is dominated by water absorbtion). As such, the location of the local minima and maxima in the NIR of the reflected radiance of skin corresponds to the locations of the local minima and maxima of skin reflectance.
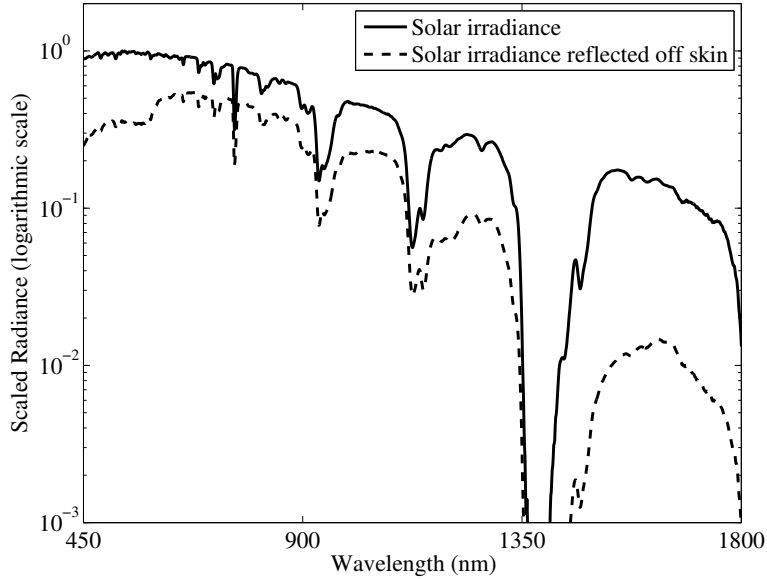
Figure 53: Solar irradiance in Dayton, OH on a sunny day scaled by the maximum irradiance (solid) and the radiance spectra of Type I/II skin illuminated by sunlight scaled by the same maximum irradiance (dashed).

Since these algorithms are based on skin reflectance, any imaged tissue needs to be converted from radiance to reflectance. This can be accomplished using one of several methods (we discuss two). The first is measuring the solar irradiance and dividing the corresponding spectra by these. The second method involves a simple linear regression using in-scene targets with known reflectance (the so-called Empirical Line Method (ELM) [21]). Estimated reflectance of pixel i ($\hat{\rho}_i(\lambda)$) is computed via ELM as shown in Eqn. (26) where $L_i(\lambda)$ is the apparent reaching radiance of pixel i, $\rho_1(\lambda)$ and $\rho_2(\lambda)$ are the measured reflectances of two reference materials in the scene and $L_1(\lambda)$ and $L_2(\lambda)$ are the apparent reaching radiances of the two reference materials respectively. The variable L_{m1} is the radiance of the first reference material and L_{m2}

89

the radiance of the second reference material. The variable ρ_{m1} is the reflectance of the first reference material and ρ_{m2} is the reflectance of the second reference material. The variable $\hat{\rho}_i$ is the estimated reflectance for the ith pixel [21]. For the case of the hyperspectral camera used in this research, the values of L_i, L_{m1}, and L_{m2} can also represent the raw values collected by the camera rather than an apparent reaching radiance. However, Eqn. (26) still holds.

$$\hat{\rho}_i = \frac{\left(L_i(\lambda) - \frac{L_{m1}(\lambda)\rho_{m2}(\lambda) - L_{m2}(\lambda)\rho_{m1}(\lambda)}{\rho_{m2}(\lambda) - \rho_{m1}(\lambda)}\right)(\rho_{m2}(\lambda) - \rho_{m1}(\lambda))}{L_{m2}(\lambda) - L_{m1}(\lambda)} \quad (26)$$

4.3.2 Normalized difference vegetation index (NDVI). By analyzing the properties of skin reflectance from our skin model and considering the atmospheric absorption characteristics relative to the model, we developed the *normalized difference skin index* (NDSI - note that this acronym also appears in the literature as the normalized difference snow index [73]) and the *normalized difference green-red index* (NDGRI). The former is for skin detection and the latter, as shown in Section 4.6, is adequate for false alarm suppression. Both equations are similar to, and motivated by, the Normalized Difference Vegetation Index (NDVI) [22] defined as:

$$\alpha_i = \frac{\hat{\rho}_i(860\text{nm}) - \hat{\rho}_i(660\text{nm})}{\hat{\rho}_i(860\text{nm}) + \hat{\rho}_i(660\text{nm})} \quad (27)$$

where α_i is the NDVI value for the ith pixel and as earlier, $\hat{\rho}_i$ is the estimated reflectance for the ith pixel, and $-1 \leq \alpha_i \leq 1$. From the model, assuming the model output is accurate and under the conditions that blood levels range from zero to $2\times$ "typical" volume and $1.5\% \leq$ melanin $\leq 43\%$, the NDVI for skin is $-0.00389 \leq \alpha_i \leq 0.50321$. Knowledge of the bounds of the NDVI metric is one tool that can be used in an accurate skin detection algorithm.

The NDVI looks for a large difference in the reflectance between approximately 660nm and 860nm as this is characteristic of vegetation (due to chlorophyll absorption in the red portion of the spectra and high scattering in the NIR). Our combined NDSI/NDGRI-based skin detector also considers the difference for their respective regions. As with the NDVI values for skin, the theoretical bounds on the NDSI and NDGRI for skin are determined using our skin reflectance model.

4.3.3 Normalized difference skin index (NDSI). The NDSI is a function of reflectance at 1080nm and 1580nm. The reflectance at 1080nm is the location of a local maximum of the reflectance of skin in the NIR where melanosome absorption dominates. Beyond 1080nm, water absorption in the skin becomes more significant until a local minimum at approximately 1400nm. A stable yet low-valued reflectance feature in skin spectra is chosen at 1580nm (beyond the atmospheric water vapor band at 1400nm), in order to ensure the derivative is large between melanin-dominated and water-dominated portions of the spectra. The model and measurements show that the difference in reflectance for all skin types is fairly large at 1080nm versus 1580nm, which is consistent with reflectance measurements in the literature and in this chapter. Furthermore, according to the measured (and known theoretical) solar irradiance curves in Fig. 53, a significant amount of solar illumination power reaches the surface of the earth ensuring a strong signal-to-noise ratio at 1580nm. The NDSI is described as:

$$\gamma_i = \frac{\hat{\rho}_i(1080\text{nm}) - \hat{\rho}_i(1580\text{nm})}{\hat{\rho}_i(1080\text{nm}) + \hat{\rho}_i(1580\text{nm})} \qquad (28)$$

where γ_i is the NDSI value for the ith pixel and $-1 \leq \gamma_i \leq 1$ for all materials. Under the same assumptions as stated above for the NDVI, NDSI values cover the range $0.65703 \leq \gamma_i \leq 0.76779$ for skin pixels.

4.3.4 Normalized difference red-green index (NDGRI). The colors green and red encompass wavelength ranges of 495nm through 570nm and 620nm through 750nm respectively [28]. One can observe that human skin is more red than green, as indicated by Fig. 54, which shows the extremes of skin based on melanosome content. To eliminate common false alarm sources, such as heavy water bearing vegetation (succulents) and water-bearing objects that are highly forward scattering (e.g., snow and murky water), we invert the red-green relationship using the NDGRI. The bands are chosen to correspond to the red-green channels in the red-green-blue color space and are 660nm and 540nm respectively. The NDGRI is described as:

$$\beta_i = \frac{\hat{\rho}_i(540\text{nm}) - \hat{\rho}_i(660\text{nm})}{\hat{\rho}_i(540\text{nm}) + \hat{\rho}_i(660\text{nm})} \tag{29}$$

where β_i is the NDGRI value for the ith pixel and $-1 \leq \beta_i \leq 1$. Under the same assumptions as stated above for the NDVI, NDGRI values cover the range $-0.54079 \leq \beta_i \leq -0.06153$ for skin pixels.

4.3.5 Observation of feature values using modeled and measured data. Table 11 provides a list of NDSI, NDGRI, and NDVI values for different materials including skin with different pigmentation levels, skin confusers, and typical background material in a rural scene. As one would anticipate, materials with significant water content, such as vegetation and skin, have the highest NDSI values. Also note that the NDSI values for the darkest skin *can* be higher than values for vegetation. Vegetation has the highest NDVI values and objects that are green have the highest NDGRI values. Several examples of modeled skin reflectance for various levels of skin pigmentation (including the extremes), and the relevant wavelengths used for the NDSI, NDVI, and NDGRI algorithms are provided in Fig. 54.

From Table 11, it is clear that either the NDVI or NDGRI can be used to suppress false alarms when used in conjunction with the NDSI to identify skin. If
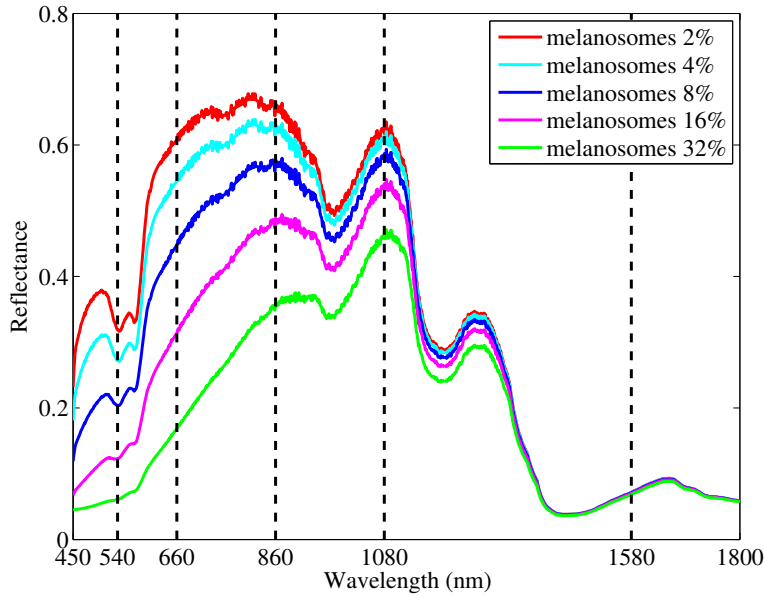
Figure 54: Modeled skin reflectance for different melanosome levels marked with colored solid lines. Pertinent spectral components used for each algorithm are marked with vertical dashed lines: (660,860)nm for NDVI, (1080,1580)nm for NDSI, and (540,660)nm for NDGRI.

one is searching for fair to moderately-pigmented persons in a scene with a significant amount of vegetation, the NDVI algorithm can be an effective method for filtering out water-rich vegetation. However, darkly pigmented people have a high NDVI value and may be incorrectly discarded by an NDVI threshold set too low. If one is searching for people in an urban environment, the NDGRI can filter out pixels that are more green than red in a scene. However, the NDGRI would have greater difficulty identifying vegetation under low signal-to-noise ratio conditions. This is due to the fact that NDVI>NDGRI for vegetation. We explore the use of NDVI and NDGRI in suppression of false alarms when combined with the NDSI for skin detection in the following sections. Specifically, we present a rules-based detection scheme and demonstrate the differences in false alarm suppression using both the NDVI and NDGRI.

4.3.6   Rules-based skin detection algorithms.   To identify a pixel as skin is a two step process. The first step is for the pixel to cross the NDSI threshold.

Table 11:   NDVI, NDSI, and NDGRI values for different materials.

Material	NDVI	NDSI	NDGRI
Fair Skin	0.04	0.77	-0.25
Darkly Pigmented Skin	0.51	0.66	-0.34
Grass	0.88	0.53	0.37
Leaf	0.9	0.27	0.41
Doll	0.04	0.24	-0.28
Paper Bag	0.27	0.15	-0.27
Cardboard	0.3	0.14	-0.33
Red Brick	-0.01	-0.01	-0.47
Soil	0.37	-0.1	-0.18

This means there is sufficient difference between the estimated reflectance of the pixel at 1080nm and 1580nm. The next step is to use either the NDVI or NDGRI to eliminate potential skin confusers. A rules-based skin detector based on NDVI and NDSI is defined as:

$$S_i = \begin{cases} 1 & \text{if } a_1 \leq \alpha_i \leq a_2 \text{ and } c_1 \leq \gamma_i \leq c_2 \\ 0 & \text{otherwise} \end{cases} \tag{30}$$

where $S_i = 1$ when the ith pixel is skin and $S_i = 0$ otherwise. Here, a_1 and a_2 are the minimum and maximum NDVI thresholds for skin respectively and c_1 and c_2 are the minimum and maximum values NDSI thresholds for skin respectively. Similarly, a rules-based skin detection based on NDGRI and NDSI is defined as:

$$S_i = \begin{cases} 1 & \text{if } b_1 \leq \beta_i \leq b_2 \text{ and } c_1 \leq \gamma_i \leq c_2 \\ 0 & \text{otherwise} \end{cases} \tag{31}$$

where b_1 and b_2 are the minimum and maximum NDGRI thresholds for skin respectively.

4.4 *Estimating reflectance of skin at 685nm as well as the melanosome content of the epidermis*

Estimating melanin level of those pixels detected as skin is based on several key skin reflectance features. As seen in Fig. 55, when melanin level increases, the reflectance in the region between 650nm and 950nm decreases and the reflectance at 1080nm does not undergo a significant change. The near-infrared melanosome index (NIMI) shown in Eqn. (32) takes advantage of this relationship providing a mechanism to classify skin as one of the Fitzpatrick skin types. As the melanosome level increases, $N(\lambda)$ decreases for values of λ between 650nm and 950nm where $N(\lambda)$ is used to estimate the reflectance of skin at 685nm. The reason for the selection of 685nm is discussed in Section 4.2.2. Although the reflectance of skin at 685nm can be read directly from a reflectance measurement, there are circumstances where this might not be possible. One example of this is only having reflectance spectra measurements in the NIR. Another example is having a reflectance value derived from a hyperspectral image that has the incorrect scale due to the method used to estimate reflectance. For both cases, the reflectance spectra can still be used to estimate the reflectance of skin at 685nm as will be shown in the rest of this section.

$$N(\lambda) = \frac{\rho(\lambda)}{\rho(1080\text{nm})} \tag{32}$$

NIMI values for the model, $\tilde{N}(\lambda, D)$, are based on the skin reflectance model using Eqn. (33) for each wavelength between 650nm and 950nm over the full range of melanin levels, D. The reason this range of λ values is analyzed is the flexibility it offers. Different types of sensors will have different capabilities to collect at this range of wavelengths. The value of λ to select for the NIMI algorithm is the lowest
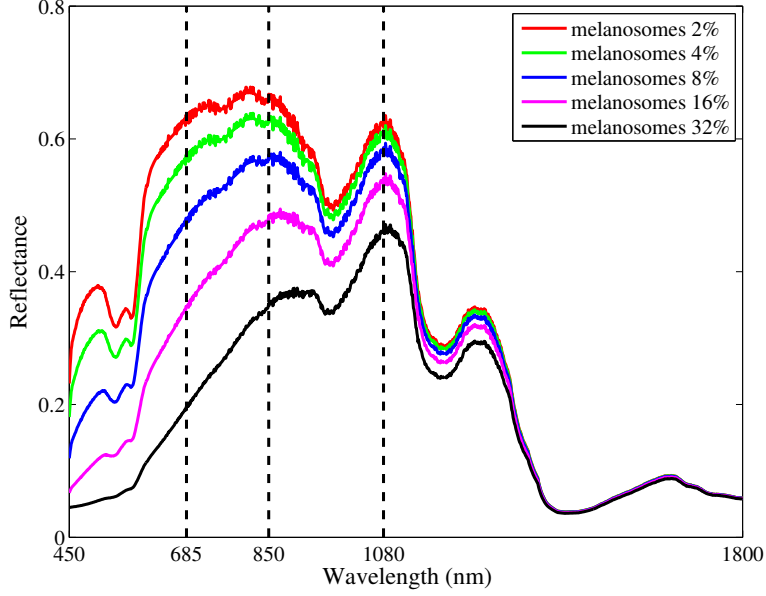
Figure 55:   Modeled skin reflectance for different pigmentation levels with locations of NIMI algorithm wavelengths identified with vertical dashed lines at 685nm, 850nm, and 1080nm.

wavelength between 650nm and 950nm and depends on the sensor response. Figure 56 shows D versus $\tilde{N}(\lambda, D)$ for different values of λ. The trend is to have a greater dynamic range of $\tilde{N}(\lambda, D)$ values for shorter wavelengths.

$$\tilde{N}(\lambda, D) = \frac{\tilde{\rho}(\lambda, D, 1)}{\tilde{\rho}(1080\text{nm}, D, 1)} \tag{33}$$

Once the NIMI values have been calculated for a specific wavelength λ, they can be transformed into an approximate value of D. This is done by performing a linear regression of a second order polynomial where an estimate of D is a function of $\tilde{N}(\lambda, D)$. Equation (34) shows the polynomial where coefficients were generated for each wavelength, λ, between 650nm and 950nm. Figure 57 shows a graph of the coefficients.
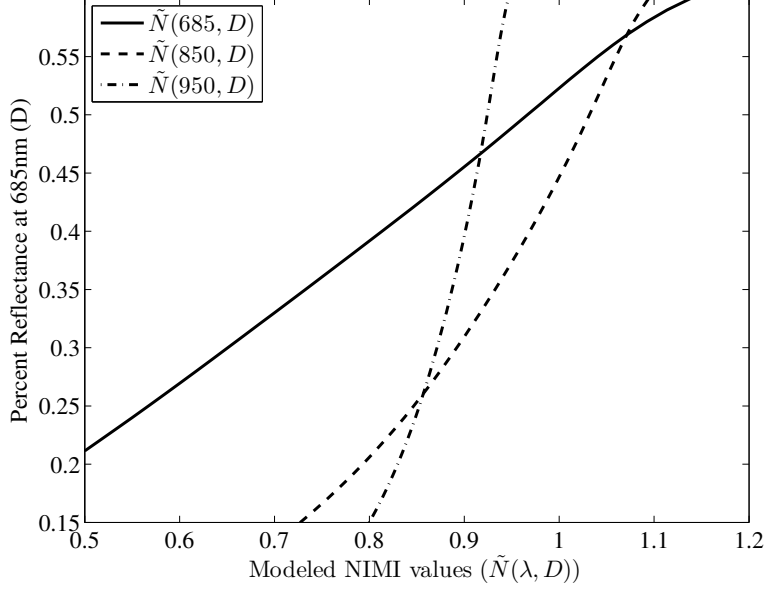
Figure 56: $\tilde{N}(\lambda, D)$ values for values of $\lambda = \{685, 850, 950\}$nm versus skin reflectance at 685nm (D).

$$D \approx S(\lambda)\tilde{N}(\lambda, D)^2 + M(\lambda)\tilde{N}(\lambda, D) + B(\lambda) \tag{34}$$

Although the coefficients were created from values generated by the model, Eqn. (35) is the estimate of skin reflectance at 685nm (D) based on the value of $\hat{N}_i(\lambda)$ which is derived from the estimated reflectance of the ith pixel, $\hat{\rho}_i(\lambda)$, as shown in Eqn. (36). The assumption is made that the modeled reflectance and estimated reflectance from the hyperspectral image are similar enough that the coefficients derived from the modeled data can be used with $\hat{N}_i(\lambda)$ to calculate D for the image skin pixels.

$$D \approx S(\lambda)\hat{N}_i(\lambda)^2 + M(\lambda)\hat{N}_i(\lambda) + B(\lambda) \tag{35}$$
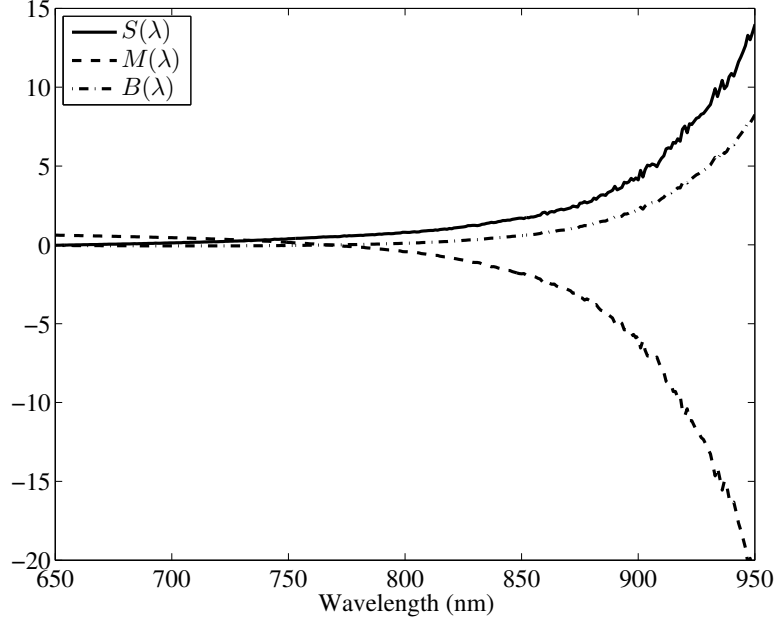
Figure 57: Regression coefficients for the NIMI algorithm for wavelengths between 650nm and 950nm.

$$\hat{N}_i(\lambda) = \frac{\hat{\rho}_i(\lambda)}{\hat{\rho}_i(1080\text{nm})} \tag{36}$$

The values of D for $\lambda = 685\text{nm}$ and $\lambda = 850\text{nm}$ can be calculated from Eqn. (37) and Eqn. (38) respectively where the coefficient values come from the linear regression of the modeled NIMI values. The results of the regression of D versus $\tilde{N}(\lambda, D)$ for $\lambda = 685\text{nm}$ and $\lambda = 850\text{nm}$ are shown in Fig. 58. This figure plots D versus $N(\lambda)$ for $\lambda = 685\text{nm}$ (squares) and $\lambda = 850\text{nm}$ (filled circles) for reflectance measurements collected from the forearms of living people.

$$D = 0.071314 \ N(685)^2 + 0.50862 \ N(685) - 0.060247 \tag{37}$$

$$D = 1.692\ N(850)^2 - 1.8351\ N(850) + 0.5906 \qquad (38)$$
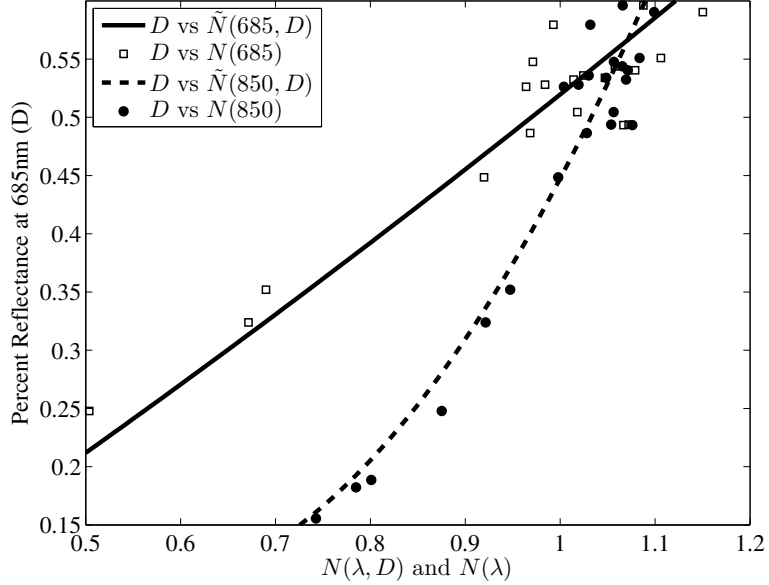
Figure 58: Regressed $N(\lambda)$ values for $\lambda = 685$nm (solid, square) and $\lambda = 850$nm (dashed, circle) versus D (skin reflectance at 685nm).

When estimating D from the estimated reflectance of skin pixels from a hyperspectral image, Eqn. (37) and Eqn. (38) can be used with $\hat{N}_i(\lambda)$ instead of $N(\lambda)$. The coefficients for these two equations will be used to estimate D for the hyperspectral test image described in the next section.

Based on the skin reflectance model, a linear regression is performed where melanosome percentage is a function of the variable D. Equation (39) shows the results of the linear regression of the fifth order polynomial where M is the melanosome percentage assuming a 60μm thick epidermis.

$$M = -35.649D^5 + 74.283D^4 - 62.223D^3 + 27.263D^2 - 7.0446D + 0.99453 \qquad (39)$$

4.5   Hyperspectral test images

Data used to test the skin detection and melanosome estimation algorithms was collected with the SpecTIR HST3 Hyperspectral Imager [36]. The HST3 collects data in the range of 400nm – 2500nm. The spectral bands are nominally 10nm wide in the VIS and 7nm wide in the NIR. The full width half maximum (FWHM) of each of the bands is approximately 8nm and 12nm respectively. Radiance spectra from the image cube is transformed into estimated reflectance using ELM described previously.

To test the rules-based skin detection algorithm, an image was collected with skin color confusers and skin with various levels of pigmentation as shown in Fig. 59 (top). The image contains a flesh-colored doll, a piece of cardboard, and a red brick. These objects were selected because of false detections they caused in skin detection algorithms based on color imagery. Other color confuser's include a leather boot and several pieces of wood. These objects were selected because their color was similar to some shades of skin. A branch from a conifer (from the yew family) is included in the scene as it is known to have a high NDSI value. The scene is a suburban environment with houses, streets, sidewalks, trees, typical residential yards with grass, bushes, bark, and other assorted materials. Portions of the reference panels used to perform the ELM are shown in the bottom right portion of the figure. Figure 59 (bottom) shows the corresponding pixels manually identified as skin.

Due to the noise inherent in the system/environment and the fact that the bands identified for our algorithms do not line up with the HST3 band centers, the NDVI, NDSI, and NDGRI algorithms were modified to accommodate the available spectra. The algorithms were implemented with the mean of the estimated reflectance of the three HST3 bands closest to the algorithms' band centers. For example, the estimated reflectance at 540nm used for the NDGRI algorithm was implemented using the mean of the estimated reflectance from the HST3 bands centered at 531.373nm, 542.741nm, and 554.075nm. The band centers for the HST3 estimated reflectance

Figure 59: **Top**: Color image of suburban test scene. The scene contains people with different skin colors as well as several potential false alarm sources. **Bottom**: The skin truth pixels.

that correspond to the band centers of the skin detection and melanosome estimation algorithms described earlier are provided in Table 12.

4.6   Results of the rules-based skin detector

The essential property of the NDSI algorithm is that skin is one of the few materials with a high reflectance at 1080nm and a low reflectance at 1580nm. Figure 60 (top) shows the estimated reflectance of the scene with confusers at 1080nm while Figure 60 (bottom) shows the estimated reflectance at 1580nm. Most of the materials in the image have a similar reflectance at both wavelengths. The two major exceptions to this are skin throughout the image and the bush at the bottom center of the

Table 12:   HST3 image bands used to implement skin detection and melanosome estimation algorithms.

Wavelength	Band 1	Band 2	Band 3
540nm	531.373nm	542.741nm	554.075nm
660nm	648.676nm	660.268nm	672.004nm
685nm	743.138nm	754.703nm	766.490nm
850nm	837.50nm	849.047nm	860.889nm
860nm	849.047nm	860.889nm	872.767nm
1080nm	1069.910nm	1078.060nm	1086.290nm
1580nm	1570.830nm	1579.030nm	1587.270nm

image. For both materials, the reflectance is much greater at 1080nm than 1580nm due to the fact that both materials contain significant amounts of water which is highly absorbing at 1580nm.

Application of the NDSI algorithm on the test scene from Fig. 59 (top) is shown in Fig. 61. The portions of the image with the highest NDSI values are skin and the bush at the bottom center of the image. The cloth at the bottom center of the image has a moderately high NDSI value. The rest of the image has very low or negative NDSI values. This includes the flesh-colored objects such as the doll, leather boot, cardboard, and wood at the bottom right of the image.

A receiver operating characteristic (ROC) curve for the NDSI-only detector is shown in Fig. 62, and was generated by adjusting $0 \leq \gamma \leq 1$. Two operating points are selected for comparison: first is a $P_D = 0.95$, second is a $P_{FA} = 0.0005$. A threshold of $\gamma = 0.314$ gives a $P_D = 0.95$ with a $P_{FA} = 0.0156$. The corresponding detection image for $\gamma = 0.314$ is shown in Fig. 63 (top). The algorithm does an excellent job of detecting skin of all colors, but has difficulty with skin under the chin of the person in the center of the due to the low illumination levels at that location. The algorithm also has difficulty with false detections of the bush and the strongly illuminated clothing at the bottom center of the image. A threshold of $\gamma = 0.589$ gives a $P_{FA} = 0.0005$ with a $P_D = 0.413$. The corresponding detection image for

Figure 60:   Suburban test scene with potential false alarm sources. **Top**: Image at 1080nm and **Bottom**: Image at 1580nm (bottom).

$\gamma = 0.589$ is shown Fig. 63 (bottom). The false detections from the bush and the clothing have been eliminated, however, the P_D for this threshold is poor.

To reduce false alarms caused by vegetation, the NDVI can be used to eliminate pixels detected as skin that also have a high NDVI value. Application of the NDVI algorithm to the test scene is demonstrated in Fig. 64. The Fitzpatrick Skin Types II, III, and IV skin pixels have NDVI values $\beta \leq 0.3$ while Types V and VI have NDSI values as high as $\beta = 0.55$. This limits the ability of the NDVI algorithm for use in skin detection algorithms when searching for darkly pigmented skin.

Three ROC curves shown in Fig. 65 are generated by adjusting the NDSI threshold γ while holding the NDVI constant at one of three values: $\alpha = \{0.5, 0.6, 0.7\}$ (solid, dashed, dashed-dotted respectively). An NDVI threshold of $\beta = 0.5$ results in
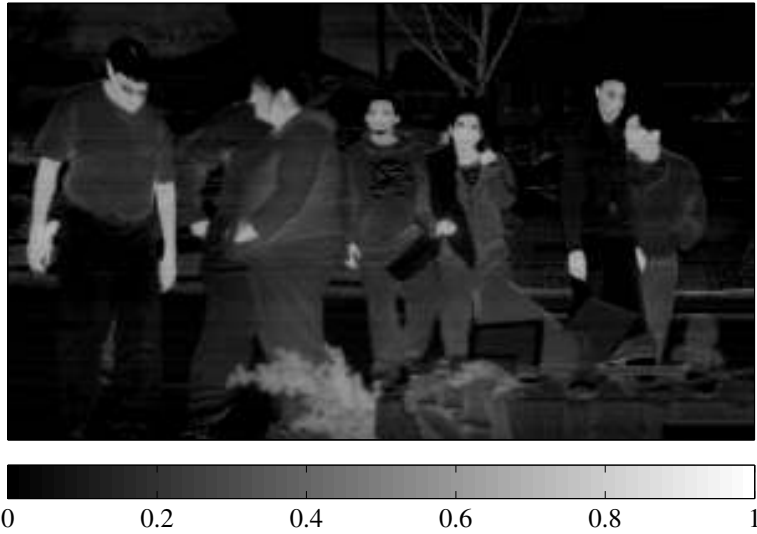
Figure 61:   Application of the NDSI algorithm to the suburban test scene with potential false alarm sources.
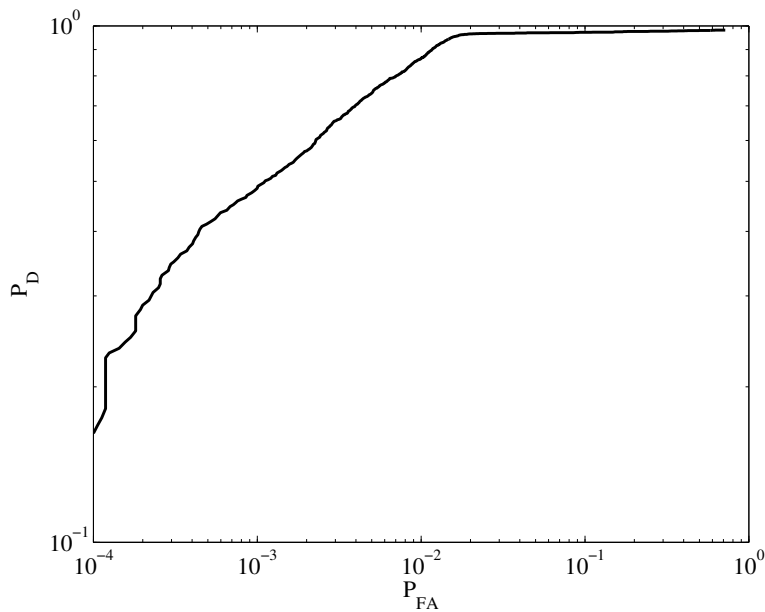
Figure 62:   The receiver operating characteristic (ROC) curve for skin detection varying NDSI threshold $0 < \gamma < 1$.

a maximum $P_D \approx 0.9$. This is due to the misidentification of skin pixels with a high level of pigmentation (Type V/VI skin) as vegetation. Increasing the NDSI threshold to $\beta = 0.7$ increases the maximum $P_D \approx 0.96$. However, P_D performance suffers for $P_{FA} < 0.0007$. An NDVI of $\alpha = 0.6$ has approximately the same maximum P_D
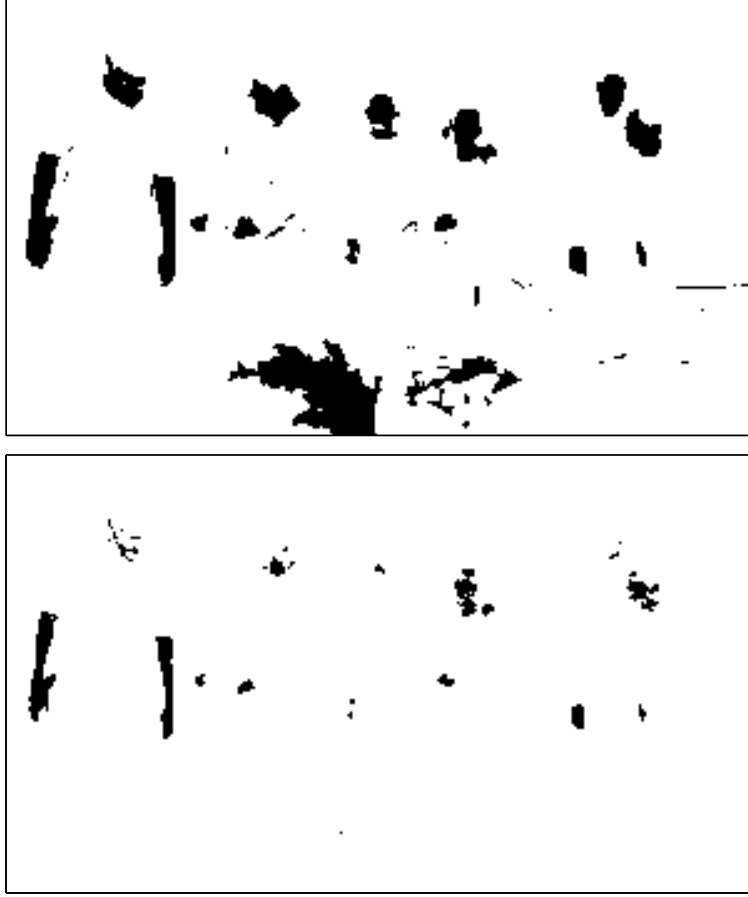
Figure 63:   **Top**: Detection Image with NDSI threshold $\gamma = 0.314$ with $P_D = 0.95$ and corresponding $P_{FA} = 0.0156$. **Bottom**: Detection Image with NDSI threshold $\gamma = 0.589$ with $P_{FA} = 0.0005$ and corresponding $P_D = 0.413$.

as an NDVI threshold of $\alpha = 0.7$ and better performance across the board over an NDVI threshold $\alpha = 0.5$. Figure 66 shows a scatter plot of NDSI values versus NDVI values for both skin and non-skin pixels. NDSI thresholds of $\gamma = 0.259$ and $\gamma = 0.467$ are also displayed on the figure along with a NDSI threshold of $\gamma = 0.6$. Figure 67 (top) shows the result of applying both NDVI and NDSI to the detection problem per Eqn. (30) for an NDVI threshold of $\alpha = 0.6$ and an NDSI threshold of $\gamma = 0.259$ (yielding a 95% detection) while Fig. 67 (bottom) shows the result for $\alpha = 0.6$ and $\gamma = 0.467$ (yielding a 0.5% false alarm rate). Given a fixed NDVI of $\alpha = 0.6$, an NDSI of $\gamma = 0.259$ results in a $P_D = 0.95$ with a $P_{FA} = 0.015$, and an NDSI of $\gamma = 0.467$ results in a $P_{FA} = 0.0005$ with a $P_D = 0.766$.

Figure 64:   Application of NDVI to the suburban test scene with possible false alarm sources.
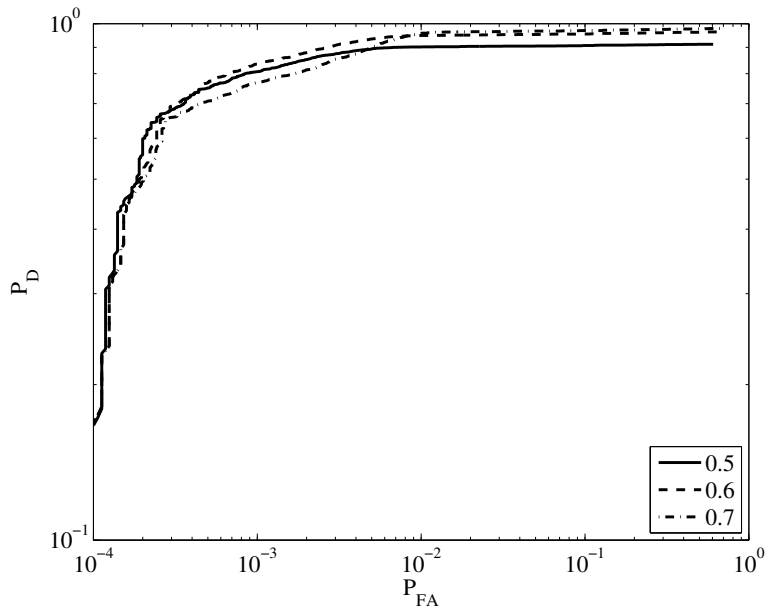
Figure 65:   ROC curves for the rules-based skin detection algorithm per Eqn. (30) varying NDSI with fixed values of NDVI: $\alpha = \{0.5, 0.6, 0.7\}$ (solid, dashed, dashed-dotted respectively).

False detections can be reduced by incorporating the NDGRI algorithm with the NDSI algorithm. The NDGRI algorithm is used to identify pixels that are more green than red. Figure 68 shows the application of the NDGRI algorithm to the test
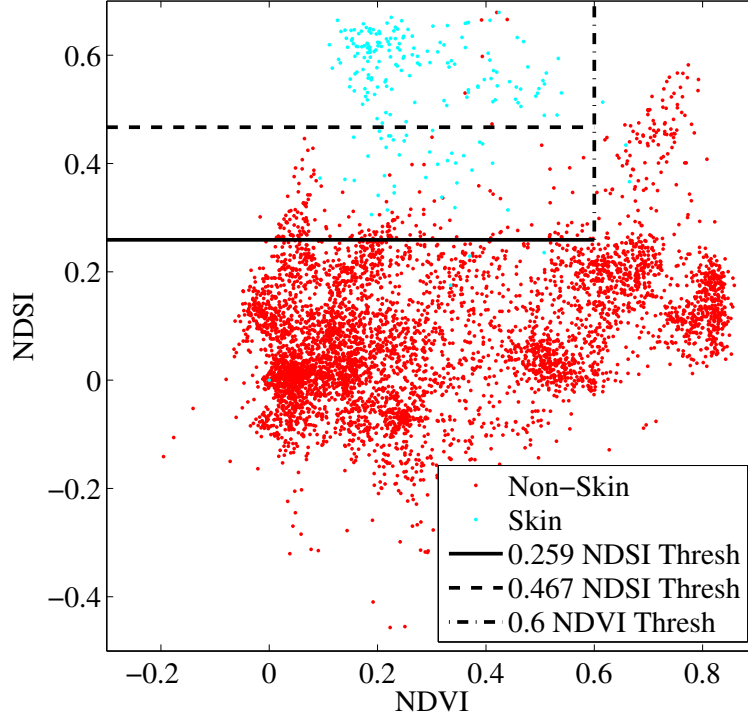
Figure 66: Scatter plot of NDSI versus NDVI values for skin and non-skin pixels. Number of pixels analyzed was decimated for ease of viewing. Skin detection algorithm with NDSI threshold of 0.259 (solid) and NDVI threshold of 0.6 (dashed-dotted) has $P_D = 0.95$ and corresponding $P_{FA} = 0.015$. Skin detection algorithm with NDSI threshold of 0.467 (dashed) and NDVI threshold of 0.6 (dashed-dotted) has $P_D = 0.766$ and corresponding $P_{FA} = 0.0005$.

scene. In general, skin in the scene has an NDGRI value $\beta < -0.3$ while vegetation has a value $\beta > 0$.

Three ROC curves corresponding to varying NDSI threshold γ at three NDGRI values of $\beta = \{-0.2, -0.05, 0.1\}$ are shown in Fig. 69 (solid, dashed, dashed-dotted respectively). For a threshold of $\beta = -0.2$, a maximum $P_D \approx 0.67$ occurs. The reason for the low P_D is some fair skin pixels may be insufficiently more red than green to cross this NDGRI threshold. For a threshold of $\beta = 0.1$, a maximum $P_D = 0.97$ with a resultant $P_{FA} = 0.01$ occurs. A compromise may be to use an NDGRI threshold of $\beta = -0.05$ with $P_D = 0.95$ and $P_{FA} < 0.0065$, which has better overall performance than when $\beta = -0.2$ or $\beta = 0.1$. Figure 70 shows a scatter plot of NDSI values versus NDGRI values for both skin and non-skin pixels. NDSI thresholds of 0.286 and 0.455
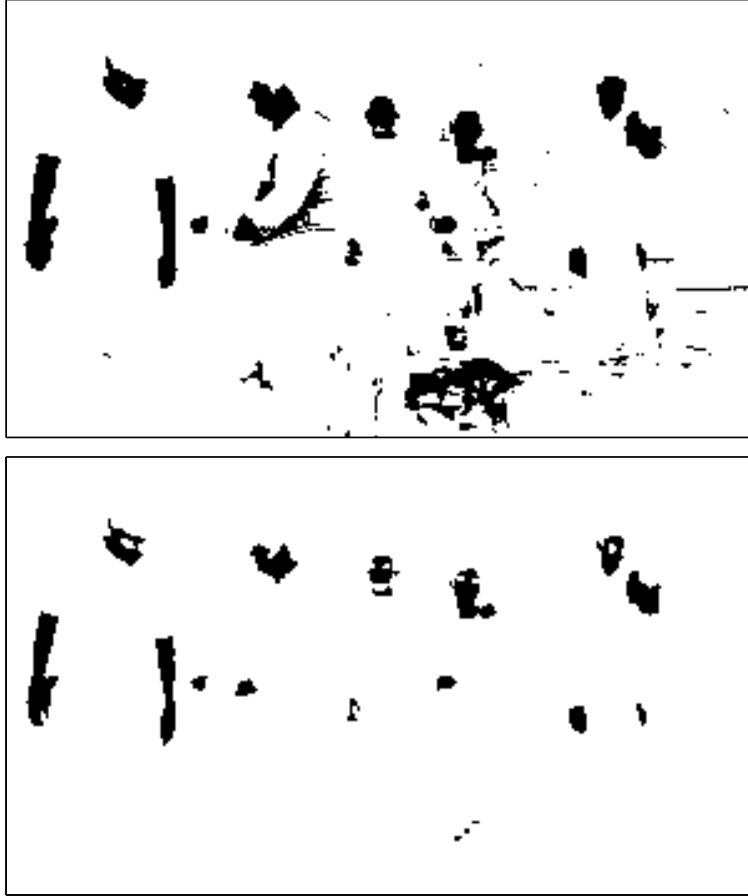
Figure 67: Application of NDSI and NDVI with thresholds for skin detection. **Top**: NDSI threshold of $\gamma = 0.259$ and NDVI threshold of $\alpha = 0.6$ for a $P_D = 0.95$ with a corresponding $P_{FA} = 0.015$. **Bottom**: NDSI threshold of $\gamma = 0.467$ and NDVI threshold of $\alpha = 0.6$ for $P_{FA} = 0.0005$ with a corresponding $P_D = 0.766$.

are also displayed on the figure along with a NDGRI threshold of -0.05. The skin detection results on our test image generated by fixing $\beta = -0.05$ and selecting an NDSI threshold where $P_D = 0.95$ (with a corresponding $P_{FA} = 0.006$) is shown in Fig. 71 (top). Under the same fixed value of $\beta = -0.05$ and choosing the operating point where $P_{FA} = 0.0005$ (with a corresponding $P_D = 0.785$), the resultant detection image is shown in Fig. 71 (bottom).

Figure 68:   Application of NDGRI to image of suburban test scene with potential skin color confusers. Colorbar shows the representative NDGRI values.
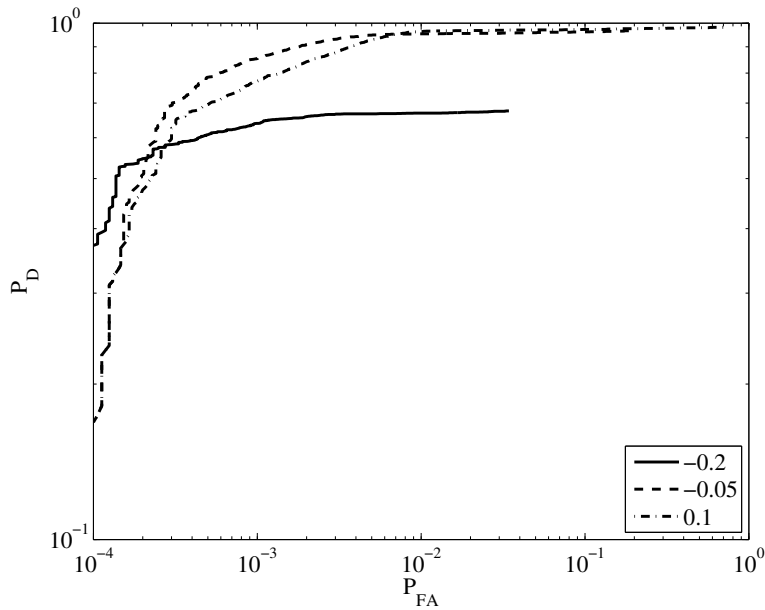
Figure 69:   ROC curves for the rules-based skin detection algorithm per Eqn. (31) varying NDSI with fixed values of NDGRI: $\beta = \{-0.2, -0.05, 0.1\}$ (solid, dashed, dashed-dotted respectively).

4.7   NIMI remote sensing

The selection of which λ value to use for estimating skin reflectance at 685nm is based on the capabilities of the sensor used to collect the hyperspectral image. Smaller values of λ have a greater dynamic range for the NIMI values resulting in a

109
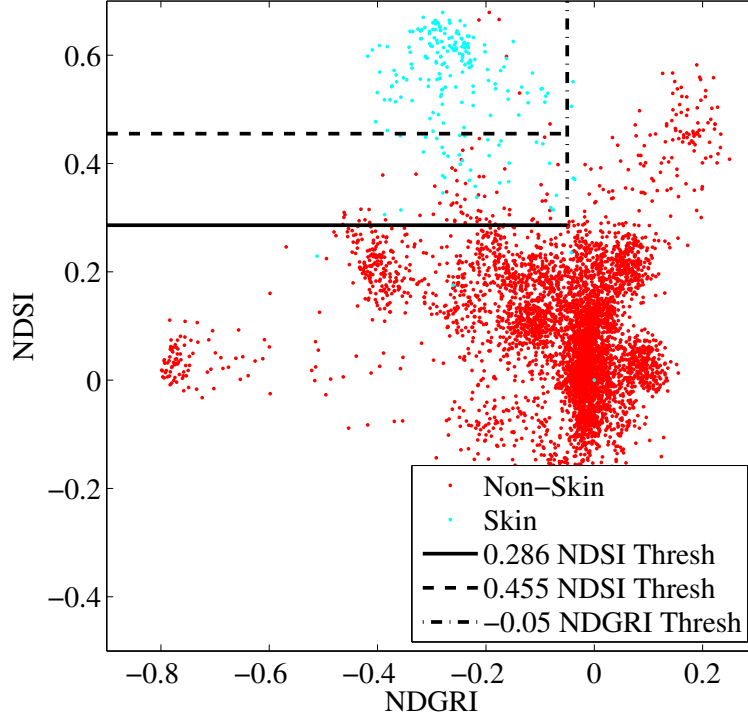
Figure 70: Scatter plot of NDSI versus NDGRI values for skin and non-skin pixels. Number of pixels analyzed was decimated for ease of viewing. Skin detection algorithm with NDSI threshold of 0.286 (solid) and NDGRI threshold of -0.05 (dashed-dotted) has $P_D = 0.95$ and corresponding $P_{FA} = 0.006$. Skin detection algorithm with NDSI threshold of 0.455 (dashed) and NDGRI threshold of -0.05 (dashed-dotted) has $P_D = 0.785$ and corresponding $P_{FA} = 0.0005$.

more accurate estimation of the skin reflectance at 685nm if significant noise is present. However, the response of the sensor at shorter wavelengths must also be taken into consideration. Better results can be expected using the smallest wavelength between 650nm and 950nm assuming the sensor has a good response at that wavelength.

The results of the skin reflectance at 685nm estimation algorithms for the test image in Fig. 72 (top) for a value of λ =685nm Fig. 72 (middle) and λ =850nm (Fig. 72 bottom). The colors of the colorbar on Fig. 72 (bottom) represent the skin color associated with the skin reflectance at 685nm numerical values on the bar. The estimation of skin reflectance at 685nm appears reasonable. The skin reflectance at 685nm estimated for λ =685nm should be the same as λ =850nm. However, as λ increases, the dynamic range for skin reflectance at 685nm estimation is reduced (as
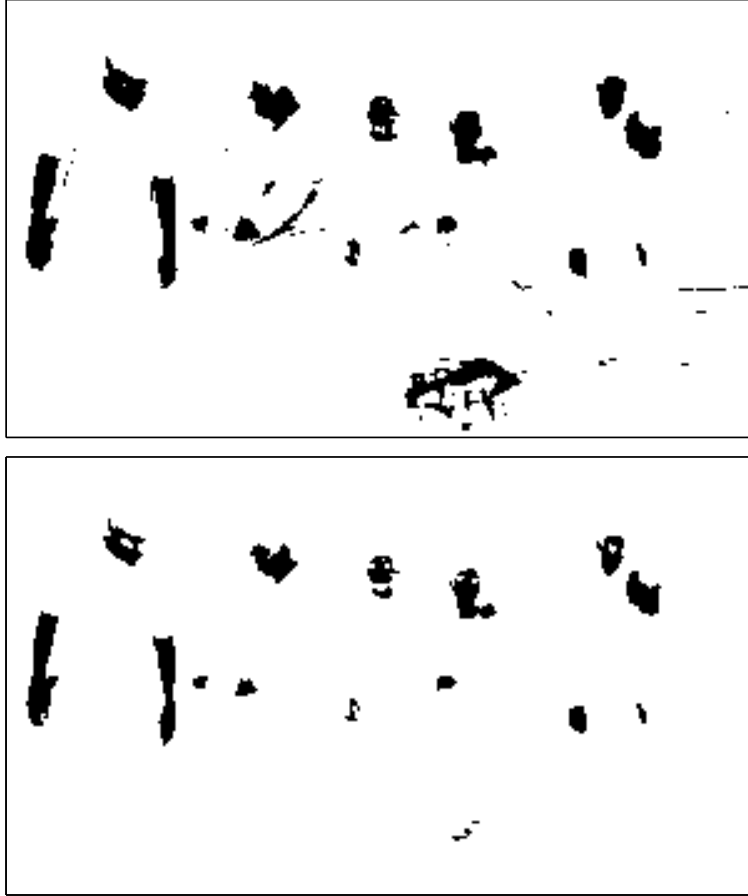
Figure 71: Application of NDSI and NDGRI with thresholds for skin detection. **Top**: NDSI threshold of $\gamma = 0.286$ and NDGRI threshold of $\beta = -0.05$ with $P_D = 0.95$ and corresponding $P_{FA} = 0.006$. **Bottom**: NDSI threshold of $\gamma = 0.455$ and NDGRI threshold of $\beta = -0.05$ with $P_D = 0.785$ and corresponding $P_{FA} = 0.0005$.

shown in Fig. 56). As a result, the results in Fig. 72 (bottom) have a reduced accuracy in pigmentation level compared to the results in Fig. 72 (middle).

The next step in determining the accuracy of the NIMI algorithm is to make a comparison between measured and estimated skin reflectance at 685nm. The ASD FieldSpec3® Spectrometer was used to collect reflectance measurements at 685nm of the left forearms of seven subjects. The NIMI algorithms were then used to estimate the mean reflectance at 685nm of a 3X3 pixel section of the center of the left and right forearms of each of the subjects. Table 13 shows a comparison between the measured reflectance at 685nm for the left forearms and the NIMI algorithm results for the left

Figure 72:   **Top**: Test scene with seven subjects of interest covering the range of Fitzpatrick skin types. Middle: Skin reflectance at 685nm estimate based on estimated reflectance of skin pixels at λ =685nm. **Bottom**: Skin reflectance at 685nm estimate based on estimated reflectance of skin pixels at λ =850nm.

and right forearms of the seven subjects. There is a good correspondence between the measured and estimated results. The subject number from the first column of Table 13 corresponds to the number on the torso of each of the individuals in Fig. 72 (top). Measured skin reflectance for the seven subjects at 685nm ranged from 0.14 to 0.64. For $\lambda = 685$nm, the mean absolute error between measured forearm reflectance

112

Table 13: Estimation of reflectance at 685nm of subjects' forearms in the suburban test image shown in Fig. 59. Values calculated using NIMI for $\lambda = 685$ and $\lambda = 850$

		$\lambda = 685$		$\lambda = 850$	
Subject	**Reflectance**	**Left**	**Right**	**Left**	**Right**
1	0.25	0.25	0.24	0.25	0.26
2	0.19	0.20	0.18	0.22	0.22
3	0.33	0.28	0.30	0.34	0.34
4	0.14	0.15	0.14	0.14	0.12
5	0.64	0.64	0.63	0.55	0.61
6	0.35	0.30	0.24	0.32	0.35
7	0.57	0.68	0.59	0.58	0.54

at 685nm and that estimated by the NIMI algorithm is 0.03. For $\lambda = 850$nm, the mean absolute error is 0.021. The mean of these two results is 0.026.

The values shown in Table 13 are then transformed using Eqn. (39) into melanosome percentages. Limitations are placed on the transformation such that the lowest and highest melanosome levels are 1% and 43% respectively. The results of the transformation are shown in Table 14. According to Table 1, subjects 1, 2, and 4 fall in the category of darkly pigmented (Type V/VI) while subjects 3 and 6 fall in the upper range of moderately pigmented (Type III/IV). Subjects 5 and 7 fall in the category of fairly pigmented (Type I/II).

4.8 Discussion

Algorithms and results for the detection of skin and estimation of pigmentation level in hyperspectral images were presented in this chapter. The algorithms were based on skin reflectance measurements and results from a reflectance model developed for this research. Images used to test the algorithm contained skin with a wide variety of melanosome levels and a variety of skin-color confusers. The detection of skin was conducted with four bands of data in the VIS and NIR. With the proper selection of image bands and detector thresholds, the skin detection algorithm had

Table 14:   Estimation of melanosome levels of subjects' forearms in the suburban test image shown in Fig. 59.

		$\lambda = 685$		$\lambda = 850$	
Subject	**Melanosome Level**	**Left**	**Right**	**Left**	**Right**
1	0.22	0.22	0.23	0.22	0.21
2	0.30	0.29	0.32	0.26	0.26
3	0.14	0.19	0.17	0.14	0.14
4	0.40	0.38	0.40	0.40	0.43
5	0.01	0.01	0.01	0.02	0.01
6	0.13	0.17	0.23	0.15	0.13
7	0.01	0.01	0.01	0.01	0.02

a P_D as high as 0.95 with a P_{FA} of 0.003. Once pixels were identified as skin, the skin melanosome-estimation algorithm was able to successfully determine the skin's melanosome content when compared with color imagery of the test scene. The mean absolute error between data measured by the ASD FieldSpec3® Spectrometer and data estimated by the NIMI algorithm was only 0.026 where the reflectances of the individuals at 685nm ranged from 0.14 to 0.64. This is sufficient to correctly categorize skin based on the Fitzpatrick skin types per Table 2.

V. Conclusions and Future Work

5.1 Introduction

We end our description of this research with conclusions and a discussion of current and future work. Current work includes improvements in the skin detection algorithm and the development of a camera system for real-time skin detection and melanosome-estimation/skin color classification. Future work includes the development of classification algorithms for the amount of blood in skin to assist in determining psycho-physiological responses, and an investigation of how the skin detection algorithm interacts with animal skin.

5.2 Conclusions

For this research we developed a skin reflectance model in the visible (VIS) and near-infrared (NIR) based on the Kubelka-Munk and Fresnel equations. This multi-layer reflectance model incorporates optical coefficients documented in the current literature and measured in the laboratory. Optical coefficients derived from measurements in the laboratory include the absorption coefficient of collagen and an estimate of the reduced scattering coefficient of skin. The model uses six parameters (epidermal melanosome level, dermal blood level, hemoglobin oxygenation percentage, dermal thickness, collagen level, and subcutaneous tissue reflectance) to simulate the wide variety of skin reflectances. These six parameters can be adjusted to match measured skin reflectances with a high degree of accuracy.

The next part of this research uses the skin reflectance model to determine the output of a generic red-green-blue (RGB) color sensor recording skin with various types of illumination. Modeled skin reflectance and blackbody illumination sources were combined to form a reflected radiance. This reflected radiance spectrum was then transformed into the RGB color space. We successfully applied this transformation to a hyperspectral image of an avatar with different skin parameters under different illumination sources.

In the last part of this research, we developed skin detection and melanosome level estimation algorithms for use with remotely sensed hyperspectral data. We applied both algorithms to a suburban scene which included people possessing a variety of pigmentation levels and various skin color confusers. We were able to successfully detect skin with a high probability of detection (P_D) and a low probability of false alarm (P_{FA}). The results of the melanosome level algorithm also compare favorably with an ASD FieldSpec3® Spectrometer measurements of skin in the scene.

There are several unique contributions of this research. First, the absorption coefficient of collagenous protein was measured which is essential for determining the total absorption coefficient of skin. Although the absorption coefficient of collagen has been measured by others [86, 90], our method was novel in that we measured the absorption properties of nearly pure collagen that did not possess the scattering properties of more typical powdered collagen.

Second, is the measuring of skin's reduced scattering coefficient. Given accurate knowledge of the amount of absorption in the skin tissue and the reflectance of subcutaneous tissue, this new scattering coefficient allowed us to create a skin reflectance model with an overall root mean square error of approximately 2% compared to measurements. Although this measurement of the reduced scattering coefficient is significantly different than that measured or estimated by others [35, 72, 78], we show that it is plausible as it was an essential element in creating an accurate model of skin reflectance based on the assumptions made in this research.

Third, the multi-layer skin reflectance model incorporated all the possible reflectance and transmittance paths for light propagating through the skin tissue. Other models only allow for the primary reflectance and transmittance paths of light through the skin tissue [16]. Incorporating all the reflectance and transmittance paths allows for an increase in the number of layers used in the model without a loss of fidelity.

Fourth, sensor response was incorporated with the skin reflectance model to simulate the result of various psycho-physiological responses on the sensor. Knowledge

116

of the lighting conditions in the environment, sensor response, and skin reflectance for various psycho-physiological responses can allow the development of algorithms for detecting psycho-physiological responses for a given sensor.

Fifth, the Normalized Difference Skin Index (NDSI) and Normalized Difference Red Green Index (NDGRI) were developed for use in algorithms that detect skin with a high P_D and a low P_{FA}. The NDSI and NDGRI algorithms are computationally inexpensive and easy to implement with commercial off the shelf equipment. A combination of the NDSI and NDGRI had a P_D as high as 0.95 with a P_{FA} of 0.006 within a typical suburban scene with a wide variety of skin colors.

Finally, an accurate method for remotely determining the pigmentation level of skin in hyperspectral images using the near-infrared Melanosome Index (NIMI) algorithm was demonstrated. The NIMI algorithm was applied to a hyperspectral image containing a wide variety of skin pigmentation levels to determine the reflectance of skin pixels at 685nm where those values varied from 0.14 to 0.64. The mean error for the algorithm results was 0.007 while the standard deviation of the error was 0.037. What makes this method unique is that the assessment of skin color is done using data from the NIR rather than the VIS. This method is also unique in that it is flexible enough to be used with a wide variety of NIR sensors rather than constrained to a specific sensor type.

5.3   Current work

5.3.1   Improved detection algorithm.   Our current skin detection algorithm calculates the NDSI and NDGRI values for an image and then applies thresholds for each metric based on the desired P_D and P_{FA} performance. An area defined as ranging from -1 to 1 for the x-axis and -1 to 1 for the y-axis can define all the possible combinations of NDSI and NDGRI values with the x coordinate defining the NDGRI value and y coordinate defining the NDSI value. The NDSI and NDGRI thresholds then define a rectangular region that goes from -1 to the NDGRI threshold along the x direction and from the NDSI threshold to 1 in the y direction. Adding an

upper threshold for the NDSI value and a lower threshold for the NDGRI value can reduce the area within the NDSI/NDGRI space which would improve the P_{FA} without significantly degrading P_D. We are currently investigating traditional detection methods for the NDGRI/NDSI pair. The key to determining all of these thresholds is an analysis of materials with spectra similar to skin. Examples of materials we are investigating include vegetation, snow, mud, and other water rich materials.

5.3.2 Two camera skin detection system. We are currently developing a skin detection system based on the NDSI algorithm [58] which operates at approximately 20Hz. This project was part of a special study for three masters students to demonstrate the practicality of implementing the skin detection algorithms for use in the field. Two Goodrich NIR cameras are co-located with both having a connection to an image acquisition card on a computer. As shown in Fig. 73, one camera has a filter centered at 1050nm in front of its lens while the other has a filter centered at 1550nm.

Figure 73: Goodrich near-infrared cameras with optical filters at 1050nm and 1550nm (approximately the specified NDSI wavelengths of 1080nm and 1580nm) with bandwidths of 10nm and 12nm respectively. This demonstrates the flexibility of the methodology developed in this dissertation.

For initial tests of the system, all of the blinds in the laboratory were opened to allow sunlight to enter the room. The cameras were placed in front of the windows and the test subject was placed across the laboratory in front of the cameras. For demonstration purposes, the test subject held the monitor that displayed the results of the skin detection algorithm. This allowed the display of the skin detection results to be co-located with the skin within the scene. Figure 74 shows the test subject and the skin detection results on the monitor while Fig. 75 shows a close in view. Accurate detection results require accurate registration of the two cameras. However, since the pair of cameras do not share a single set of optics, they can only be registered to one depth of view. Objects outside the depth of view may not be properly registered. Because of this, there are some false detections at edges within the scene such as the door's edge or the monitor's edges.
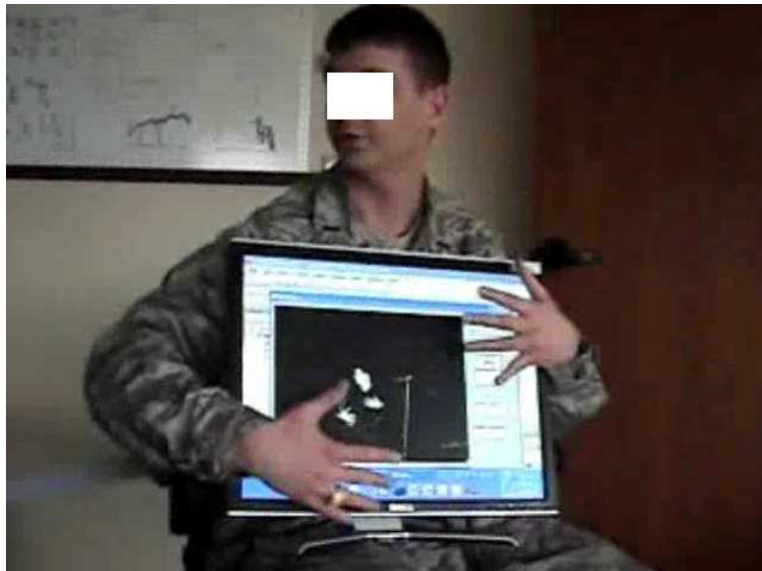
Figure 74:   Skin detection shown on monitor for the two NIR skin detection camera/system with cameras pointing at the subject.

5.3.3 Monocular skin detection system.   The solution to the stereo optics problem is to use a single set of optics for both cameras. To accomplish this, the two cameras will be integrated with a dichroic mirror and a single lens. Light enters through the single lens and is then split into two bands using a dichroic mirror. The

119

Figure 75:   Close in view of skin detection shown on monitor for cameras pointing at the subject. The false detections due to depth of field problems are clearly evident.

dichroic mirror will allow light below a specified wavelength to pass through to one camera while reflecting light above the specific wavelength to the second camera. This will allow the entire scene to be registered for all depths-of-view.

5.3.4 Four camera solution.   A single set of optics, three dichroic mirrors, and four cameras can be used to create a real-time skin detection system that also reduces false alarms and estimates pigmentation level of pixels identified as skin. Once light exits the single set of optics, it is split by a dichroic mirror at approximately 1000nm. Wavelengths above 1000nm are further split into two bands by another dichroic mirror for skin detection. The light from the first dichroic mirror below 1000nm is further split into light above and below 700nm by a third dichroic mirror. The light below 700nm is received by a color camera where the light is split into its RGB channels. Information from the color camera is used to identify false detections using a modified version of the NDGRI. The light above 700nm is the second band used for melanosome estimation. This system is currently being produced as a masters thesis as a result of this dissertation.

120

5.4 Future work

5.4.1 Improving skin reflectance model.   There are multiple areas where the skin reflectance model can be improved. First, we can incorporate additional layers into the model by subdividing the subcutaneous tissue. Subcutaneous tissue can be divided into layers of fat, striated muscle, and possibly bone or cartilage where the optical properties of each of these materials can be measured with an ASD FieldSpec3® Spectrometer. This would be an improvement over using the characteristic subcutaneous spectra with a scale factor. Another area for improvement is the characterization of melanosome scattering. Both the amount and size of melanosomes in the epidermis vary depending on the pigmentation level of skin. Accounting for melanosome scattering would increase the accuracy of the model in the NIR for skin with a high melanosome level. Finally, using different scattering coefficients for the epidermis, papillary dermis, and reticular dermis would improve model accuracy. All three layers have different densities and sizes of collagen fibers which is the primary source of scattering in skin tissue. For simplicity at the cost of accuracy, our model used the same scattering coefficient spectra for all layers of skin (similar to the existing literature).

5.4.2 Remote sensing for triage.   After developing algorithms for detecting skin and determining its pigmentation level, the next step is developing an algorithm for remote sensing of the amount of blood in skin. An algorithm that can successfully detect the blood volume in skin may provide a tool for performing triage. Once skin detection is applied to an image, an analysis of the NDGRI values of the skin pixels can give an indication of the blood volume in the skin. A low blood volume in skin can indicate severe injury or even death. As the blood volume in skin drops, absorption of the blue and green portions of the visible spectrum by hemoglobin also begins to drop. This effect gives skin a paler color. This also means the NDGRI value for the skin pixel also begins to increase. Based on how dark the skin is, an NDGRI threshold can be selected to indicate if the blood volume in the skin is normal or abnormal.

If the NDGRI value is greater than a set threshold for a given skin reflectance at 685nm, the skin pixel can be classified as having an abnormally low blood level. A low NDGRI value can be an indication of an abnormally high amount of blood in the skin which can be an indication of some form of blushing or trauma to the skin.

As a preliminary test of this concept, a hyperspectral image of a cadaver and a live person was collected with the HyperSpecTIR 3 hyperspectral imager. The spectrum of each pixel was then converted to estimated reflectance using the empirical line method. Figure 76 shows a NIR panchromatic image of the scene collected by the camera. Within the scene is the forearm and open palm of a living person with a reclined cadaver below. A nine square inch area of skin on the shoulder of the cadaver is removed to expose the subcutaneous tissue.

Figure 76:   NIR panchromatic image of the palm of a living person above the abdomen of a fair-skinned cadaver. The artifact on the shoulder of the cadaver (right portion of the image) is due to exposed subcutaneous tissue.

The NDGRI algorithm was then applied to the skin pixels as shown in Fig. 77. The palm of the hand of the living person is rich in blood and has no melanin which causes an NDGRI value between -0.3 and -0.25. Because the blood volume of the skin is reduced after death and the skin of the cadaver is fair, the NDGRI value is greater

than -0.2. The exposed subcutaneous tissue has an NDGRI value less than -0.25 since the tissue is still rich in blood. Because gravity has caused some of the blood to pool, areas along the bottom of the cadaver have a slightly lower NDGRI value than areas on the top of the cadaver.
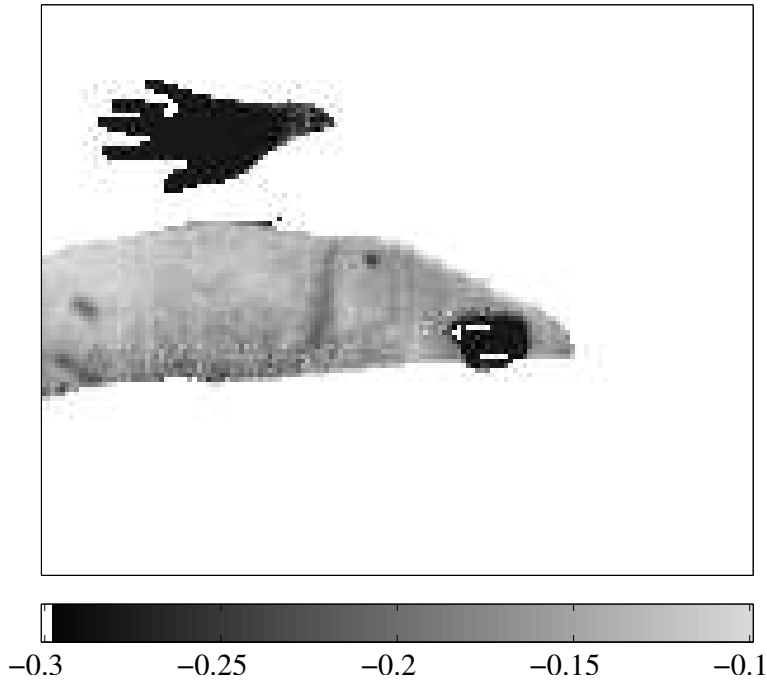
Figure 77:   NDGRI values of the fair-skinned cadaver and the palm of the living person in Fig. 76.

5.4.3   *Animal skin detection.*   One question frequently asked with respect to the skin detection algorithm is "Does it detect animals?" Human and animal skin are biologically similar enough for the answer to be yes. Figure 78 shows a NIR image of a man and his dog (left) and the result of applying the NDSI with threshold to the scene (right). The algorithm does detect exposed skin tissue on the dog such as the skin on the nose and the tongue. However, the algorithm will not detect skin completely covered with fur. With further study, one may be able to model animal skin and be able to distinguish between animal and human skin.

123

Figure 78: **Left:** NIR image of a man and his dog. **Right:** Application of the NDSI thresholded to yield a detection mask.

5.4.4   Psycho-physiological responses.   Deep emotion can manifest itself in people through a variety of physiological responses. One of the most common responses is a change in the amount of blood in the skin of the face. Using the skin reflectance model developed for this work in conjunction with the response of the system used to image the face, one may be able to remotely detect and characterize the level of psycho-physiological responses such as vasodilation and vasoconstriction. These psycho-physiological responses would manifest themselves as changes of color in the skin as demonstrated in Chapter 3.

Appendix A. Human Subjects Research Documents

The following documents in the appendix show memoranda requesting and receiving the proper approvals and support to accomplish the research described in this dissertation. Figures 79, 80, and 81 are a memorandum requestion approval from the AFIT Institutional Review Board (IRB) to collect data from living subjects. Figure 82 is a memorandum from the AFIT IRB giving us an exemption to collect data from human subjects. The main conditions of the data collection are that it does not cause harm to the human subjects and that it does not collect identifiable data from the human subjects. Figure 83 is a letter from the Wright State University Anatomical Gift Program giving us permission to conduct our research on the cadavers in their facility. Figure 84 is a memorandum from the 88th Medical Group IRB supporting the author's work with the pathology department at the Wright-Patterson Medical Center on this research.

DEPARTMENT OF THE AIR FORCE
AIR UNIVERSITY (AETC)

25 January 2008

TO: AFIT IRB Research Reviewer, Maj Alex J. Barelka

FROM: AFIT/ENG Maj Michael J. Mendenhall

SUBJECT: Request for exemption from human experimentation requirements (32 CFR 219, DoDD 3216.2 and AFI 40-402) for detection and classification of human skin in hyperspectral imagery

1. The purpose of this study is to characterize skin reflectance for people of different skin color, detect areas in hyperspectral images that are skin, and determine melanin levels of pixels in hyperspectral images that are identified as skin.

2. This request is based on the Code of Federal Regulations, title 32, part 219, section 101, paragraph (b) (2) Research activities that involve the use of educational tests (cognitive, diagnostic, aptitude, achievement), survey procedures, interview procedures, or observation of public behavior unless: (i) Information obtained is recorded in such a manner that human subjects can be identified, directly or through identifiers linked to the subjects; and (ii) Any disclosure of the human subjects' responses outside the research could reasonably place the subjects at risk of criminal or civil liability or be damaging to the subjects' financial standing, employability, or reputation.

3. The following information is provided to show cause for such an exemption:

    a. Equipment and facilities: The first set of tests will use a reflectance spectrometer to measure skin reflectance. A reflectance spectrometer shines a low-powered (less than 10W) white light onto an object and measures the amount of light reflected off the object for different bands of the electromagnetic spectrum. The second set of tests will use hyperspectral and color cameras to photograph people. A hyperspectral camera photographs multiple bands of light in the visible and infrared regions of the electromagnetic spectrum. For the special case of specimen collection from cadavers, we will use equipment as specified by the collaborating pathologist from the Wright-Patterson AFB medical center, and specimen collection will take place at the Wright-State Boonshoft School of Medicine Anatomical Donor facility.

    b. Subjects: Subjects will be volunteers from AFIT/ENG and AFRL/SNAT recruited by email and in person. The total number of subjects will be approximately 50. There are no inclusion/exclusion criteria for the selection of subjects. The minimum age of subjects will be 22 years.

Figure 79: Page 1 of request for Institutional Review Board (IRB) exemption Memorandum for Record (MFR).

c. Timeframe: The approximate duration of the study is two years. Hyperspectral images of human subjects will be collected under various seasonal conditions, daylight conditions, and weather conditions.

d. Data collected: Data will be conducted from living subjects (with consent) and cadavers (with permission from Wright-State University).

    i) Living subjects: The first set of data collected will consist of skin reflectance measurements of people using the reflectance spectrometer. The second set of data collected will consist of hyperspectral images with people in them. A group of people will be asked to gather within the field of view of the camera. They will be asked to pose and stay still for 10 seconds while the camera collects the image. Afterwards they can resume their normal activity. Information collected from the living subjects is provided on the living subject collection form presented as Attachment 1. No personal identifiers or demographic data will be collected.

    ii) Cadavers: The first set of data collected will consist of skin reflectance measurements of cadavers using the reflectance spectrometer, just as is accomplished with the living subjects. The second set of data collected will consist of hyperspectral images obtained from a tripod-mounted instrument and accompanied color imagery of the same location. The third data collected will be tissues samples removed from the cadavers. Initial specimen extraction will be accompanied by a pathologist from Wright-Patterson AFB medical center. Information collected from the cadaver is provided on the cadaver collection form presented as Attachment 2. No personal identification data will be collected. Information recorded about the extracted tissue samples in no way allows one to identify the individual they came from. As such, the extracted tissue samples are de-identified.

e. Risks to Subjects: The light radiated on the subject by the reflectance spectrometer poses no risk to the subjects. The light radiated on the individuals is less than a standard flashlight radiating one centimeter away from the skin of the subject for approximately 10 seconds. Collection of reflectance measurements of skin poses negligible risk for identification of individuals. For the images collected by hyperspectral cameras there is one possible risk. Individuals may be identifiable in the images if they are too close to the camera when the camera is collecting an image. To mitigate this risk hyperspectral images will not be taken if an individual is judged to be too close to the camera. After an image is collected, if it is judged that an individual can be identified within the image, the image will be immediately deleted.

f. Informed consent: All subjects are self-selected to volunteer to participate in the collection of the hyperspectral images. No adverse action is taken against those who choose not to participate. Subjects are made aware of the nature and purpose of the

Figure 80:   Page 2 of request for IRB exemption MFR.

research, sponsors of the research, and disposition of the images. A copy of the Privacy Act Statement of 1974 is presented for their review.

4. Vitas for Maj Mendenhall and Maj Nunez are provided in Attachments 3 & 4 respectively. Completion certificates for human subjects exemption training are provided in Attachments 5 & 6.

5. If you have any questions about this request, please contact Maj Michael J. Mendenhall at DSN 785-3636x 4614 or via e-mail at michael.mendenhall@afit.edu.

MICHAEL J. MENDENHALL, Major, USAF, PhD
Principal Investigator
Assistant Professor of Electrical Engineering
Air Force Institute of Technology

7 Attachments
1. Living subjects collection form
2. Cadaver collection form
3. Vita for Maj Michael J. Mendenhall
4. Vita for Maj Abel S. Nunez
5. Human Subjects Training Certification for Maj Michael J. Mendenhall
6. Human Subjects Training Certification for Maj Abel S. Nunez
7. Abstract: Detection of Human Skin and Determination of Skin Color in Hyperspectral Imagery

Attachment 7:
Abstract: Detection of Human Skin and Determination of Skin Color in Hyperspectral Imagery

The goal of this project is to identify pixels in hyperspectral images that are human skin. One of the challenges in doing this is that skin color varies from person to person. To solve this problem a skin model was created which calculates a reflectance spectrum for different amounts of melanin. The main assumption in the model is that everybody's skin is alike except for the amount of melanin. The results of the skin model can then be validated by comparing its results with measurements of skin reflectance from different people. Based on the skin model, a method was developed to identify pixels in hyperspectral images that are skin. Once those pixels are identified another algorithm can be used to estimate the melanin level of each of the skin pixels.

Figure 81:   Page 3 of request for IRB exemption MFR.

DEPARTMENT OF THE AIR FORCE
AIR UNIVERSITY (AETC)

25 January 2008

TO: AFIT/ENG Maj Michael J. Mendenhall

FROM: AFIT IRB Research Reviewer, Maj Alex J. Barelka

SUBJECT: Human subjects IRB exemption determination for proposed research and data collection

1. I have reviewed your study for the detection, classification, and characterization of human skin in hyperspectral imagery and found that your study qualifies for an IRB exemption.

2. Per 32 CFR 219.101 (b)(2), Research involving the use of educational tests (cognitive, diagnostic, aptitude, achievement), survey procedures, interview procedures or observation of public behavior, unless: (i) information obtained is recorded in such a manner that human subjects can be identified, directly or through identifiers linked to the subjects; and (ii) any disclosure of the human subjects' responses outside the research could reasonably place the subjects at risk of criminal or civil liability or be damaging to the subjects' financial standing, employability, or reputation is exempt.

3. Your study qualifies for this exemption because you are not collecting any identifying information, the demographic data you are collecting cannot realistically be expected to identify a specific subject, and your experimental methodology does not pose a risk (physical or otherwise) to the subjects.

4. The portion of your research involving the use of cadavers does not require IRB approval for human subject research. This is due to the fact that you are not using tissue from living subjects and when you receive the samples they are de-identified.

5. As a reminder, this determination pertains only to the Federal, DoD, and Air Force regulations that govern the use of human subjects in research. Please remember that you are also required to report any unforeseen adverse event to this office immediately

ALEX J. BARELKA, Maj, USAF, PhD, PMP
AFIT IRB Research Reviewer

Figure 82:   AFIT human subjects IRB exemption MFR.

BOONSHOFT SCHOOL *of* MEDICINE
WRIGHT STATE UNIVERSITY

ANATOMICAL GIFT PROGRAM

3640 Col. Glenn Hwy., Dayton, OH 45435-0001
(937) 775-3066; FAX (937) 775-3417
med.wright.edu/agp

Frank Nagy, Ph.D., Director
frank.nagy@wright.edu

February 20, 2008

Maj. Michael J. Mendenhall, Ph.D.
Air Force Institute of Technology
2950 Hobson Way
Wright-Patterson AFB, OH 45433

Dear Colleagues,

It is with great pleasure that I am able to accept your proposal entitled *Collection Plan: Hyperspectral Skin Reflectance Measurement and Skin Tissue Sample Extraction* and to confirm my personal commitment as well as that of the Anatomical Gift Program to partner with the Air Force Institute of Technology in this project. I am prepared to offer support to you and Maj. Abel S. Nunez for the completion of this work by providing you with limited workspace adequate to your needs in the laboratories of the Anatomical Gift Program. The purpose of this will be to collect data reflected in the above referenced project. From both scientific and ethical perspectives, I find considerable merit in, and am in complete support of, the research described in your proposal.

Prior to their deaths, the donors from whom you propose to obtain tissue samples all signed consent forms releasing their remains to the Anatomical Gift Program and the Boonshoft School of Medicine for either educational and/or scientific research purposes. The protocols described in your proposal are certainly within the bounds of the expectations of our donors and their families and have my complete support.

If there are questions regarding this support, please feel free to contact me via email at frank.nagy@wright.edu or by phone at 937.775-2253 (office) or 937.344-2253 (mobile).
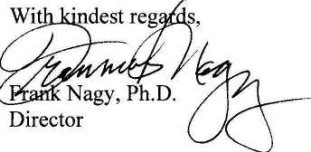
With kindest regards,

Frank Nagy, Ph.D.
Director

Figure 83:   Accepted proposal from the Director of the Anatomical Gift Program, Boonshoft School of Medicine, Wright State University.

DEPARTMENT OF THE AIR FORCE
88th MEDICAL GROUP
WRIGHT-PATTERSON AIR FORCE BASE OHIO

12 May 2008

88th Medical Group/SGNE
4881 Sugar Maple Drive
Wright-Patterson AFB OH 45433-5529

Maj Michael J. Mendenhall, PhD
AFIT/ENG
2950 Hobson Way
Wright-Patterson AFB OH 45433

Dear Maj Mendenhall,

It is with pleasure that I submit this letter of intent to confirm the 88th Medical Group's commitment to partner with the Air Force Institute of Technology (AFIT) on the *Request for Support for Skin Tissue Analysis* MFR dated 6 April 2008. Specifically, Maj Heidi Bertram, M.D., and the pathology lab from the Department of Pathology will collaborate with Maj Michael J. Mendenhall, PhD, and Maj Abel S. Nunez from AFIT, on the preparation of skin tissue samples and the analysis of those samples to include tissue layer thickness, estimation of melanin content in the skin, and digital imagery of the tissues. Please contact me at nathan.kellett@wpafb.af.mil or (937) 257-1430 if you have any questions or require additional information. Thank you.

Respectfully,

NATHAN T. KELLETT
Captain, USAF, MSC
Chair, Institutional Review Board

Figure 84:   Accepted proposal from the 88th Medical Group IRB.

Appendix B. CIE Colorspace Values

Table 15 give the values of $x(\lambda)$, $y(\lambda)$, and $z(\lambda)$ for values of λ ranging from 380nm through 825nm. These three functions along with the reflectance spectra are used to calculate values of X, Y, and Z for the reflectance spectra for use in Eqn. 24. Values for $x(\lambda)$, $y(\lambda)$, and $z(\lambda)$ are derived from [32].

Table 15:   Values of $x(\lambda)$, $y(\lambda)$, and $z(\lambda)$ for CIE Color Space [32]

Wavelength	$x(\lambda)$	$y(\lambda)$	$z(\lambda)$
380	2.69E-03	2.00E-04	1.23E-02
385	5.31E-03	3.96E-04	2.42E-02
390	1.08E-02	8.00E-04	4.93E-02
395	2.08E-02	1.55E-03	9.51E-02
400	3.80E-02	2.80E-03	1.74E-01
405	6.32E-02	4.66E-03	2.90E-01
410	9.99E-02	7.40E-03	4.61E-01
415	1.58E-01	1.18E-02	7.32E-01
420	2.29E-01	1.75E-02	1.07E+00
425	2.81E-01	2.27E-02	1.31E+00
430	3.11E-01	2.73E-02	1.47E+00
435	3.31E-01	3.26E-02	1.58E+00
440	3.33E-01	3.79E-02	1.62E+00
445	3.17E-01	4.24E-02	1.57E+00
450	2.89E-01	4.68E-02	1.47E+00
455	2.60E-01	5.21E-02	1.37E+00
460	2.33E-01	6.00E-02	1.29E+00
465	2.10E-01	7.29E-02	1.24E+00
470	1.75E-01	9.10E-02	1.11E+00
475	1.33E-01	1.13E-01	9.42E-01

Wavelength	$x(\lambda)$	$y(\lambda)$	$z(\lambda)$
480	9.19E-02	1.39E-01	7.56E-01
485	5.70E-02	1.70E-01	5.86E-01
490	3.17E-02	2.08E-01	4.47E-01
495	1.46E-02	2.58E-01	3.41E-01
500	4.85E-03	3.23E-01	2.64E-01
505	2.32E-03	4.05E-01	2.06E-01
510	9.29E-03	5.03E-01	1.54E-01
515	2.93E-02	6.08E-01	1.09E-01
520	6.38E-02	7.10E-01	7.66E-02
525	1.11E-01	7.95E-01	5.62E-02
530	1.67E-01	8.62E-01	4.14E-02
535	2.28E-01	9.15E-01	2.94E-02
540	2.93E-01	9.54E-01	2.00E-02
545	3.62E-01	9.80E-01	1.33E-02
550	4.36E-01	9.95E-01	8.78E-03
555	5.15E-01	1.00E+00	5.86E-03
560	5.97E-01	9.95E-01	4.05E-03
565	6.81E-01	9.79E-01	2.92E-03
570	7.64E-01	9.52E-01	2.28E-03
575	8.44E-01	9.16E-01	1.97E-03
580	9.16E-01	8.70E-01	1.81E-03
585	9.77E-01	8.16E-01	1.54E-03
590	1.02E+00	7.57E-01	1.23E-03
595	1.05E+00	6.95E-01	1.12E-03
600	1.06E+00	6.31E-01	9.06E-04
605	1.04E+00	5.67E-01	6.95E-04

Wavelength	$x(\lambda)$	$y(\lambda)$	$z(\lambda)$
610	9.92E-01	5.03E-01	4.29E-04
615	9.29E-01	4.42E-01	3.18E-04
620	8.43E-01	3.81E-01	2.56E-04
625	7.40E-01	3.21E-01	1.57E-04
630	6.33E-01	2.65E-01	9.77E-05
635	5.34E-01	2.17E-01	6.89E-05
640	4.41E-01	1.75E-01	5.12E-05
645	3.55E-01	1.38E-01	3.60E-05
650	2.79E-01	1.07E-01	2.42E-05
655	2.15E-01	8.17E-02	1.69E-05
660	1.62E-01	6.10E-02	1.19E-05
665	1.18E-01	4.43E-02	8.15E-06
670	8.58E-02	3.20E-02	5.60E-06
675	6.31E-02	2.35E-02	3.95E-06
680	4.58E-02	1.70E-02	2.79E-06
685	3.21E-02	1.19E-02	1.92E-06
690	2.22E-02	8.21E-03	1.31E-06
695	1.56E-02	5.77E-03	9.15E-07
700	1.11E-02	4.10E-03	6.48E-07
705	7.92E-03	2.93E-03	4.64E-07
710	5.65E-03	2.09E-03	3.33E-07
715	4.00E-03	1.48E-03	2.38E-07
720	2.83E-03	1.05E-03	1.70E-07
725	1.99E-03	7.40E-04	1.22E-07
730	1.40E-03	5.20E-04	8.71E-08
735	9.70E-04	3.61E-04	6.15E-08

wavelength	$x(\lambda)$	$y(\lambda)$	$z(\lambda)$
740	6.68E-04	2.49E-04	4.32E-08
745	4.61E-04	1.72E-04	3.04E-08
750	3.21E-04	1.20E-04	2.16E-08
755	2.26E-04	8.46E-05	1.55E-08
760	1.60E-04	6.00E-05	1.12E-08
765	1.13E-04	4.24E-05	8.09E-09
770	7.95E-05	3.00E-05	5.83E-09
775	5.61E-05	2.12E-05	4.21E-09
780	3.95E-05	1.50E-05	3.04E-09
785	2.79E-05	1.06E-05	2.19E-09
790	1.96E-05	7.47E-06	1.58E-09
795	1.38E-05	5.26E-06	1.13E-09
800	9.67E-06	3.70E-06	8.16E-10
805	6.79E-06	2.61E-06	5.86E-10
810	4.77E-06	1.84E-06	4.21E-10
815	3.36E-06	1.30E-06	3.03E-10
820	2.35E-06	9.11E-07	2.18E-10
825	1.64E-06	6.36E-07	1.55E-10

Appendix C.   Comparison of Modeled and Measured Skin Reflectances

The following tables give the skin layer depths and the parameters used for comparison with each of the 76 skin reflectances collected. Table 16 gives the name of the skin layers and their assigned layer number. Table 17 and Table 18 give the thicknesses for the skin layers. Note for samples 1 through 24, a generic set of skin thicknesses is used while for the rest of the samples, the values measured by the Wright Patterson AFB Medical Center Department of Pathology are used. Reflectance measurements for samples 1 through 24 were conducted in vivo so skin thicknesses were not available. The model parameters are optimized to reduce the mean square error between measured and modeled skin reflectance. Tables 19, 20, and 21 list the optimized model parameters for each sample. Figures 85 through 122 display the comparisons between measured and modeled results for each sample.

Table 16:   Skin layer names

Layer Name	Layer Number
Stratum Corneum	1
Stratum Lucidum	2
Stratum Granulosum	3
Stratum Spinosum	4
Stratum Basale	5
Papillary Dermis	6
Upper Blood Net Dermis	7
Reticular Dermis	8
Deep Blood Net Dermis	9

Table 17:   Skin layer depths in centimeters for skin samples 1 through 50.

#	Layer								
	1	**2**	**3**	**4**	**5**	**6**	**7**	**8**	**9**
1-24	0.0020	0.0010	0.0010	0.0045	0.0015	0.0150	0.0080	0.1000	0.0080
25	0.0030	0.0004	0.0004	0.0020	0.0007	0.0101	0.0050	0.2090	0.0110
26	0.0018	0.0002	0.0002	0.0010	0.0003	0.0067	0.0033	0.1900	0.0100
27	0.0028	0.0003	0.0003	0.0014	0.0005	0.0097	0.0048	0.1810	0.0095
28	0.0020	0.0003	0.0003	0.0014	0.0005	0.0084	0.0041	0.1045	0.0055
29	0.0035	0.0005	0.0005	0.0024	0.0008	0.0034	0.0017	0.0903	0.0048
30	0.0024	0.0002	0.0002	0.0010	0.0003	0.0084	0.0041	0.0594	0.0031
31	0.0039	0.0003	0.0003	0.0013	0.0004	0.0047	0.0023	0.0765	0.0040
32	0.0035	0.0008	0.0008	0.0037	0.0012	0.0067	0.0033	0.1211	0.0064
33	0.0140	0.0043	0.0043	0.0195	0.0065	0.0117	0.0058	0.0926	0.0049
34	0.0043	0.0005	0.0005	0.0023	0.0008	0.0050	0.0025	0.0760	0.0040
35	0.0043	0.0002	0.0002	0.0008	0.0003	0.0141	0.0069	0.2176	0.0115
36	0.0025	0.0003	0.0003	0.0014	0.0005	0.0097	0.0048	0.4019	0.0212
37	0.0073	0.0037	0.0037	0.0165	0.0055	0.0013	0.0007	0.0812	0.0043
38	0.0045	0.0011	0.0011	0.0049	0.0016	0.0017	0.0008	0.1354	0.0071
39	0.0035	0.0008	0.0008	0.0034	0.0011	0.0013	0.0007	0.1905	0.0100
40	0.0020	0.0004	0.0004	0.0017	0.0006	0.0117	0.0058	0.1995	0.0105
41	0.0049	0.0014	0.0014	0.0061	0.0020	0.0144	0.0071	0.0903	0.0048
42	0.0030	0.0074	0.0074	0.0335	0.0112	0.0134	0.0066	0.2019	0.0106
43	0.0015	0.0003	0.0003	0.0013	0.0004	0.0067	0.0033	0.0865	0.0046
44	0.0020	0.0066	0.0066	0.0298	0.0099	0.0101	0.0050	0.1663	0.0088
45	0.0100	0.0008	0.0008	0.0037	0.0012	0.0302	0.0149	0.1805	0.0095
46	0.0043	0.0003	0.0003	0.0014	0.0005	0.0121	0.0059	0.0808	0.0043
47	0.0050	0.0002	0.0002	0.0010	0.0003	0.0151	0.0074	0.2161	0.0114
48	0.0033	0.0002	0.0002	0.0009	0.0003	0.0067	0.0033	0.5819	0.0306
49	0.0060	0.0021	0.0021	0.0094	0.0031	0.0075	0.0037	0.0748	0.0039
50	0.0048	0.0007	0.0007	0.0030	0.0010	0.0084	0.0041	0.1140	0.0060

Table 18: Skin layer depths in centimeters for skin samples 51 through 76.

	Layer								
#	1	2	3	4	5	6	7	8	9
51	0.0044	0.0022	0.0022	0.0101	0.0034	0.0067	0.0033	0.0380	0.0020
52	0.0030	0.0003	0.0003	0.0011	0.0004	0.0101	0.0050	0.1520	0.0080
53	0.0025	0.0003	0.0003	0.0013	0.0004	0.0057	0.0028	0.2494	0.0131
54	0.0030	0.0004	0.0004	0.0018	0.0006	0.0067	0.0033	0.1924	0.0101
55	0.0013	0.0004	0.0004	0.0017	0.0006	0.0087	0.0043	0.1876	0.0099
56	0.0028	0.0003	0.0003	0.0011	0.0004	0.0102	0.0050	0.1069	0.0056
57	0.0160	0.0058	0.0058	0.0259	0.0086	0.0012	0.0006	0.1805	0.0095
58	0.0038	0.0006	0.0006	0.0025	0.0008	0.0013	0.0007	0.2731	0.0144
59	0.0048	0.0003	0.0003	0.0015	0.0005	0.0018	0.0009	0.2423	0.0128
60	0.0023	0.0002	0.0002	0.0010	0.0003	0.0040	0.0020	0.3515	0.0185
61	0.0025	0.0003	0.0003	0.0014	0.0005	0.0020	0.0010	0.3776	0.0199
62	0.0120	0.0028	0.0028	0.0124	0.0041	0.0027	0.0013	0.1425	0.0075
63	0.0290	0.0050	0.0050	0.0225	0.0075	0.0067	0.0033	0.1473	0.0078
64	0.0038	0.0014	0.0014	0.0062	0.0021	0.0050	0.0025	0.4038	0.0213
65	0.0028	0.0004	0.0004	0.0020	0.0007	0.0184	0.0091	0.2541	0.0134
66	0.0040	0.0007	0.0007	0.0030	0.0010	0.0328	0.0162	0.2090	0.0110
67	0.0038	0.0003	0.0003	0.0014	0.0005	0.0201	0.0099	0.2494	0.0131
68	0.0035	0.0002	0.0002	0.0010	0.0003	0.0117	0.0058	0.1544	0.0081
69	0.0043	0.0003	0.0003	0.0015	0.0005	0.0025	0.0012	0.1306	0.0069
70	0.0038	0.0006	0.0006	0.0028	0.0009	0.0059	0.0029	0.3206	0.0169
71	0.0033	0.0004	0.0004	0.0020	0.0007	0.0121	0.0059	0.2850	0.0150
72	0.0038	0.0005	0.0005	0.0021	0.0007	0.0087	0.0043	0.2565	0.0135
73	0.0035	0.0003	0.0003	0.0014	0.0005	0.0064	0.0031	0.2138	0.0113
74	0.0030	0.0003	0.0003	0.0014	0.0005	0.0067	0.0033	0.2209	0.0116
75	0.0043	0.0003	0.0003	0.0014	0.0005	0.0050	0.0025	0.3088	0.0163
76	0.0040	0.0003	0.0003	0.0014	0.0005	0.0074	0.0036	0.2304	0.0121

Table 19:   Skin reflectance model parameters for best match with measured data.

Sample	Melanosome Fraction	Blood Level	Blood Oxy. %	Dermal Depth	Collagen Fraction	Sub Cut. Scale
1	0.0168	0.8429	0.3406	0.7536	0.1500	0.8353
2	0.0587	0.9946	0.3719	0.6511	0.1500	0.8495
3	0.0440	0.9315	0.2038	0.7021	0.1500	0.7390
4	0.0479	1.4839	0.3564	1.8932	0.2834	0.6726
5	0.0220	0.8228	0.3548	0.6625	0.1775	0.9176
6	0.0431	1.1008	0.3775	1.5946	0.1500	0.8236
7	0.0773	1.4889	0.3765	1.3238	0.2819	0.8409
8	0.0303	1.8019	0.2000	1.7916	0.3000	0.8860
9	0.0329	0.6829	0.2203	0.9372	0.2110	1.0000
10	0.0447	1.3665	0.3848	1.7639	0.1500	0.8232
11	0.0210	1.2768	0.2000	0.5704	0.1500	0.8102
12	0.0401	1.3027	0.3980	1.2975	0.1500	0.8575
13	0.0411	1.0834	0.2345	1.1157	0.2908	0.9089
14	0.0231	1.5828	0.2000	0.5829	0.2323	0.8320
15	0.3395	0.7846	0.2000	0.5000	0.3000	1.0000
16	0.2926	2.0000	0.2000	0.5000	0.3000	1.0000
17	0.1570	1.3414	0.2000	1.5272	0.3000	0.9856
18	0.1352	1.2478	0.2051	0.9955	0.3000	1.0000
19	0.3122	2.0000	0.2000	0.5000	0.3000	1.0000
20	0.0498	1.1671	0.4170	0.6112	0.3000	0.9575
21	0.0471	1.9281	0.4158	0.6033	0.2855	0.8625
22	0.2956	2.0000	0.2000	0.6736	0.3000	1.0000
23	0.2109	2.0000	0.2000	0.5000	0.3000	1.0000
24	0.0475	1.6971	0.2739	0.5000	0.1500	1.0000

Table 20: Skin reflectance model parameters for best match with measured data continued.

Sample	Melanosome Fraction	Blood Level	Blood Oxy. %	Dermal Depth	Collagen Fraction	Sub Cut. Scale
25	0.0577	0.1686	0.9000	1.0000	0.1500	1.0000
26	0.0986	0.0000	0.9000	1.0000	0.1500	1.0000
27	0.0686	0.0000	0.9000	1.0000	0.1500	0.8933
28	0.0701	0.2903	0.0000	1.0000	0.1500	0.8363
29	0.0422	0.0541	0.2637	1.0000	0.1500	0.8616
30	0.1268	0.0000	0.9000	1.0000	0.1500	0.8147
31	0.0676	0.1432	0.0000	1.0000	0.1500	0.8551
32	0.0492	0.0000	0.9000	1.0000	0.1500	0.7942
33	0.0150	0.0000	0.9000	1.0000	0.1500	0.8704
34	0.0345	0.0000	0.9000	1.0000	0.1500	0.7438
35	0.2769	0.0000	0.9000	1.0000	0.1500	0.7029
36	0.1653	0.0939	0.9000	1.0000	0.1500	0.7762
37	0.0166	1.2364	0.9000	1.0000	0.1500	1.0000
38	0.0306	1.0028	0.0000	1.0000	0.1500	0.8255
39	0.0362	0.0000	0.9000	1.0000	0.1500	0.9191
40	0.0437	0.0000	0.9000	1.0000	0.1500	0.7764
41	0.0346	0.0000	0.9000	1.0000	0.1500	0.9458
42	0.0150	0.0000	0.9000	1.0000	0.1500	1.0000
43	0.1968	0.0000	0.9000	1.0000	0.2990	1.0000
44	0.0166	0.0000	0.9000	1.0000	0.1500	1.0000
45	0.0271	0.1519	0.4001	1.0000	0.1500	0.7418
46	0.0936	0.2929	0.0000	1.0000	0.1500	0.6527
47	0.1927	0.2948	0.0000	1.0000	0.3000	0.6000
48	0.3306	0.0976	0.0000	1.0000	0.3000	0.6000
49	0.0260	0.0000	0.9000	1.0000	0.1500	0.8772
50	0.0725	0.0000	0.9000	1.0000	0.1500	0.9803

Table 21:   Skin model parameters for best match with measured data.

Sample	Melanosome Fraction	Blood Level	Blood Oxy. %	Dermal Depth	Collagen Fraction	Sub Cut. Scale
51	0.0224	0.0000	0.9000	1.0000	0.1500	0.8895
52	0.2159	0.0000	0.9000	1.0000	0.2331	1.0000
53	0.1450	0.1865	0.2326	1.0000	0.1500	0.6000
54	0.0650	0.2517	0.0000	1.0000	0.1500	0.6000
55	0.0857	0.0412	0.0000	1.0000	0.1581	0.9703
56	0.1270	0.1075	0.1841	1.0000	0.1500	0.8235
57	0.0150	0.0000	0.9000	1.0000	0.1500	1.0000
58	0.0896	0.2381	0.0000	1.0000	0.1500	0.7761
59	0.1868	0.0000	0.9000	1.0000	0.1500	0.6659
60	0.1942	0.0000	0.9000	1.0000	0.2070	0.6000
61	0.1533	0.0000	0.9000	1.0000	0.2969	0.6000
62	0.0150	0.0000	0.9000	1.0000	0.1500	0.8942
63	0.0150	0.0000	0.9000	1.0000	0.1500	1.0000
64	0.0309	0.1637	0.0000	1.0000	0.2614	0.6000
65	0.0735	0.0000	0.9000	1.0000	0.1500	0.6000
66	0.1192	0.0000	0.9000	1.0000	0.1500	0.6778
67	0.1196	0.1321	0.0000	1.0000	0.1500	0.7166
68	0.1869	0.1120	0.0000	1.0000	0.2469	0.7874
69	0.1181	0.0000	0.0000	1.0000	0.3000	0.7562
70	0.0955	0.1663	0.0000	1.0000	0.3000	0.6159
71	0.0653	0.0712	0.0000	1.0000	0.2917	0.9797
72	0.0975	0.0000	0.9000	1.0000	0.1500	0.9135
73	0.0997	0.0385	0.0000	1.0000	0.2050	0.6788
74	0.1038	0.0844	0.0000	1.0000	0.2344	0.8384
75	0.1249	0.0000	0.9000	1.0000	0.3000	0.6000
76	0.1135	0.0559	0.0000	1.0000	0.2716	0.6253

Table 22: RMSE between measured and modeled skin reflectance

| Sample	RMSE	Sample	RMSE	Sample	RMSE
1	0.01290	25	0.01113	51	0.01948
2	0.00578	26	0.02445	52	0.02384
3	0.00693	27	0.02300	53	0.02386
4	0.01222	28	0.00782	54	0.02116
5	0.00889	29	0.01820	55	0.01291
6	0.00879	30	0.00637	56	0.01511
7	0.00709	31	0.01920	57	0.05031
8	0.01208	32	0.01393	58	0.00992
9	0.00965	33	0.05596	59	0.01403
10	0.00933	34	0.01702	60	0.02988
11	0.00750	35	0.02082	61	0.02793
12	0.00759	36	0.02454	62	0.04866
13	0.00834	37	0.02775	63	0.06410
14	0.00766	38	0.01949	64	0.01593
15	0.01438	39	0.02212	65	0.01899
16	0.01515	40	0.03078	66	0.01675
17	0.00932	41	0.03355	67	0.01468
18	0.01187	42	0.04625	68	0.01437
19	0.02981	43	0.02670	69	0.01189
20	0.01376	44	0.03198	70	0.01639
21	0.01165	45	0.02649	71	0.01667
22	0.00896	46	0.01364	72	0.01730
23	0.01313	47	0.04236	73	0.03118
24	0.01503	48	0.04154	74	0.02682
		49	0.02637	75	0.02816
		50	0.01933	76	0.02491
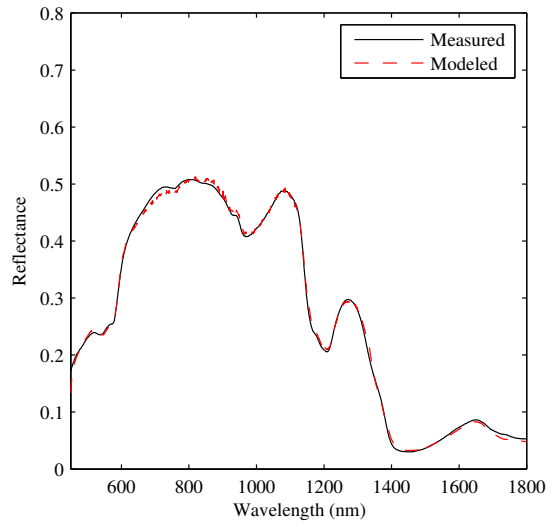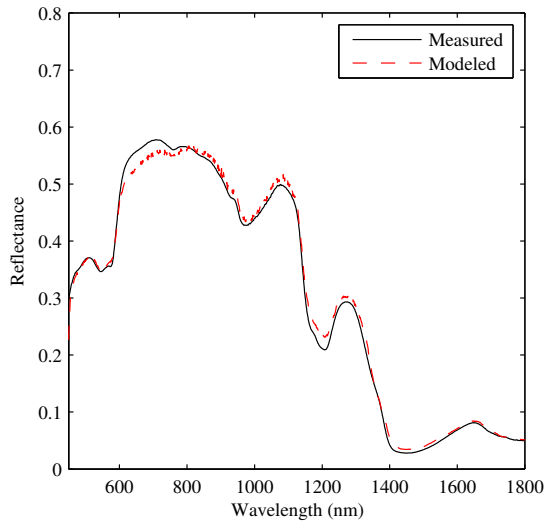
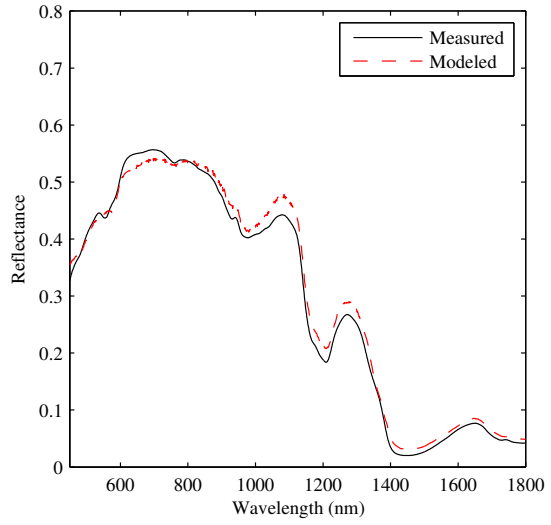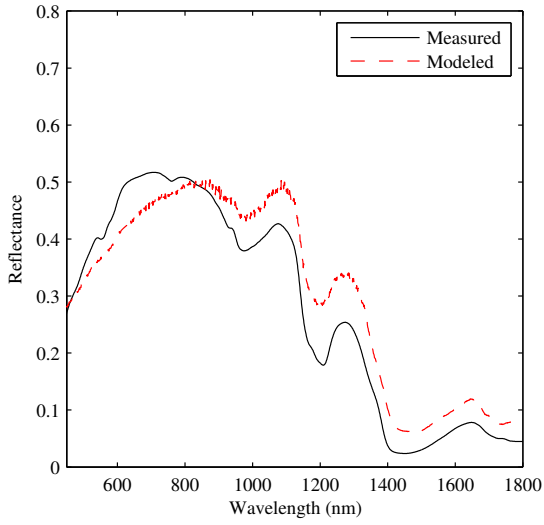Figure 85: Comparison of model and measured living skin reflectance for sample 1 and 2.
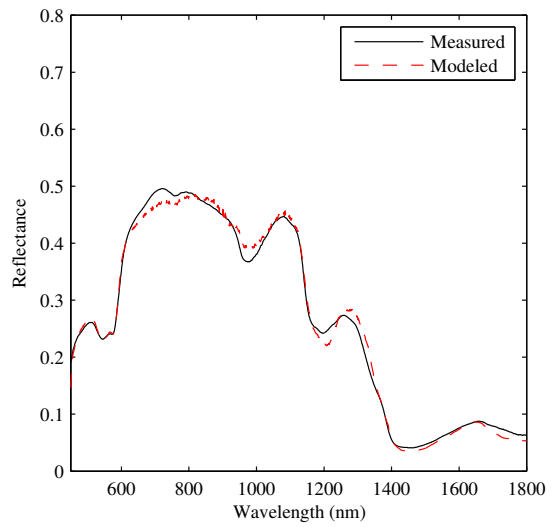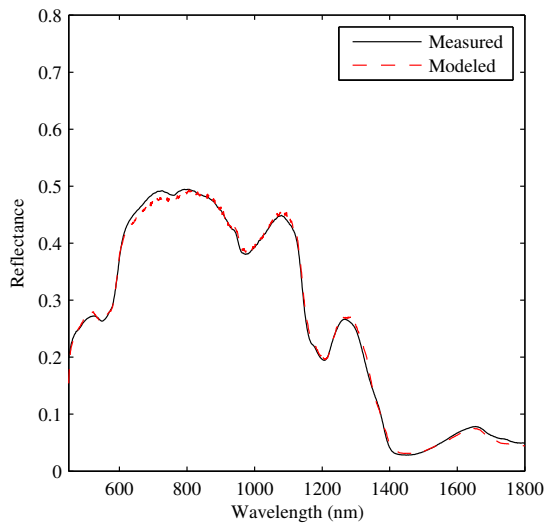
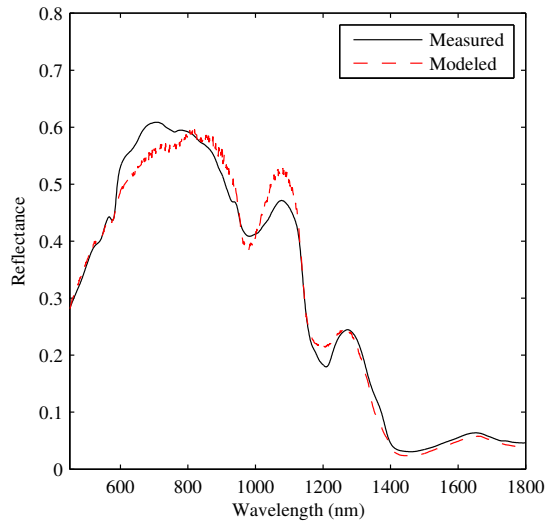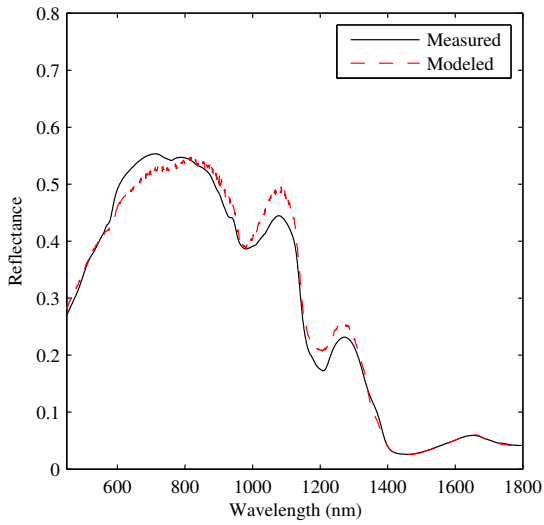Figure 86: Comparison of model and measured living skin reflectance for sample 3 and 4.
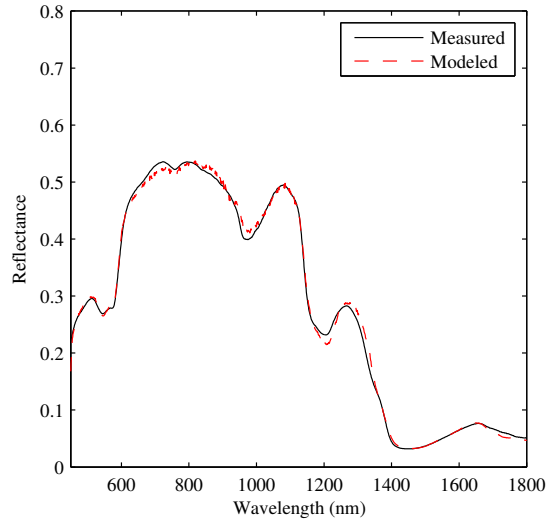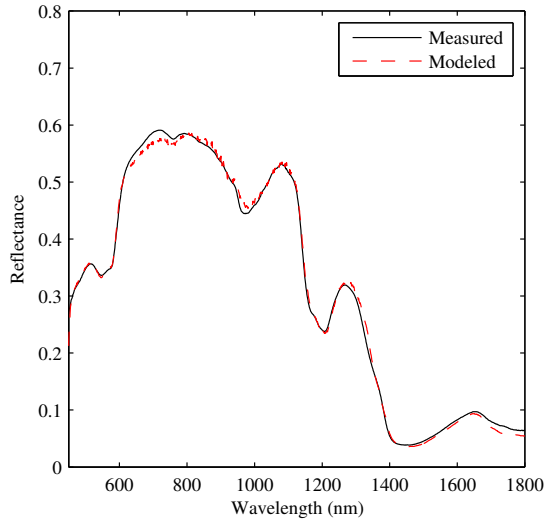
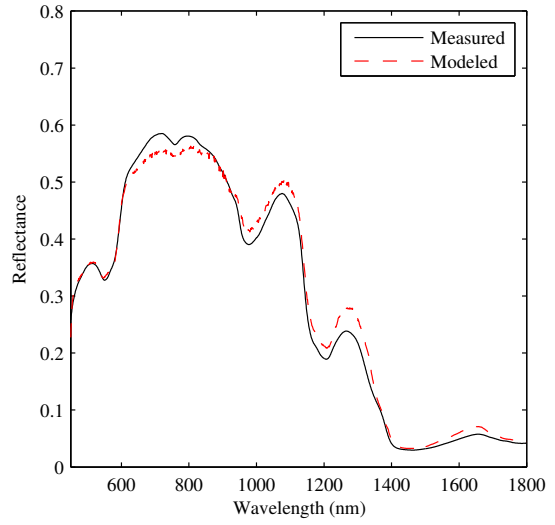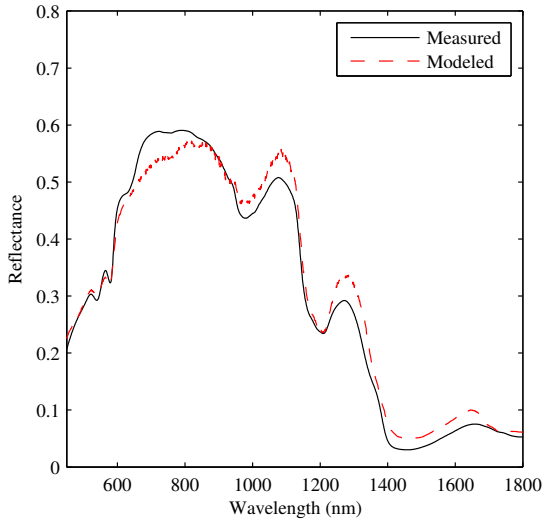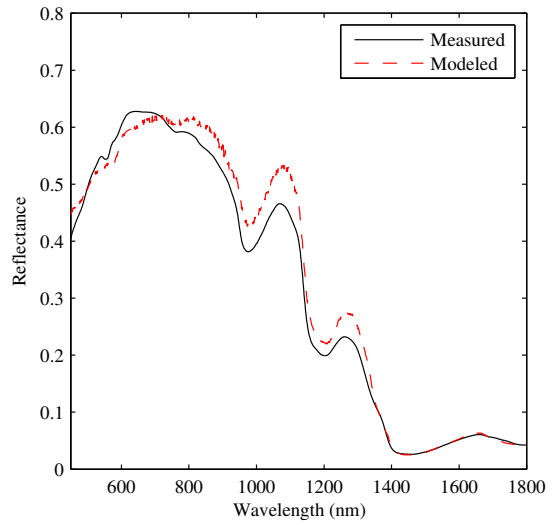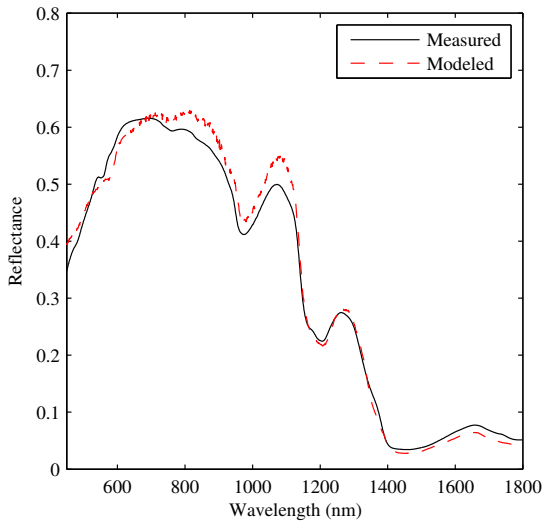Figure 87: Comparison of model and measured living skin reflectance for sample 5 and 6.
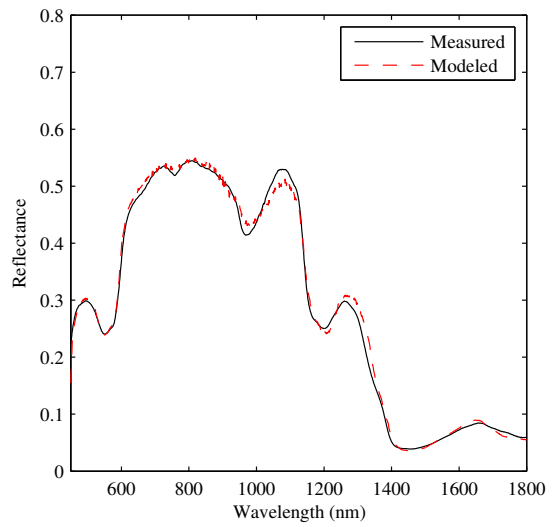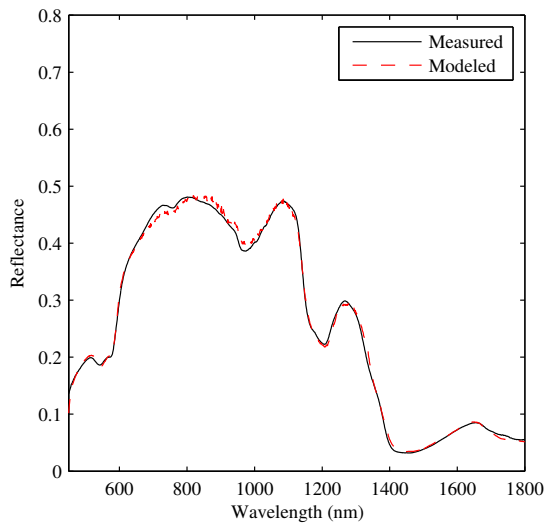
Figure 88: Comparison of model and measured living skin reflectance for sample 7 and 8.
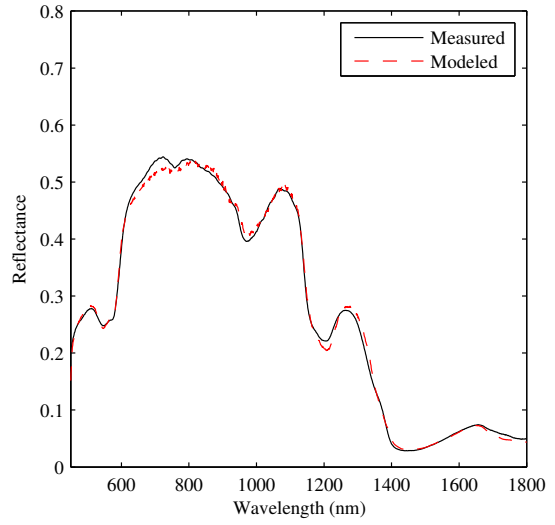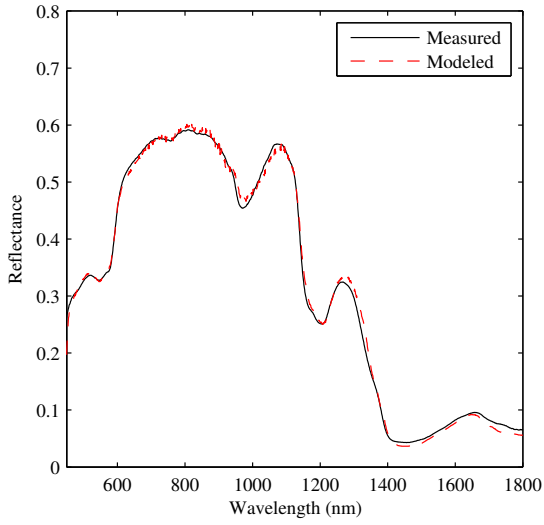
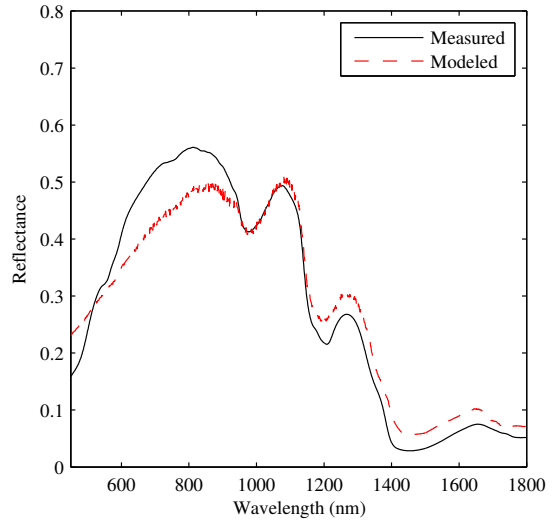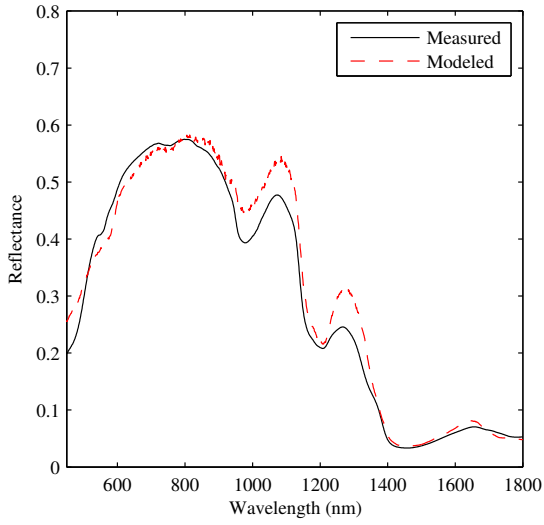Figure 89:   Comparison of model and measured living skin reflectance for sample 9 and 10.
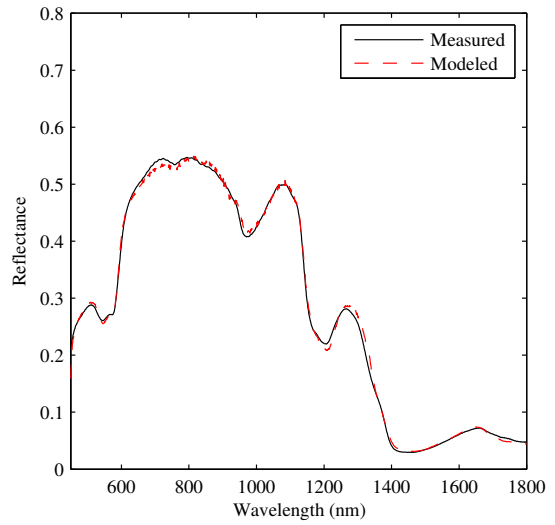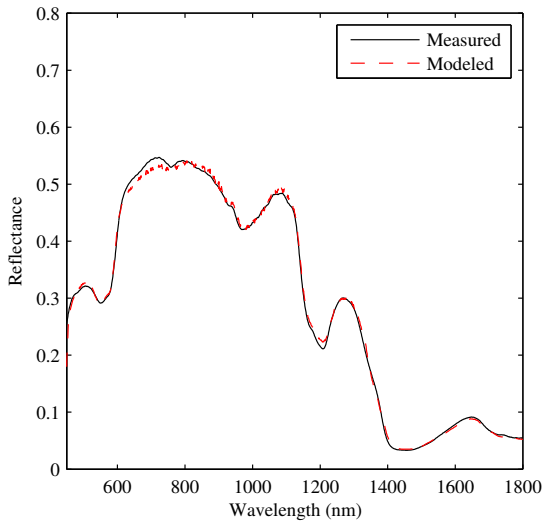
Figure 90:   Comparison of model and measured living skin reflectance for sample 11 and 12.
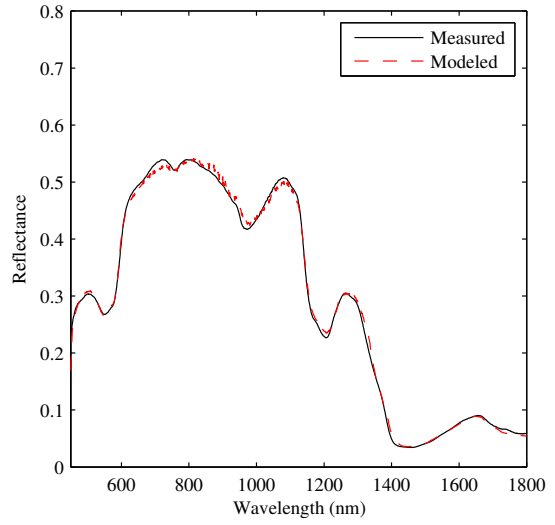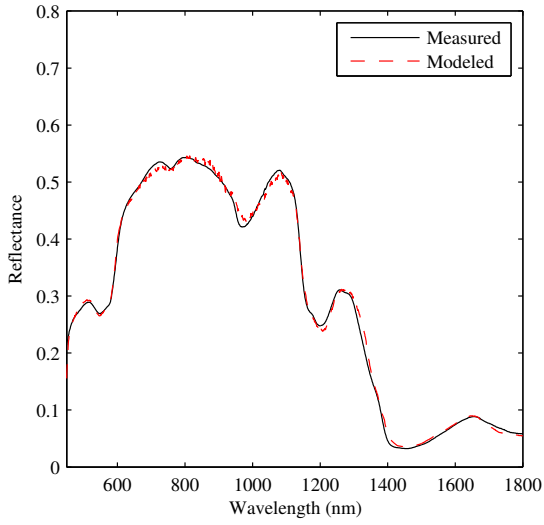
Figure 91:   Comparison of model and measured living skin reflectance for sample 13 and 14.
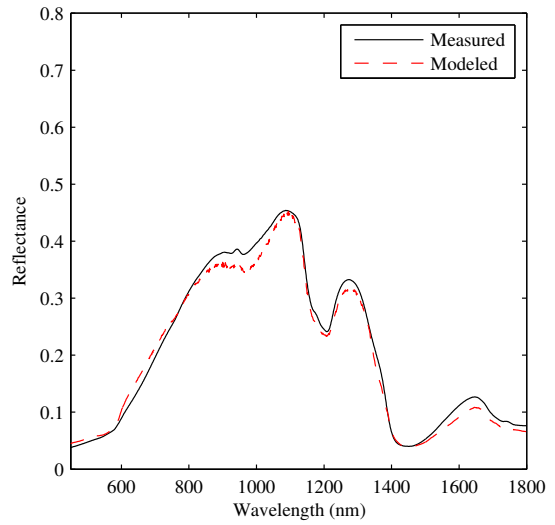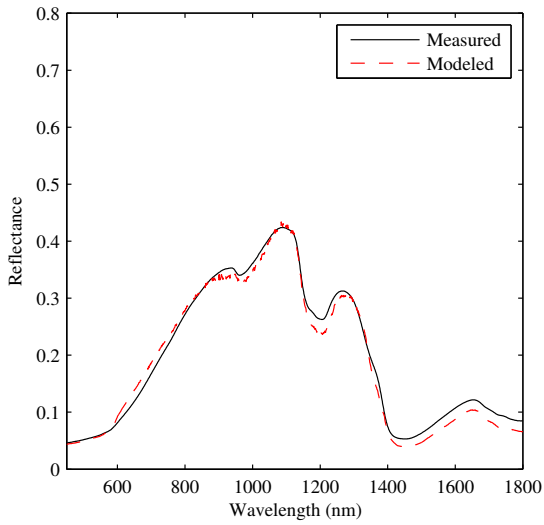
Figure 92:   Comparison of model and measured living skin reflectance for sample 15 and 16.
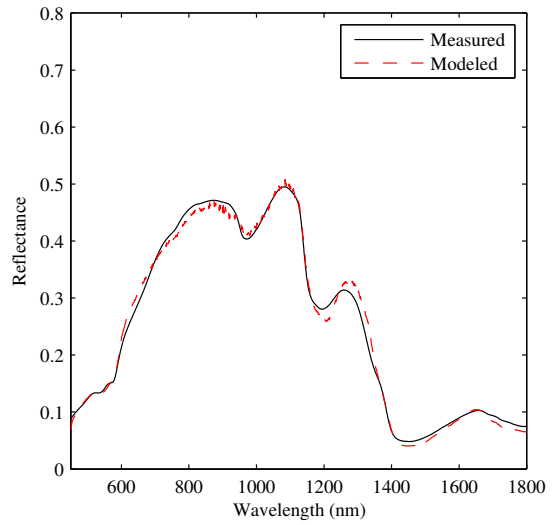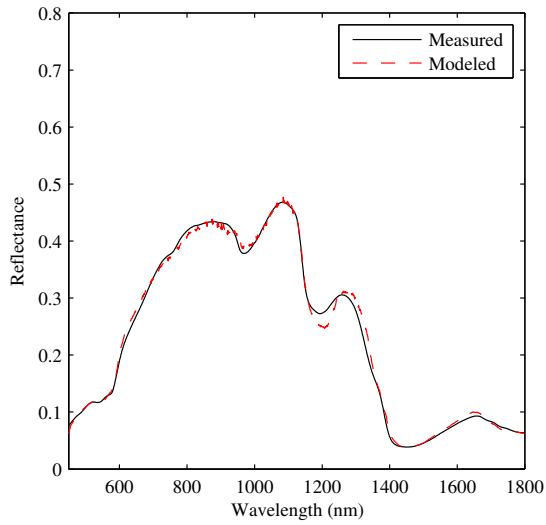
Figure 93: Comparison of model and measured living skin reflectance for sample 17 and 18.
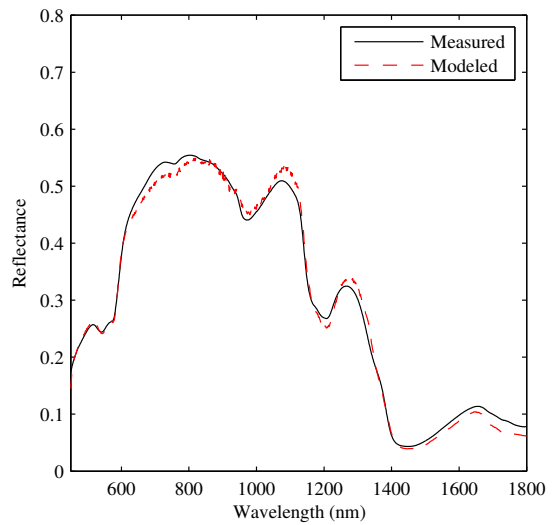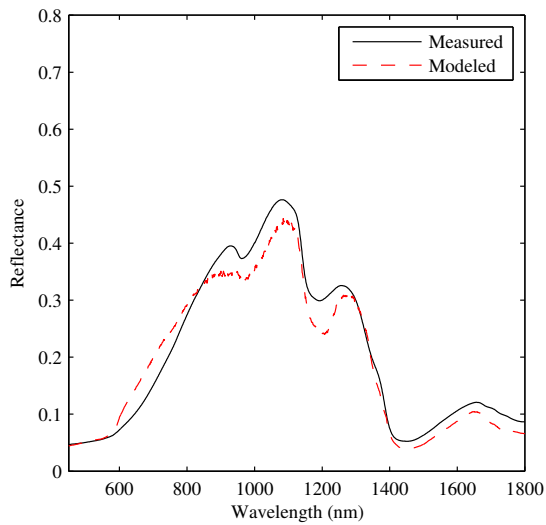
Figure 94: Comparison of model and measured living skin reflectance for sample 19 and 20.
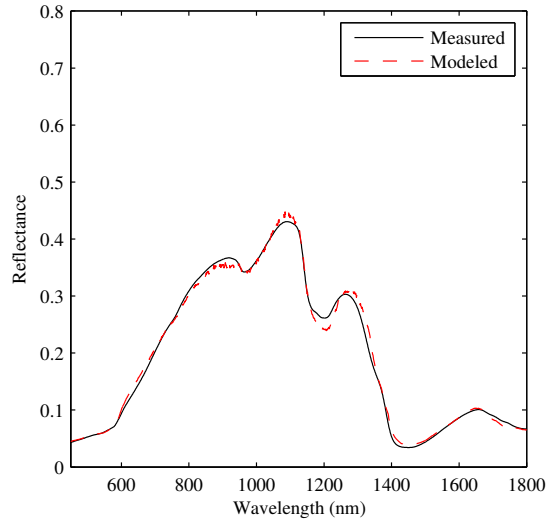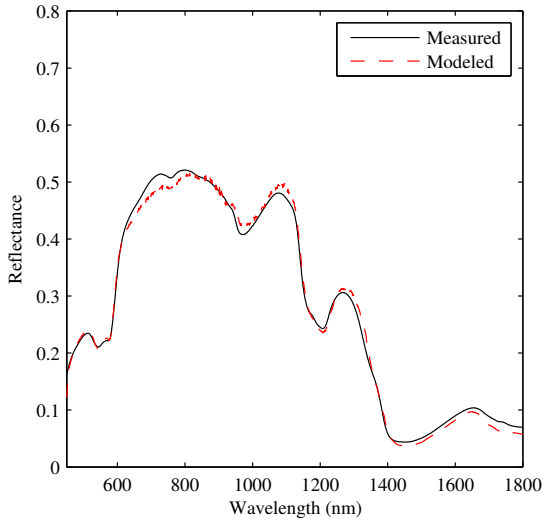
Figure 95: Comparison of model and measured living skin reflectance for sample 21 and 22.
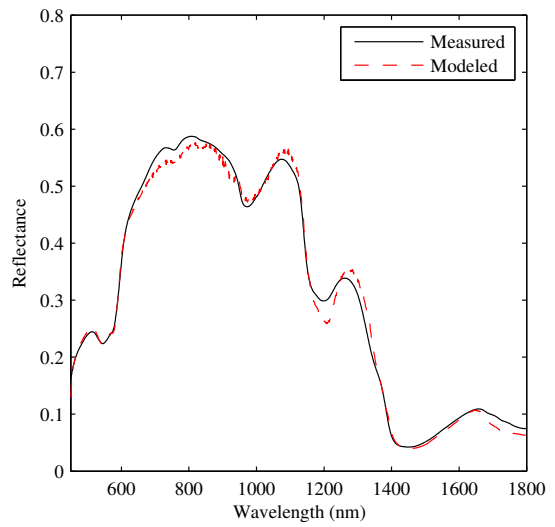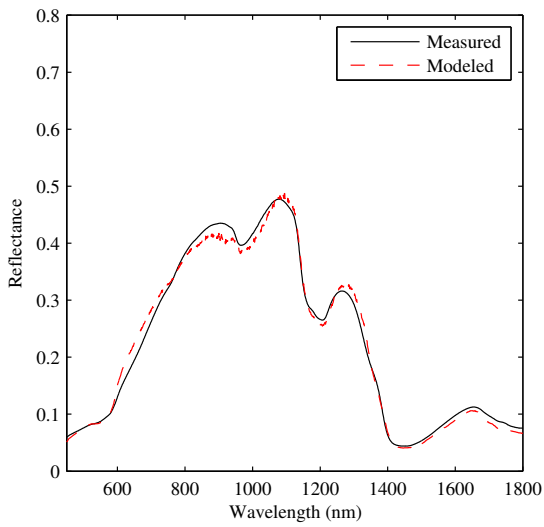
Figure 96: Comparison of model and measured living skin reflectance for sample 23 and 24.
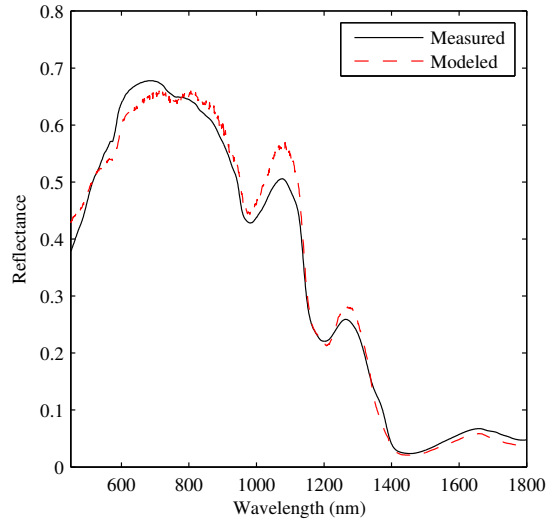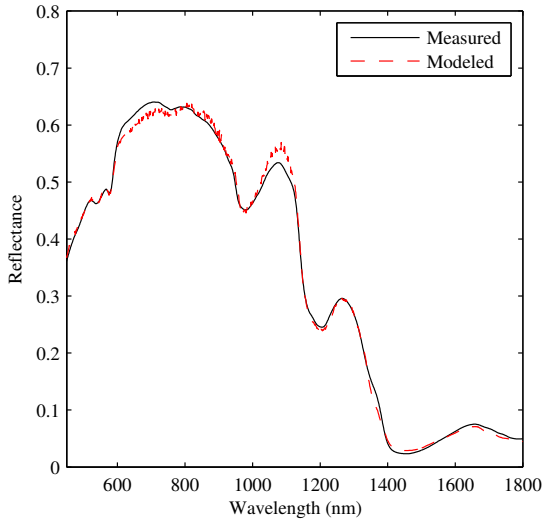
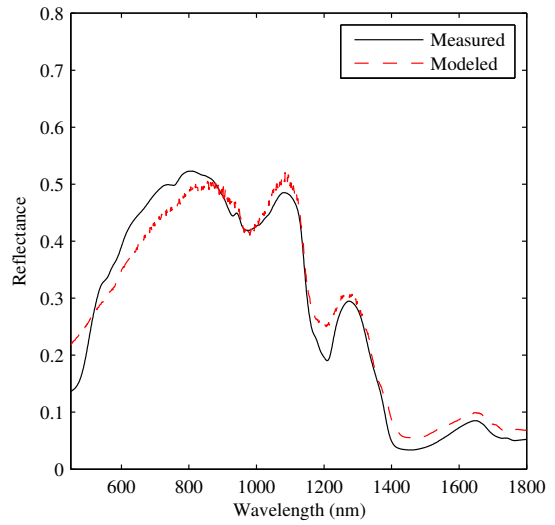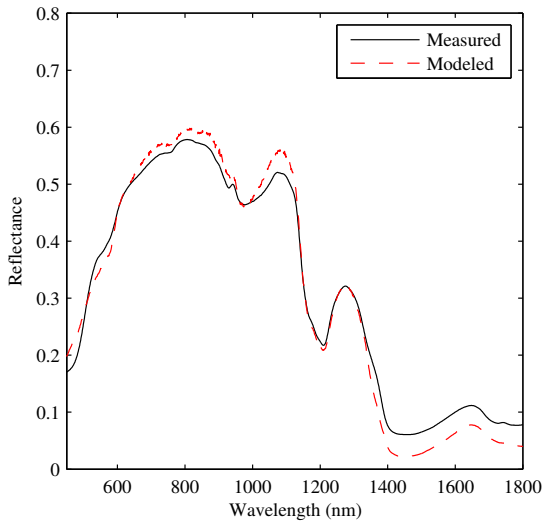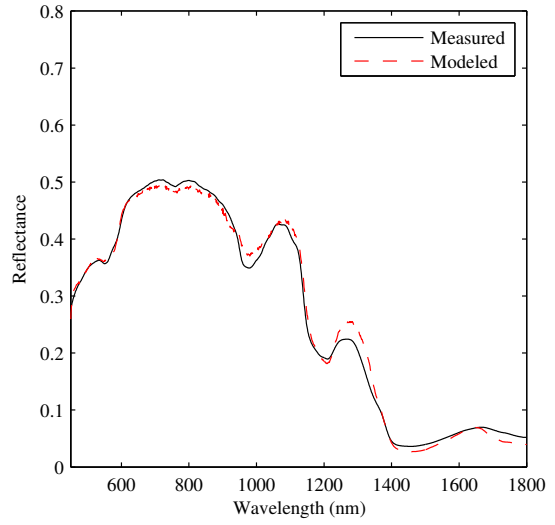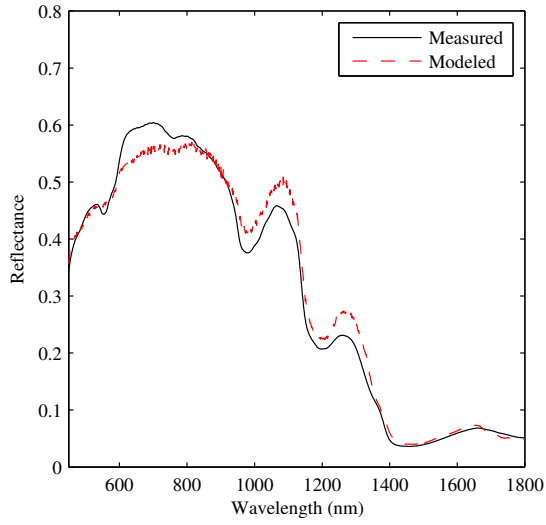Figure 97: Comparison of model and measured cadaver skin reflectance for sample 25 and 26.
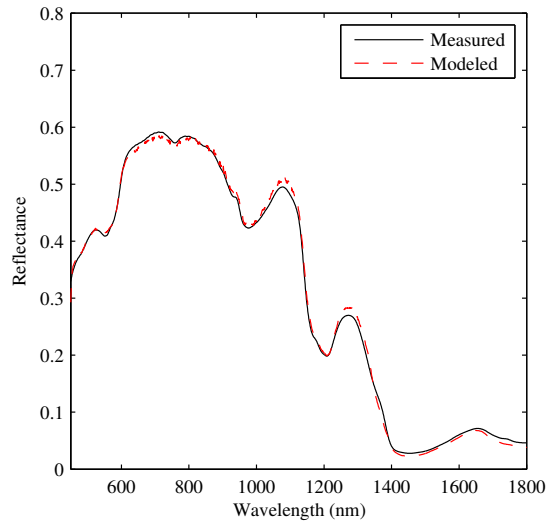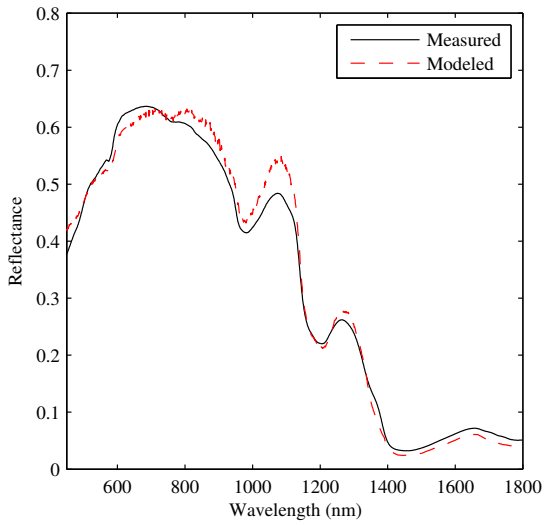
Figure 98: Comparison of model and measured cadaver skin reflectance for sample 27 and 28.
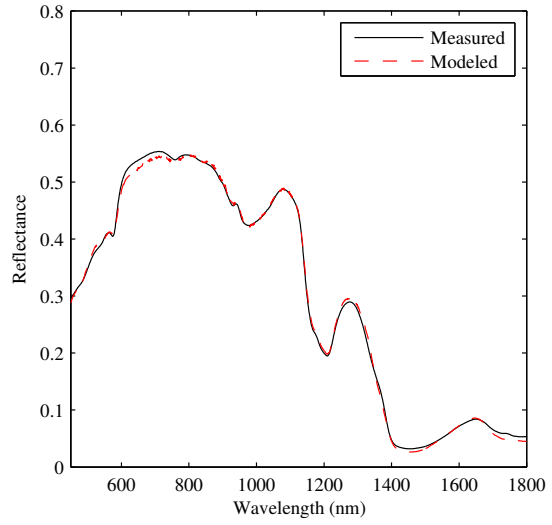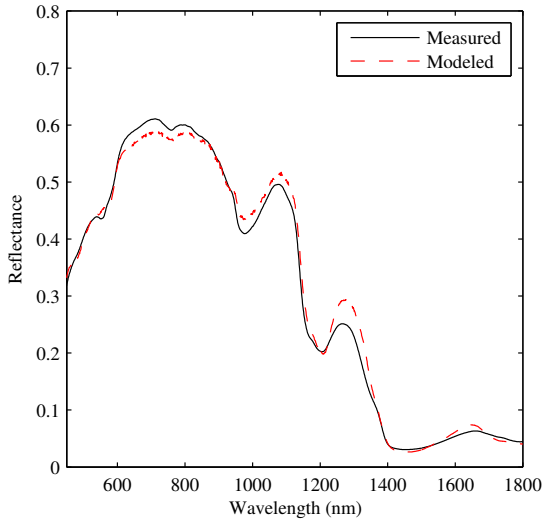
Figure 99: Comparison of model and measured cadaver skin reflectance for sample 29 and 30.
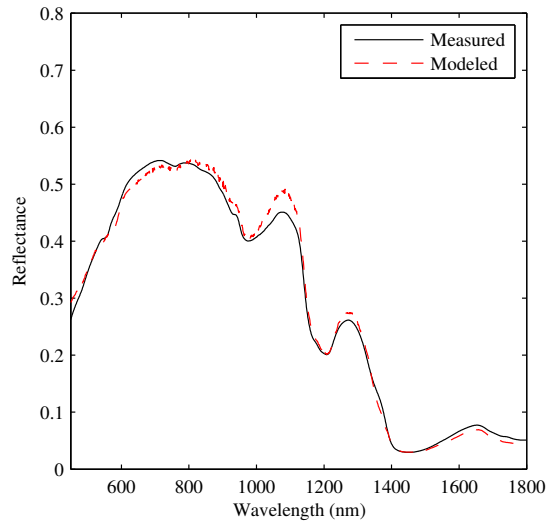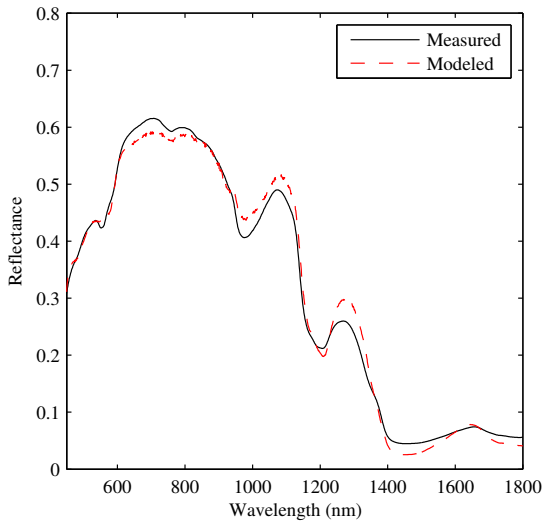
Figure 100: Comparison of model and measured cadaver skin reflectance for sample 31 and 32.

Figure 101:   Comparison of model and measured cadaver skin reflectance for sample 33 and 34.

Figure 102:   Comparison of model and measured cadaver skin reflectance for sample 35 and 36.
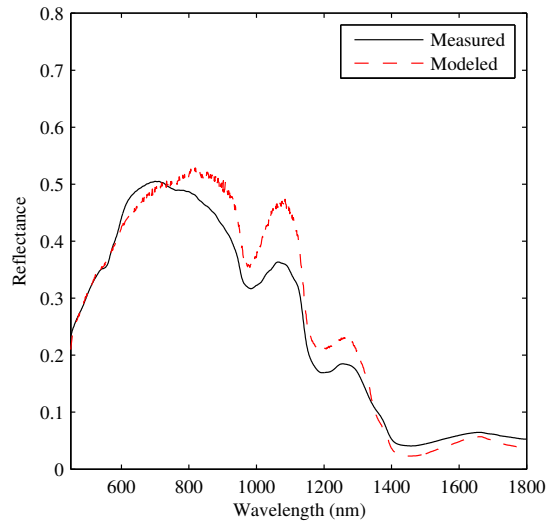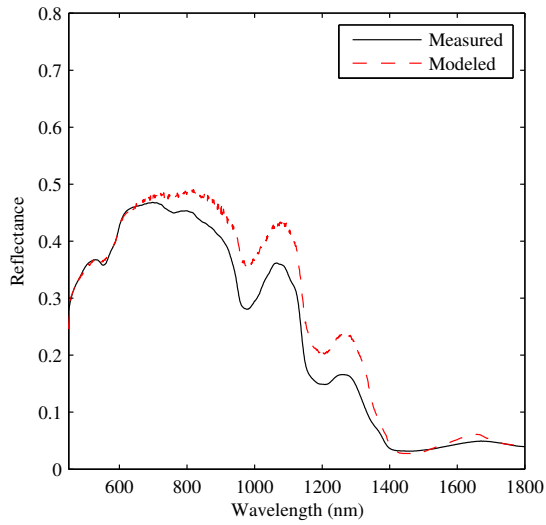
Figure 103: Comparison of model and measured cadaver skin reflectance for sample 37 and 38.

Figure 104: Comparison of model and measured cadaver skin reflectance for sample 39 and 40.

Figure 105:   Comparison of model and measured cadaver skin reflectance for sample 41 and 42.

Figure 106:   Comparison of model and measured cadaver skin reflectance for sample 43 and 44.

Figure 107: Comparison of model and measured cadaver skin reflectance for sample 45 and 46.

Figure 108: Comparison of model and measured cadaver skin reflectance for sample 47 and 48.
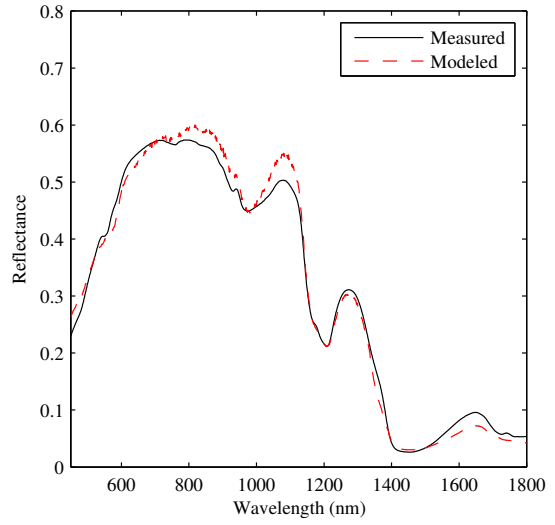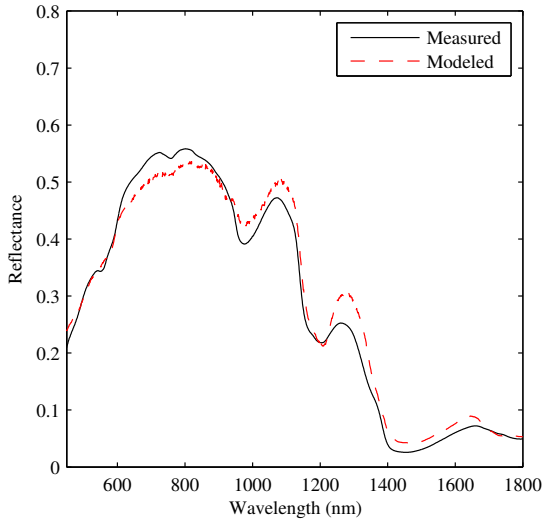
Figure 109:   Comparison of model and measured cadaver skin reflectance for sample 49 and 50.
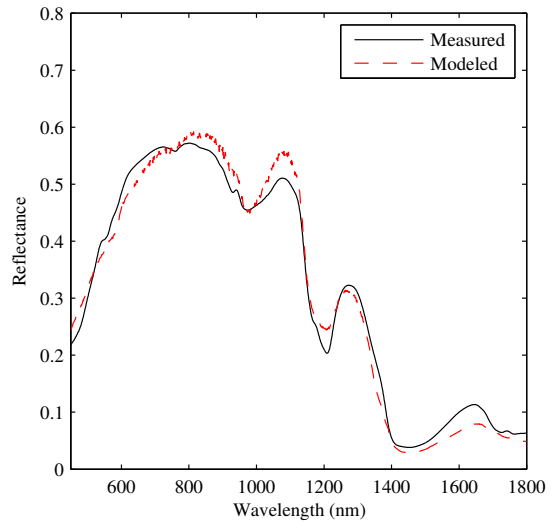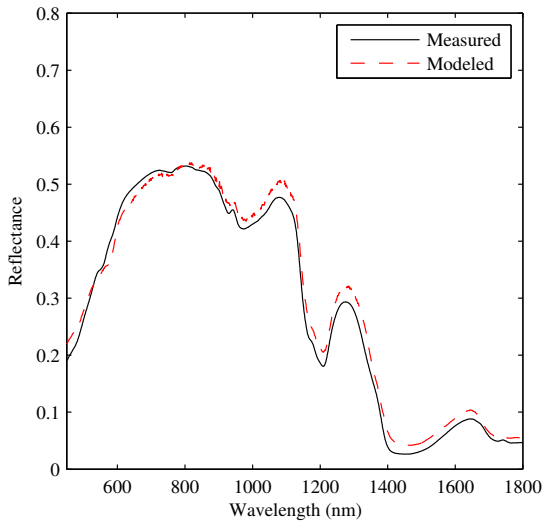

Figure 110:   Comparison of model and measured cadaver skin reflectance for sample 51 and 52.

Figure 111:   Comparison of model and measured cadaver skin reflectance for sample 53 and 54.

Figure 112:   Comparison of model and measured cadaver skin reflectance for sample 55 and 56.
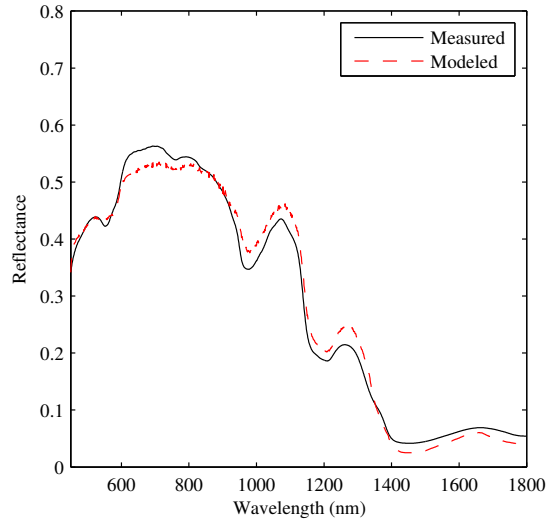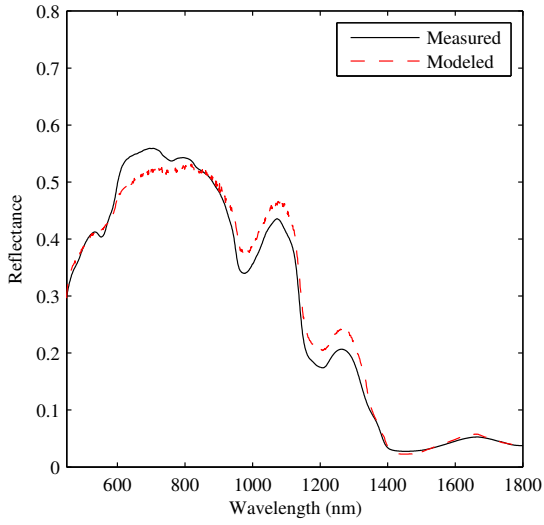
Figure 113:   Comparison of model and measured cadaver skin reflectance for sample 57 and 58.

Figure 114:   Comparison of model and measured cadaver skin reflectance for sample 59 and 60.
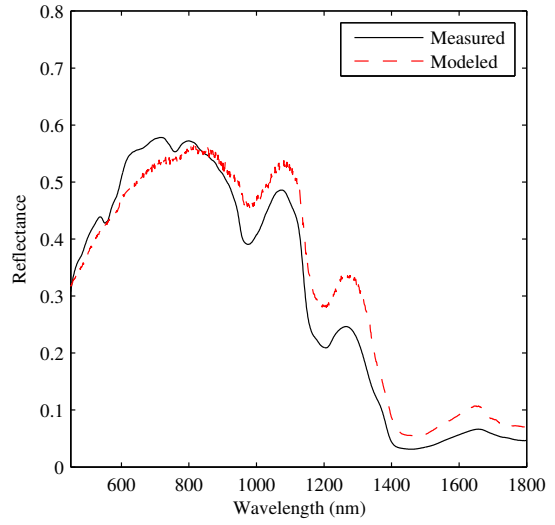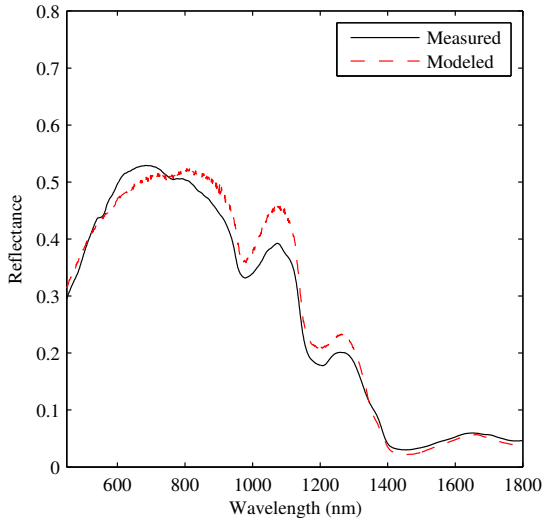
Figure 115:   Comparison of model and measured cadaver skin reflectance for sample 61 and 62.
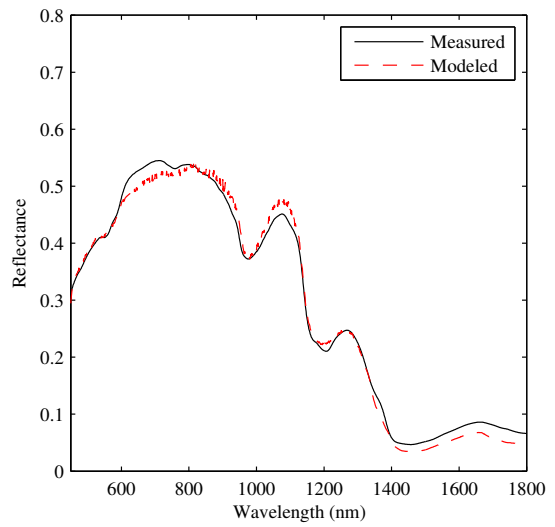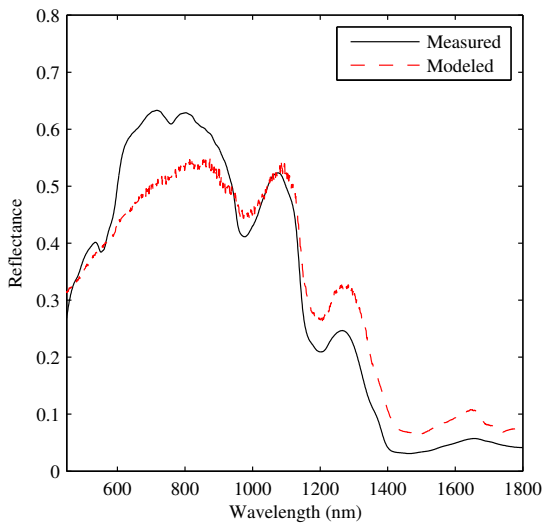
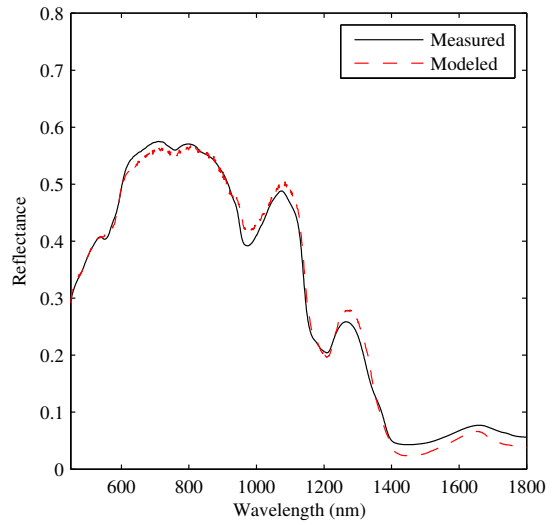Figure 116:   Comparison of model and measured cadaver skin reflectance for sample 63 and 64.
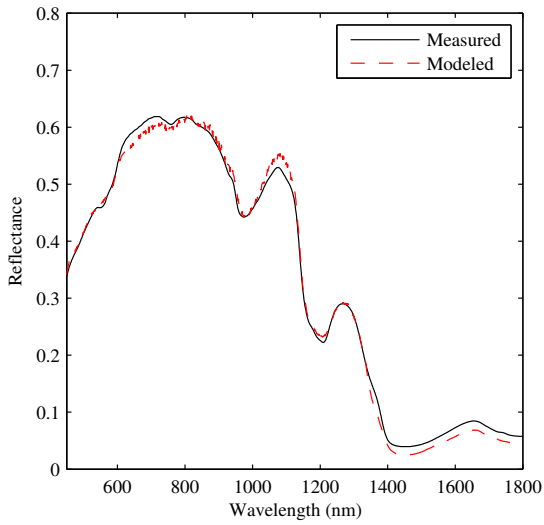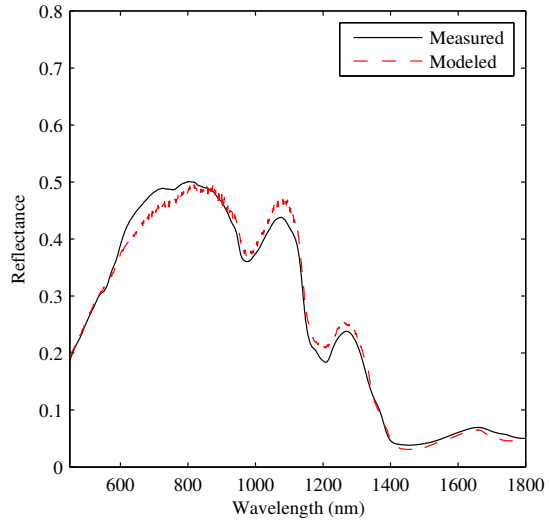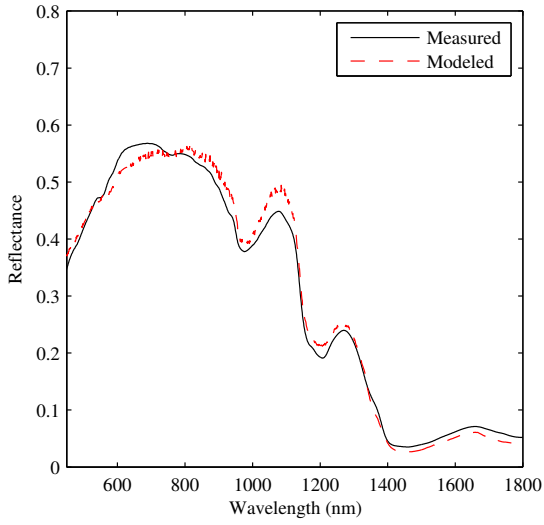
Figure 117:   Comparison of model and measured cadaver skin reflectance for sample
65 and 66.
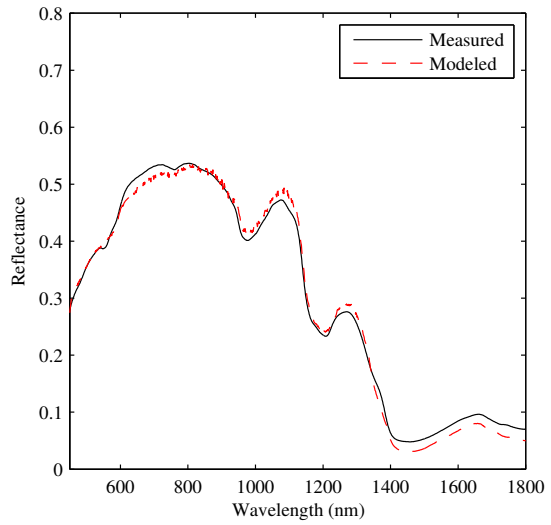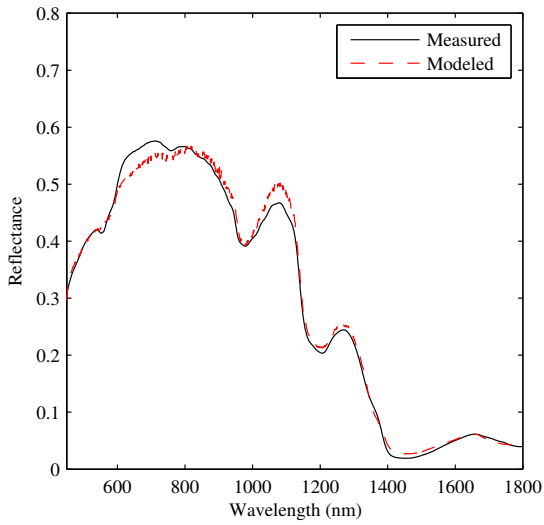
Figure 118:   Comparison of model and measured cadaver skin reflectance for sample
67 and 68.
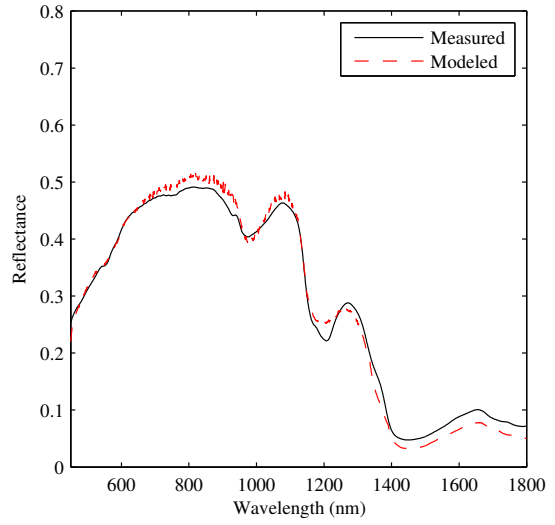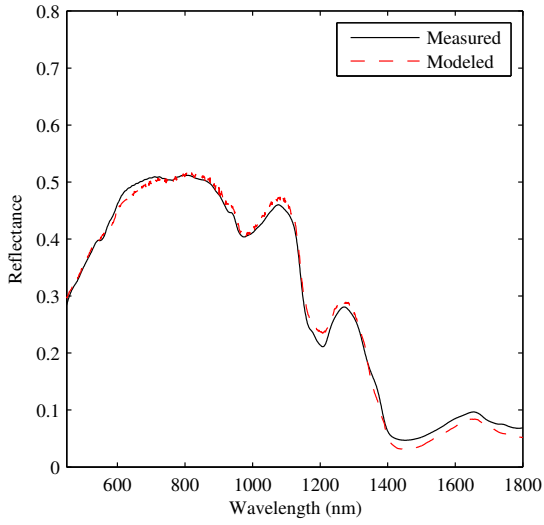
Figure 119: Comparison of model and measured cadaver skin reflectance for sample 69 and 70.
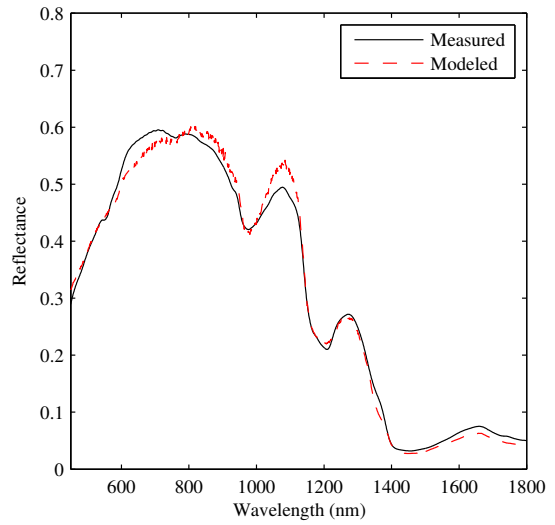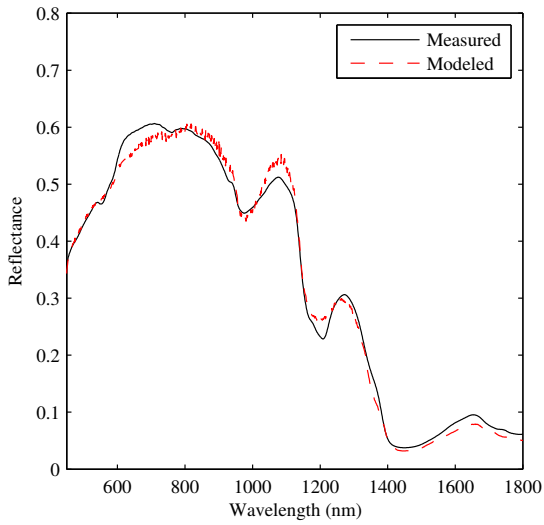
Figure 120: Comparison of model and measured cadaver skin reflectance for sample 71 and 72.
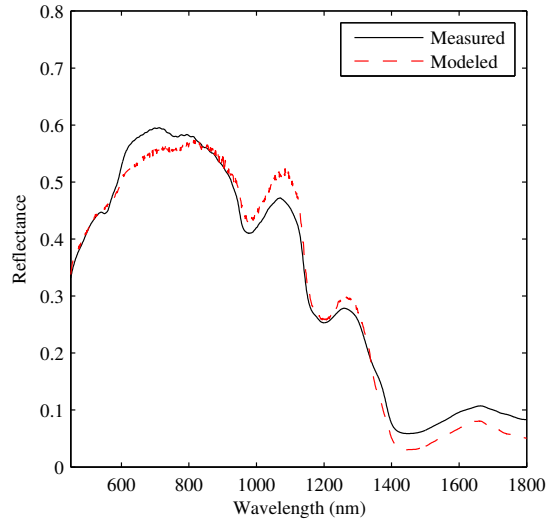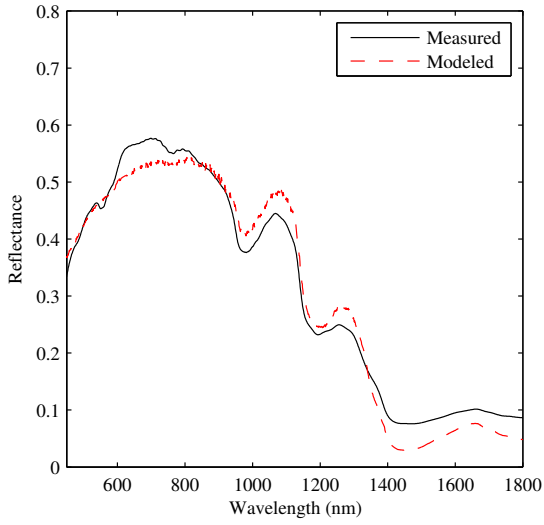
Figure 121: Comparison of model and measured cadaver skin reflectance for sample 73 and 74.
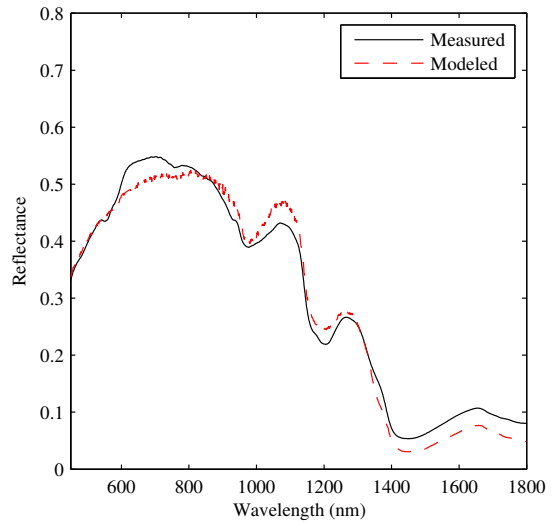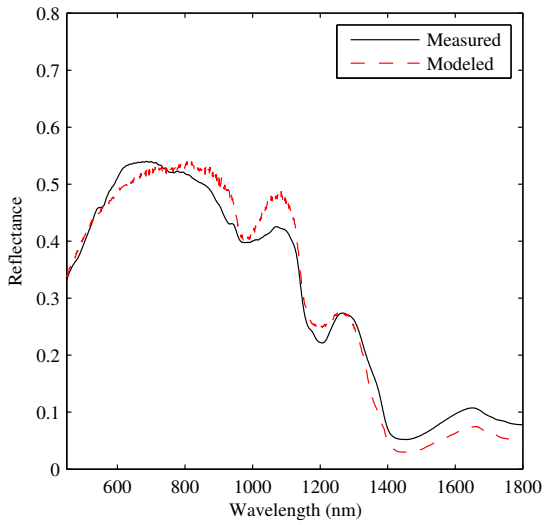
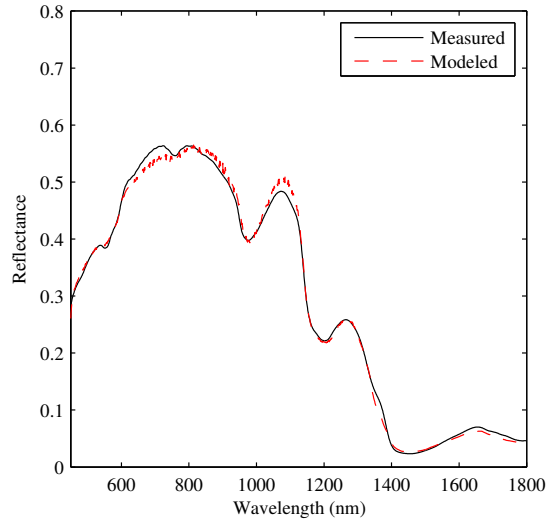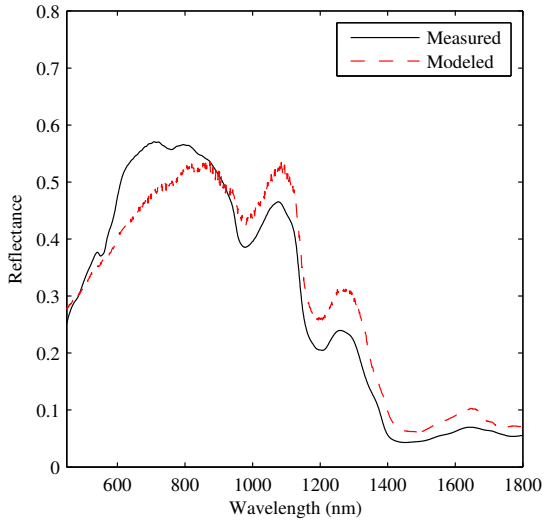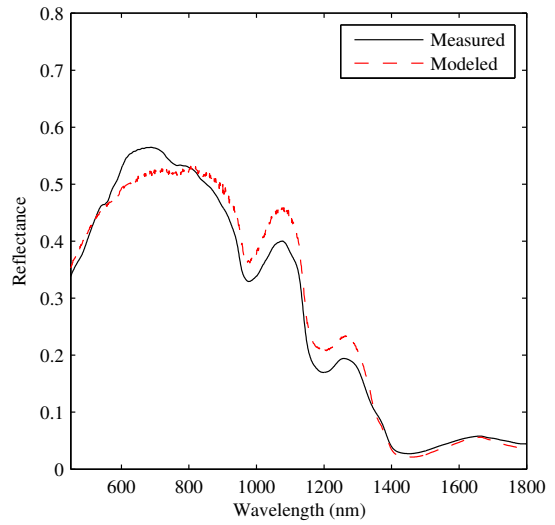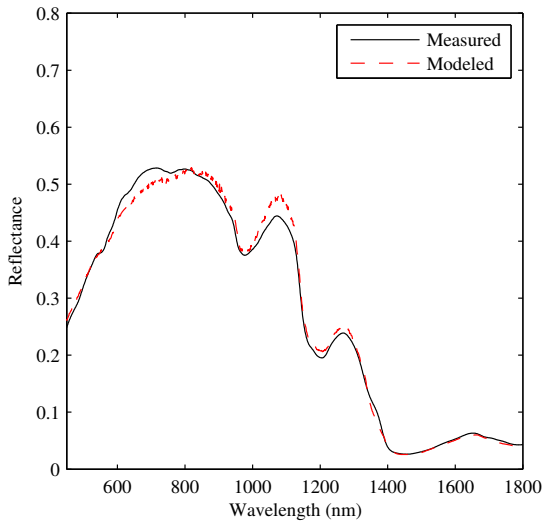Figure 122: Comparison of model and measured cadaver skin reflectance for sample 75 and 76.

Appendix D. Additional Results for Skin Detection Algorithm

Additional results for the skin detection algorithms are presented in this appendix. Figure captions provide a description of the scene and any pertinent information about the collection. The results presented in this appendix are of a qualitative nature showing images of the detection results vice Receiver Operating Characteristic (ROC) Curves. The reason for the qualitative presentation is due to time constraints as the hand-truthing process is time consuming and that quantitative results using ROC curves were presented in Chapter 4.
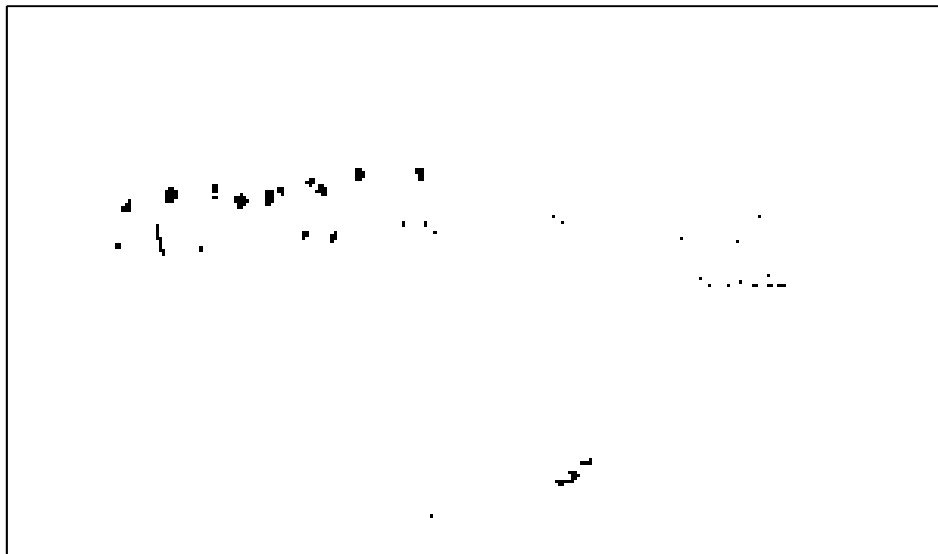
Figure 123: Skin detection results for suburban test scene containing people with a wide variety of pigmentation levels and skin color confusers. Scene was collected with SpecTir's HyperSpecTIR 3 (HST3) imager [36]. People in the scene are approximately 37m from the imager. Normalized Difference Skin Index (NDSI) and Normalized Difference Green Red Index (NDGRI) thresholds are $\beta = 0.45$ and $\gamma = 0$ respectively.

Figure 124:   Skin detection results for suburban test scene containing people with a wide variety of pigmentation levels and skin color confusers. Scene was collected with SpecTir's HST3 imager [36]. People in the scene are approximately 35m from the imager. NDSI and NDGRI thresholds are $\beta = 0.45$ and $\gamma = 0$ respectively.
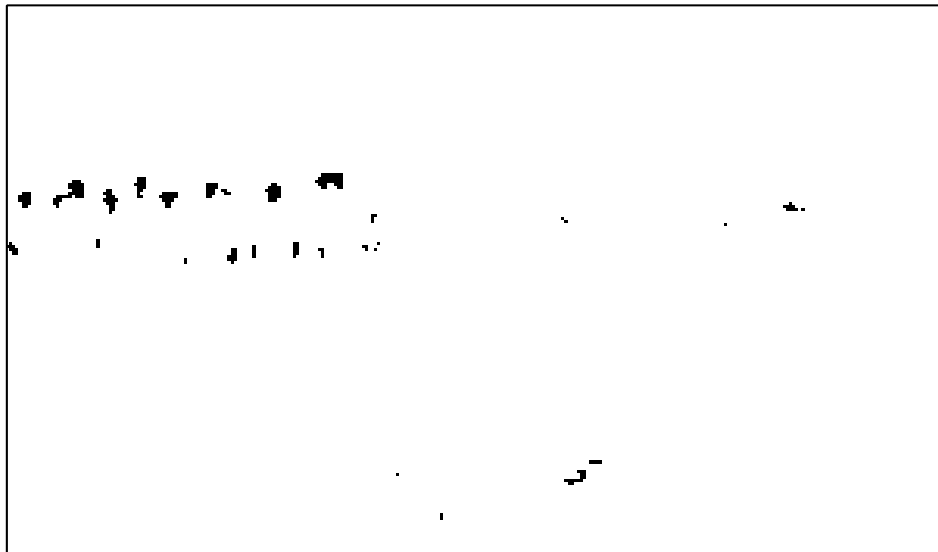
Figure 125:   Skin detection results for suburban test scene containing people with a wide variety of pigmentation levels and skin color confusers. Scene was collected with SpecTir's HST3 imager [36]. People in the scene are approximately 30m from the imager. NDSI and NDGRI thresholds are $\beta = 0.45$ and $\gamma = 0$ respectively.
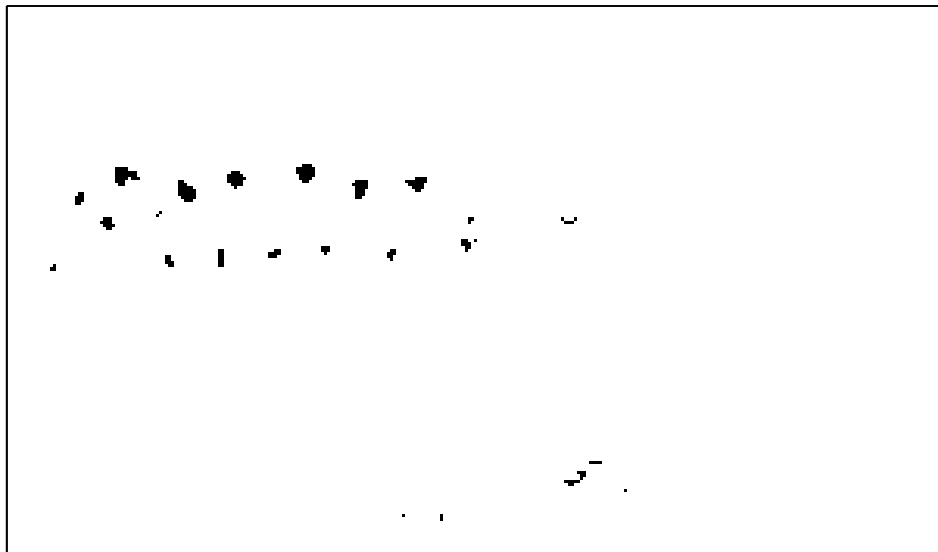
Figure 126:   Skin detection results for suburban test scene containing people with a wide variety of pigmentation levels and skin color confusers. Scene was collected with SpecTir's HST3 imager [36]. People in the scene are approximately 26m from the imager. NDSI and NDGRI thresholds are $\beta = 0.45$ and $\gamma = 0$ respectively.
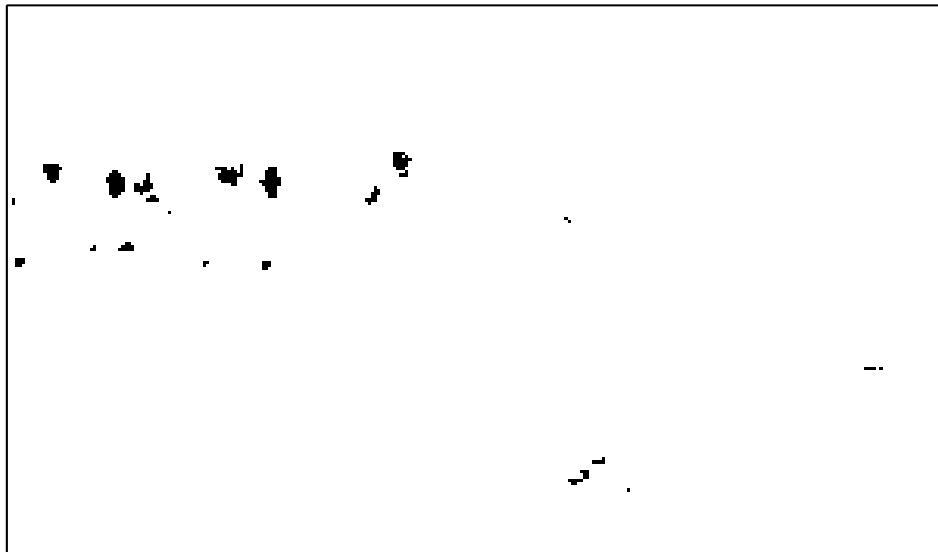
Figure 127: Skin detection results for suburban test scene containing people with a wide variety of pigmentation levels and skin color confusers. Scene was collected with SpecTir's HST3 imager [36]. People in the scene are approximately 22m from the imager. NDSI and NDGRI thresholds are $\beta = 0.45$ and $\gamma = 0$ respectively.

Figure 128: Skin detection results for suburban test scene containing people with a wide variety of pigmentation levels and skin color confusers. Scene was collected with SpecTir's HST3 imager [36]. People in the scene are approximately 19m from the imager. NDSI and NDGRI thresholds are $\beta = 0.45$ and $\gamma = 0$ respectively.

Figure 129:   Color image of suburban test scene. Scene contains one person walking through the parking lot. Scene was collected with the HST3 from a second story window.

Figure 130:   Skin detection results for parking lot and park in a section of Fig. 129. Scene contains one person walking through the parking lot (left) and results of skin detection algorithm (right). Scene was collected with the HST3 from a second story window. NDSI and NDGRI thresholds are $\beta = 0.4$ and $\gamma = -0.1$ respectively.

Figure 131:   Color image of suburban test scene. Scene contains one person in the park area behind a tree to the right of the red asterisk. Scene was collected with the HST3 from a second story window.
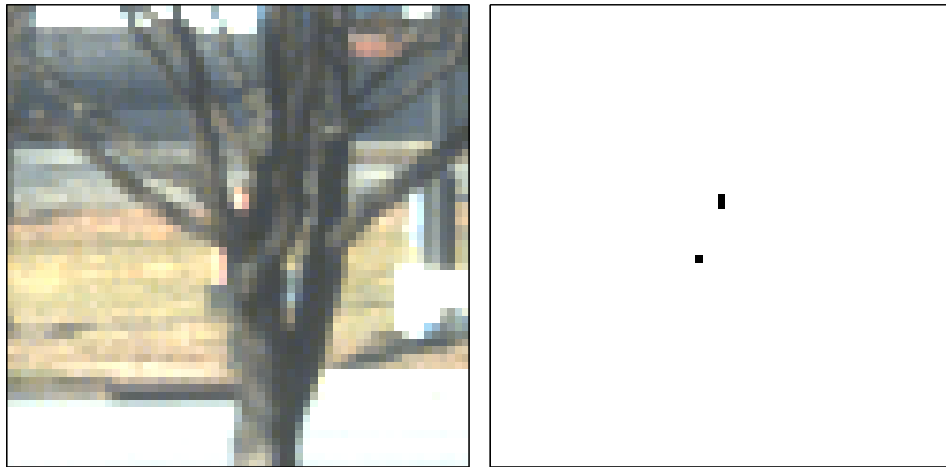
Figure 132:   Skin detection results for suburban test scene in a section of Fig. 131. Scene contains one person in the park area behind a tree (left) and results of skin detection algorithm (right).. Scene was collected with the HST3 from a second story window. NDSI and NDGRI thresholds are $\beta = 0.4$ and $\gamma = -0.1$ respectively.
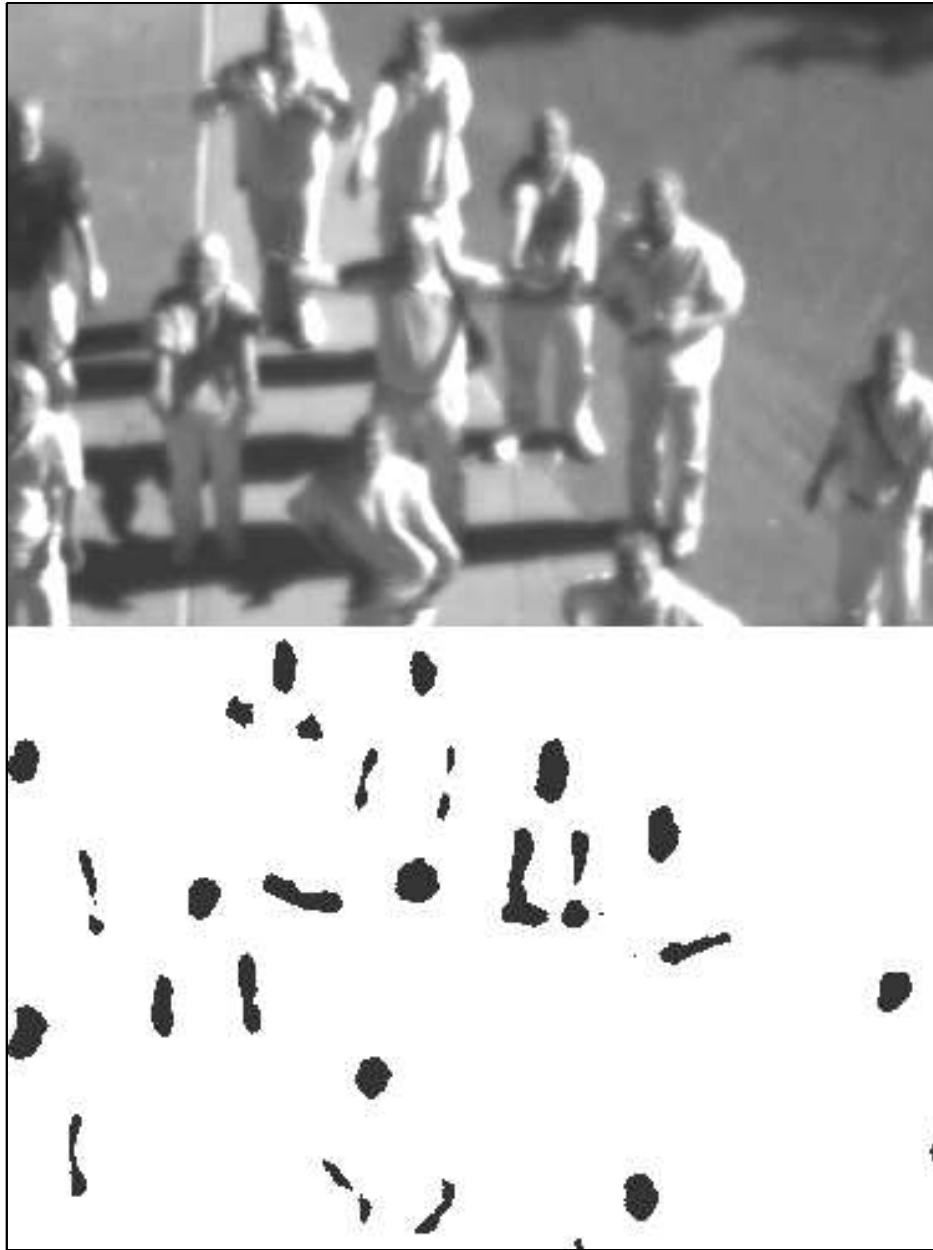
Figure 133: Skin detection results for parking lot. Scene contains people with a wide variety of pigmentation levels. Scene was collected with the Surface Optics Corporation (SOC) 700 NIR hyperspectral imager.

Bibliography

1. Abdel-Mottaleb, M. and A. Elgammal. "Method for Detecting a Face in a Digital Image". *United States Patent Application Number US 2001/0026633*, October 2001.

2. Alaluf, S., D. Atkins, K. Barrett, M. Blount, N. Carter, and A. Heath. "The Impact of Epidermal Melanin on Objective Measurements of Human Skin Colour". *Pigment Cell Research*, 15(2):119–126, April 2002.

3. Albiol, A., L. Torres, and E.J. Delp. "Optimum color spaces for skin detection". *IEEE International Conference on Image Processing (ICIP) 2001*, 1:122–124, October 2001.

4. Analytical Spectral Devices Incorporated. "Product Specifications FieldSpec 3", 2008.

5. Anderson, R.R. and J.A. Parrish. "The Optics of Human Skin". *Journal of Investigative Dermatology*, 77:13–19, 1981.

6. Angelopoulou, E. "Understanding the Color of Human Skin". *Human Vision and Electronic Imaging VI*, 4299(1):243–251, 2001.

7. Arnfield, M.R., J. Tulip, and M.S. McPhee. "Optical Propagation in Tissue with Anisotropic Scattering". *IEEE Transactions on Biomedical Engineering*, 35(5):372–381, May 1988.

8. Baranoski, G.V. and A. Krishnaswamy. "An Introduction to Light Interaction with Human Skin". *RITA*, 11(1), 2004.

9. Brand, J. and J.S. Mason. "A comparative assessment of three approaches to pixel-level human skin-detection". *Proceedings of 15th International Conference on Pattern Recognition*, 1:1056–1059, Sep 2000.

10. Brandorff, C. *Rendering Human Skin*. Technical report, Technishce Universitat Wien, 2006.

11. Bretzner, L., I. Laptev, and T. Lindeberg. "Hand Gesture Recognition using Multi-Scale Colour Features, Hierarchial Models and Particle Filtering". *Proceedings of the Fifth International Conference on Automatic Face and Gesture Recognition*, 405–410, May 2002.

12. Buiteveld, H., J.M.H. Hakvoort, and M. Donze. "The Optical Properties of Pure Water". *SPIE Proceedings on Ocean Optics XI*, 2258:174–183, October 1994.

13. Cheong, W., S.A. Prahl, and A.J. Welch. "A review of the optical properties of biological tissues". *IEEE Journal of Quantum Electronics*, 26(12):2166–2185, Dec 1990.

14. Civil Air Patrol Advanced Technology Group. "Fact Sheet: Civil Air Patrol ARCHER System". *http://atg.cap.gov*, August 2005.

15. Daugman, J. "Face and Gesture Recognition: Overview". *IEEE Transactions on Pattern Analysis and Machine Intelligence*, 19(7):675–676, July 1997.

16. Dawson, J.B., D.J. Barker, D.J. Ellis, E. Grassam, A. Cotterill, G.W. Fisher, and J.W. Feather. "A Theoretical and Experimental Study of Light Aborption and Scattering by In Vivo Skin". *Physics in Medicine and Biology*, 25(4):685–709, 1980.

17. DAZ Productions, Incorporated. "Free 3D Models". Http://www.daz3d.com.

18. Dereniak, E.L. and G.D. Boreman. *Infrared detectors and systems*. Wiley, New York, 1996.

19. Dowdall, J., I. Pavlidis, and G. Bebis. "Face Detection in the Near-IR Spectrum". *Proceedings of Infrared Technology and Applications XXIX*, 5074:745–756, 2003.

20. Duda, R.O., P.E. Hart, and D.G. Stork. *Pattern classification*. Wiley, New York, 2001.

21. Eismann, M. T. "OENG 633 Hyperspectral Remote Sensing", 2006. Air Force Institute of Technology course notes.

22. Eismann, M. T. "Strategies for hyperspectral target detection in complex background environments". *IEEE Aerospace Conference*, 10, 2006.

23. Eun, H.C. "Evaluation of Skin Blood Flow by Laser Doppler Flowmetry". *Clinics in Dermatology*, 13(4), Jul-Aug 1995.

24. Fitzpatrick, T.B., G. Szabo, and M.M. Wick. "Biochemistry and Physiology of Melanin Pigmentation". Lowell A. Goldsmith (editor), *Biochemistry and physiology of the skin*. Oxford University Press, New York, 1983.

25. Fleck, M.M. "Finding Naked People". *Proceedings of the 4th European Conference on Computer Vision*, 1065:593–602, 1996.

26. Friebel, M. and A. Roggan. "Determination of Optical Properties of Human Blood in the Spectral Range 250 to 1100 nm Using Monte Carlo Simulations with Hematocrit-Dependent Effective Scattering Phase Functions". *Journal of Biomedical Optics*, 11(3), May/June 2006.

27. Gomez, G. "On selecting colour components for skin detection". *Proceedings of the International Conference on Pattern Recognition*, 16(2):961–964, 2002.

28. Hecht, E. *Optics*. Addison-Wesley, Reading, Mass., 2002.

29. Hoffmann, G. "CIE Color Space". *online http://www.fho-emden.de/ hoffmann/-ciexyz29082000.pdf*, August 2000.

30. Hsu, R., Mohamed A., and A.K. Jain. "Face detection in color images". *IEEE International Conference on Image Processing (ICIP) 2001*, 1:1046–1049, October 2001.

31. Igarashi, T., K. Nishino, and S.K. Nayar. "The Appearance of Human Skin". *online http://www.cs.columbia.edu/techreports/cucs-024-05.pdf*, June 2005.

32. International Commission on Illumination. "Selected Colorimetric Tables". *online: http://www.cie.co.at/main/freepubs.html*.

33. Jablonski, N. and G. Chaplin. "The evolution of human skin coloration". *Journal of human evolution*, 39(1):57–106, 2000.

34. Jablonski, N. and G. Chaplin. "Skin Deep". *Scientific American*, 287(4):74–81, 2002.

35. Jacques, S.L. "Skin Optics". *online: http://omlc.ogi.edu/news/jan98/skinoptics.html*, Jan 1998.

36. Jengo, C.M. and J. LaVeigne. "Sensor performance comparison of HyperSpecTIR instruments 1 and 2". *Proceedings IEEE Aerospace Conference*, 3:1805, March 2004.

37. Jimbow, K., T.B. Fitzpatrick, and M.M. Wick. "Biochemistry and Physiology of Melanin Pigmentation". *Physiology, Biochemistry, and Molecular Biology of the Skin*, 2:873–909, 1991.

38. Jones, M.J. and J.M. Rehg. "Statistical color Models with Application to Skin Detection". *International Journal of Computer Vision*, 46(1), January 2002.

39. Kalra, P. and N. Magnenat-Thalmann. "Modeling of vascular expressions in facial animation". *Proceedings of Computer Animation*, May 1994.

40. Kilgore, G.A. and P.R. Whillock. "Skin Detection Sensor". *United States Patent Application Number 11/264,654*, October 2005.

41. Kirchweger, G. "The Biology of Skin Color: Black and White". *Discover*, 22(2):32–33, February 2001.

42. Koenderink, J. and S. Pont. *The Secret of Velvety Skin*. Technical report, Helmholtz Instituut, Universiteit Utrecht, Utrecht, The Netherlands, 2002.

43. Kollias, N. "The physical basis of skin color and its evaluation". *Clinics in Dermatology*, 13(4):361–367, 0 1995.

44. Krishnaswamy, A. *BioSpec: A Biophysically-Based Spectral Model of Light Interaction with Human Skin*. Master's thesis, University of Waterloo, 2005.

45. Krishnaswamy, A. and G. Baranoski. "A Study of Skin Optics", January 2004. Technical Report CS-2004-01, Natural Phenomena Simulation Group, School of Computer Science, University of Waterloo, Canada.

46. Leonard, C., M. DeWeert, J. Gradie, J. Iokepa, and C. Stalder. "Performance of an EO/IR Sensor System in Marine Search and Rescue". *Proceedings of Airborne Intelligence, Surveillance, Reconnaissance (ISR) Systems and Applications II*, 5787:122–133, June 2005.

47. Lichtman, M.A., W.J. Williams, E. Beutler, K. Kaushansky, T.J. Kipps, U. Seligsohn, and J. Prchal. *Williams Hematology*. McGraw-Hill Professional, 2005.

48. Lorizcz, A.L. "Pigmentation". Stephan Rothman (editor), *Physiology and biochemistry of the skin.*, 515–563. University of Chicago Press, Chicago, 1954.

49. Manolakis, D. and G. Shaw. "Detection algorithms for hyperspectral imaging applications". *IEEE Signal Processing Magazine*, 19(1):29–43, Jan 2002.

50. Marschner, S.R., S.H. Westin, E.P. Lafortune, and K.E. Torrance. "Image-Based Bidirectional Reflectance Distribution Function Measurement". *Applied Optics*, 39(16):2592–2600, Jun 2000.

51. Matts, P.J., P.J. Dykes, and R. Marks. "The distribution of melanin in skin determined in vivo". *British Journal of Dermatology*, 156(4):620–628, Apr 2007.

52. Meglinski, I.V. and S.J. Matcher. "Modeling of skin reflectance spectra". *Saratov Fall Meeting 2000: Optical Technologies in Biophysics and Medicine II*, 4241(1):78–87, 2001.

53. Meglinski, I.V. and S.J. Matcher. "Quantitative Assessment of Skin Layers Absorption and Skin Reflectance Spectra Simulation in the Visible and Near-Infrared Spectral Regions". *Physiological Measurement*, 23:741–753, 2002.

54. Mitra, S. and T. Acharya. "Gait Recognition: A Survey". *IEEE Transactions on Systems, Man, and Cybernetics-PartC: Applications and Reviews*, 37(3):311–324, May 2007.

55. Montagna, W. *Atlas of Normal Human Skin*. Springer-Verlag, New York, 1992.

56. Moore, T.L., M. Lunt, B. McManus, M.E. Anderson, and A.L. Herrick. "Seventeen-Point Dermal Ultrasound Scoring System - A Reliable Measure of Skin Thickness in Patients with Systemic Sclerosis". *Rheumatology*, (42):1559–1563, 2003.

57. Nordlund, J.J. and J. Ortonne. "The Normal Color of Human Skin". James J. Nordlund, Raymond E. Boissy, Vincent J. Hearing, and Richard A. King (editors), *The Pigmentary System: Physiology and Pathophysiology*, 475–487. Oxford University Press, 1998.

58. Nunez, A.S. and M.J. Mendenhall. "Detection of Human Skin in Near Infrared Hyperspectral Imagery". *International Geoscience and Remote Sensing Symposium*, July 2008.

59. Nunez, A.S., K.C. Gross M.J. Mendenhall, and H.C. Bertram. "Hyperspectral Modeling of Human Skin Reflectance in the Visible and Near Infrared". *IEEE Transacations on Biomedical Engineering, Draft*, 2009.

60. Odland, G.F. "Structure of Skin". *Physiology, Biochemistry, and Molecular Biology of the Skin*, 1:3–62, 1991.

61. Palmer, K.F. and D. Williams. "Optical properties of water in the near infrared." *Journal of the Optical Society of America (1917-1983)*, 64:1107–1110, 1974.

62. Pan, Z., G. Healey, M. Prasad, and B. Tromberg. "Face recognition in hyperspectral images". *IEEE Transactions on Pattern Analysis and Machine Intelligence*, 25(12):p1552 – 1560, December 2003.

63. Pan, Z., G. Healey, M. Prasad, and B. Tromberg. "Hyperspectral Face Recognition Under Variable Outdoor Illumination". *Algorithms and Technologies for Multispectral, Hyperspectral, and Ultraspectral Imagery X*, 5425:520–529, August 2004.

64. Pavlidis, I., P. Symosek, B. Fritz, M. Bazakos, and N. Papanikolopoulos. "Automatic detection of vehicle occupants: the imaging problem and its solution". *Machine Vision and Applications*, 11(6):313–320, May 2000.

65. Peer, P., J. Kovac, and F. Solina. "Human Skin Colour Clustering for Face Detection", September 2003.

66. Pishva, D. "Spectroscopic Approach for Aliveness Detection in Biometrics Authentication". *41st Annual IEEE International Carnahan Converence*, 133–137, October 2007.

67. Poirier, G. *Human Skin Modelling and Rendering*. Master's thesis, The University of Waterloo, 2003.

68. Prahl, S.A. "Tabulated Molar Extinction Coefficient for Hemoglobin in Water". URL `omlc.ogi.edu/spectra/hemoglobin/summary.html`.

69. Prahl, S.A. *Light Transport in Tissue*. Ph.D. thesis, University of Texas at Austin, 1988.

70. Rothman, S. "Circulation and Vascular Reactions". Stephan Rothman (editor), *Physiology and biochemistry of the skin.*, 61–119. Univ. of Chicago Press, Chicago, 1954.

71. Saidi, I.S., S.L. Jacques, and F.K. Tittel. "Mie and Rayleigh Modeling of Visible Light Scattering in Neonatal Skin". *Applied Optics*, 341(31), Nov 1995.

72. Salomatina, E., B. Jiang, J. Novak, and A. Yaroslavasky. "Optical Properties of Normal and Cancerous Human Skin in the Visible and Near-Infrared Spectral Range". *Journal of Biomedical Optics*, 11(6), Nov/Dec 2006.

73. Salomonson, V.V. and I. Appel. "Estimating Fractional Snow Cover from MODIS Using the Normalized Difference Snow Index". *Remote Sensing of Environment*, 89(3):351–360, 2004.

74. Sanchey-Reillo, R., C. Sanchez-Avila, and A. Gonzalez-Marcos. "Biometric Identification through Hand Geometry Measurements". *IEEE Transactions on Pattern Analysis and Machine Intelligence*, 22(10):1168–1171, October 2000.

75. Seeley, R., T. Stephens, and P. Tate. *Anatomy and Physiology*. McGraw-Hill, San Francisco, 1998.

76. Simard, J., P. Mathieu, G. Fournier, and V. Larochelle. "A Range-Gated Intensified Spectrographic Imager: an Instrument for Active Hyperspectral Imaging". *Proceedings of Laser Radar Technology and Applications V*, 4035:180–191, 2000.

77. Simi, C., A. Hill, and H. Kling. "Airborne remote spectrometry support to rescue personnel at "Ground Zero" after the World Trade Center attack on September 11, 2001". *Proceedings of Imaging Spectrometry VIII,*, 4816:23–32, 2002.

78. Simpson, C.R., M. Kohl, M. Essenpreis, and M. Cope. "Near Infrared Optical Properties of Ex Vivo Human Skin and Subcutaneous Tissues Using the Monte Carlo Inversion Technique". *Physics in Medicine and Biology*, 43:2465–2478, 1998.

79. Soriano, M., B. Martinkauppi, S. Huovinen, and M. Laaksonen. "Skin detection in video under changing illumination conditions". *Proceedings. 15th International Conference on Pattern Recognition, 2000.*, 1:839–842, 2000.

80. Stamatas, G.N., B.Z. Zmudzka, N. Kollias, and J.Z. Beer. "Non-Invasive Measurements of Skin Pigmentation in Situ". *Pigment Cell Research*, 17(6):618–626, Dec 2004.

81. Stevenson, B., R. O'Connor, W. Kendall, A. Stocker, W. Schaff, R. Holasek, D. Even, D. Alexa, J. Salvador, M. Eismann, R. Mack, P. Kee, S. Harris, B. Karch, and J. Kershenstein. "The Civil Air Patrol ARCHER Hyperspectral Sensor System". *Airborne Intelligence, Surveillance, Reconnaissance (ISR) Systems and Applications II*, 5787(1):17–28, 2005.

82. Storring, M., H. J. Andersen, and E. Granum. "Physics-based modelling of human skin colour under mixed illuminants". *Robotics and Autonomous Systems*, 35(3):131–142, 0630.

83. Storring, M., H.J. Andersen, and E. Granum. "Skin colour detection under changing lighting conditions". *7th International Symposium on Intelligent Robotic Systems*, 187–195, July 1999.

84. Storring, M., T. Kocka, H.J. Andersen, and E. Granum. "Tracking Regions of Human Skin Through Illumination Changes". *Pattern Recognition Letters*, 24(11):1715–1723, 2003.

85. Subramanian, S. and N. Gat. "Subpixel object detection using hyperspectral imaging for search and rescue operations". *Automatic Target Recognition VIII*, 3371(1):216–225, April 1998.

86. Taroni, P., D. Comelli, A. Pifferi, A. Torricelli, and R. Cubeddu. "Absorption of collagen: Effects on the Estimate of Breast Composition and Related Diagnostic Implications". *Journal of Biomedical Optics*, 12(1):1–4, January/February 2007.

87. Thornton, W. A. "Luminosity and Color-Rendering Capability of White Light". *Journal of the Optical Society of America*, 61(9):1155–1163, September 1971.

88. Thum, J., L. Caspary, A. Creutzig, and K. Alexander. "A New Method for the Assessment of Tissue Hemoglobin Oxygenation in Patients with Chronic Venous Insufficiency". *Microvascular Research*, 51(3):317–326, 1996.

89. Topping, M., J. Pfeiffer, A. Sparks, K. Jim, and D. Yoon. "ADVANCED AIRBORNE HYPERSPECTRAL IMAGING SYSTEM (AAHIS)". *Proceedings of Imaging Spectrometry VIII,*, 4816:1–11, 2002.

90. Tsai, C.L., J. Chen, and W. Wang. "Near-infrared Absorption Property of Biological Soft Tissue Constituents". *Journal of Medical and Biological Engineering*, 21(1), 2001.

91. Van Gemert, M.J.C., S.L. Jacques, H.J.C.M. Sterenborg, and W.M. Star. "Skin Optics". *IEEE Transactions on Biomedical Engineering*, 36(12):1146–1154, December 1989.

92. Vezhnevets, V., V. Sazonov, and A. Andreeva. "A survey on pixel-based skin color detection techniques", 2003. URL `citeseer.ist.psu.edu/vezhnevets03survey.html`.

93. Wagner, J.K., C. Jovel, H.L. Norton, E.J. Parra, and M.D. Shriver. "Comparing Quantitative Measures of Erythema, Pigmentation and Skin Response using Reflectometry". *Pigment Cell Research*, (15):379–384, 2002.

94. Walker, J. "Colour Rendering of Spectra". *www.fourmilab.ch*, April 1996.

95. Wang, H. and S. Chang. "Rapid Modeling of Diffuse Reflectance of Light in Turbid Slabs". *Journal of the Optical Society of America*, 15(4):936–944, April 1998.

96. Wang, X., B.W. Pogue, C. Kogel, S.P. Poplack, and W.A. Wells. "Approximation of Mie Scattering Parameters in Near-Infrared Tomography of Normal Breast Tissue In Vivo". *Journal of Biomedical Optics*, 15(5), September 2005.

97. Yang, M., D.J. Kriegman, and N. Ahuja. "Detecting faces in images: A survey". *IEEE Transactions on Pattern Analysis and Machine Intelligence*, 24(1):34–58, 2002.

98. Zonios, G., J. Bykowski, and N. Kollias. "Skin Melanin, Hemoglobin, and Light Scattering Properties can be Quantitatively Assessed In Vivo Using Diffuse Reflectance Spectroscopy". *Journal of Investigative Dermatology*, 117:1452–1457, 2001.

REPORT DOCUMENTATION PAGE

The public reporting burden for this collection of information is estimated to average 1 hour per response, including the time for reviewing instructions, searching existing data sources, gathering and maintaining the data needed, and completing and reviewing the collection of information. Send comments regarding this burden estimate or any other aspect of this collection of information, including suggestions for reducing the burden, to Department of Defense, Washington Headquarters Services, Directorate for Information Operations and Reports (0704-0188), 1215 Jefferson Davis Highway, Suite 1204, Arlington, VA 22202-4302. Respondents should be aware that notwithstanding any other provision of law, no person shall be subject to any penalty for failing to comply with a collection of information if it does not display a currently valid OMB control number.
PLEASE DO NOT RETURN YOUR FORM TO THE ABOVE ADDRESS.

1. REPORT DATE *(DD-MM-YYYY)*	2. REPORT TYPE	3. DATES COVERED *(From - To)*
12-15-2009	Doctoral Dissertation	Aug 2006 - Sep 2009

4. TITLE AND SUBTITLE

A Physical Model of Human Skin and Its Application for Search and Rescue

5a. CONTRACT NUMBER

5b. GRANT NUMBER

5c. PROGRAM ELEMENT NUMBER

6. AUTHOR(S)

Abel S. Nunez, Maj, USAF

5d. PROJECT NUMBER

JON 09-320 (Michael J. Mendenhall)

5e. TASK NUMBER

5f. WORK UNIT NUMBER

7. PERFORMING ORGANIZATION NAME(S) AND ADDRESS(ES)

Air Force Institute of Technology
Graduate School of Engineering and Management (AFIT/EN)
2950 Hobson Way
WPAFB OH 45433-7765

8. PERFORMING ORGANIZATION REPORT NUMBER

AFIT/DEO/ENG/09-14

9. SPONSORING/MONITORING AGENCY NAME(S) AND ADDRESS(ES)

Air Force Research Lab
Sensors ATR - Target Recognition Branch
Dr. Devert Wicker, devert.wicker@wpafb.af.mil, DSN 785-1175 x 4250
2241 Avionics Circle
Wright Patterson AFB OH 45433

10. SPONSOR/MONITOR'S ACRONYM(S)

AFRL/RYAT

11. SPONSOR/MONITOR'S REPORT NUMBER(S)

12. DISTRIBUTION/AVAILABILITY STATEMENT

APPROVED FOR PUBLIC RELEASE; DISTRIBUTION UNLIMITED.

13. SUPPLEMENTARY NOTES

This material is declared a work of the U.S. Government and is not subject to copyright protection in the United States.

14. ABSTRACT

For this research we created a human skin reflectance model in the VIS and NIR. We then modeled sensor output for an RGB sensor based on output from the skin reflectance model. The model was also used to create a skin detection algorithm and a skin pigmentation level (skin reflectance at 685nm) estimation algorithm. The average root mean square error across the VIS and NIR between the skin reflectance model and measured data was 2%. The skin reflectance model then allowed us to generate qualitatively accurate responses for an RGB sensor for different biological and lighting conditions. To test the accuracy of the skin detection and skin color estimation algorithms, hyperspectral images of a suburban test scene containing people with various skin colors were collected. The skin detection algorithm had a probability of detection as high as 95% with a probability of false alarm of 0.6%. The skin pigmentation level estimation algorithm had a mean absolute error when compared with data measured by a reflectometer of 2.6% where the reflectance of the individuals at 685nm ranged from 14% to 64%.

15. SUBJECT TERMS

hyperspectral, skin reflectance, skin detection, skin pigmentation, reduced scattering coefficient

16. SECURITY CLASSIFICATION OF:			17. LIMITATION OF ABSTRACT	18. NUMBER OF PAGES	19a. NAME OF RESPONSIBLE PERSON
a. REPORT	b. ABSTRACT	c. THIS PAGE			Michael J. Mendenhall, Maj, USAF (ENG)
U	U	U	UU	205	**19b. TELEPHONE NUMBER** *(Include area code)* (937)255-3636x4614 michael.mendenhall@afit.edu